Challenge Journal of STRUCTURAL MECHANICS

Vol.6 No.3 (2020)

Mindlin's theory buckling building codes compressive strength dynamic analysis dynamic response earthquake finite element analysis finite element method mechanical properties nonlinear analysis optimization prefabrication pushover analysis reinforced concrete seismic analysis seismic design seismic isolation shallow foundations steel silo temperature effects thick plate wind

ISSN 2149-8024

TULPAR ACADEMIC PUBLISHING

Challenge Journal of Structural Mechanics

E-mail: *cjsmec@challengejournal.com*

Web page: *cjsmec.challengejournal.com*

TULPAR Academic Publishing
www.tulparpublishing.com

Challenge Journal of Structural Mechanics

CONTENTS

Research Articles

TULPAR ACADEMIC PUBLISHING

Challenge Journal of Structural Mechanics

Research Article

Design analysis of a steel industrial building with wide openings exposed to fire

Burak Kaan Cirpici [a,*]

[a] *Department of Civil Engineering, Erzurum Technical University, 25050 Erzurum, Turkey*

ABSTRACT

In order to design a fire-resistant steel structure, the change in the physical and mechanical properties of the steel at high temperatures must be known. As the temperature of steel structural elements increases during fire, their strength decreases considerably. After a certain temperature, these strength drops reach critical levels. Therefore, collapses and various deformations (buckling, arching, etc.) occur. To prevent these collapses during the fire, various fire protection materials must be applied to the structural members such as column and beam. Columns are the most critical structural elements in a steel bearing system. While the possible collapse of the columns may cause the collapse of the whole structure, the beams alone may not cause the collapse of the structure, and the column-beam junctions directly affect the spread of fire. Since there will be many openings and gaps in industrial buildings, the spread and growth of a possible fire becomes very serious. Special fire protection measures are therefore required. In this study, the behavior of a steel industrial structure designed and designed under the influence of Standard Fire (ISO 834) was investigated, the distribution of the temperatures in the structural elements was determined, the required fire protection material was selected, and both protected and unprotected steel temperatures were determined. This design against fire is designed to provide fire resistance for 1 hour (60 min) for this structure. During this period, the type and optimum thickness of the protection material to be applied before reaching the critical temperature values for which the strength of the steel material would lose and would be damaged and compared with the temperatures that would occur in the structural elements without applying fire protection. According to the findings of the study, it was concluded that 25 mm drywall box protection material should be applied on the inner columns and 20 mm on the edge columns and 15 mm on the corner columns. In addition to this, it was concluded that spray beams (intumescent coating) of different thicknesses between 15-20 mm were applied to the beams depending on the location and the load to be affected and the type of joint. After these applied passive fire protection materials, the temperatures obtained in the structural elements reached to 500-550 as a result of 1-hour fire design. These temperatures are acceptable temperature values given the strength drop in critical temperature ranges for steel under the 1-hour fire condition.

ARTICLE INFO

Article history:
Received 7 January 2020
Revised 3 February 2020
Accepted 24 February 2020

Keywords:
Unprotected steel
Protected steel
Passive fire protection system
Fire design
Industrial steel structure

1. Introduction

As is well known, buildings might have a damage from foreseen extreme events such as earthquakes, natural hazards as well as fires and explosions. An experimental study to examine the fire damage of unprotected structural steel members in an industrial fabric building has been performed by Piroglu et al. (2017). In that work, tensile tests were performed on various columns and a tubular space truss member so as to determine the post-

* *Corresponding author*. Tel.: 444-5-388 ; Fax: +90-442-230-0036 ; E-mail address: burak.cirpici@erzurum.edu.tr (B. K. Cirpici)
ISSN: 2149-8024 / DOI: https://doi.org/10.20528/cjsmec.2020.03.001

fire mechanical properties in order to help for final decision whether removal, reusage or strengthening of the industrial steel building. The verification of the minimum fire resistance of existing industrial building has been done by Bilotta et al. (2017) with the help of some regulations to ensure occupant safety as well as a very limited structural damage with particular reference to intumescent coatings protected steel structural members. A 2D thermo-plastic model has been set up by Molkens and Hanus (2017) by considering thermal contribution of non-structural concrete walls to limit the steel temperature rise of the bearing elements in a steel frame system. Kmet et al. (2016) presented an analysis of an industrial hall located on a thermal power plant damaged by fire dramatically using non-destructive and destructive tests of steel and concrete materials, geodetic surveying of selected structural members, numerical modelling and static analysis.

This study developed herein this paper includes the design, manufacturing drawings and calculations of the steel industry structure in Erzurum (39.886448°, 41.269547°) according to AISC360-10, TBDY-2018 and TÇY-2016-7 standards. At the same time, the September 11, 2001 attack on the twin towers in the United States has shown that steel structures are at least as important as the other strength principles in fire protection. In this study, the fire protection of the planned steel structure is also predicted and the ability to resist fire is mentioned (Wang et al., 2015; Wang et al., 2013; Zhang et al., 2012b; Zhang et al., 2012a).

The model is a 60×32 meter industrial building with 11-roof truss and 10 openings. The ridge span is 20 meters and in the case of side protrusions it is 6 meters.

S235 and 490 MPa electrodes were used as steel class. Soil class ZB, Earthquake Ground Motion DD-2 is assumed when constructing the spectrum curve.

Crane design was not made in the structure. The 3D view and front view of the structure taken from the SAP2000 program is shown in Figs. 1 and 2, respectively. A wide variety of joint types and images are shown in Fig. 3.

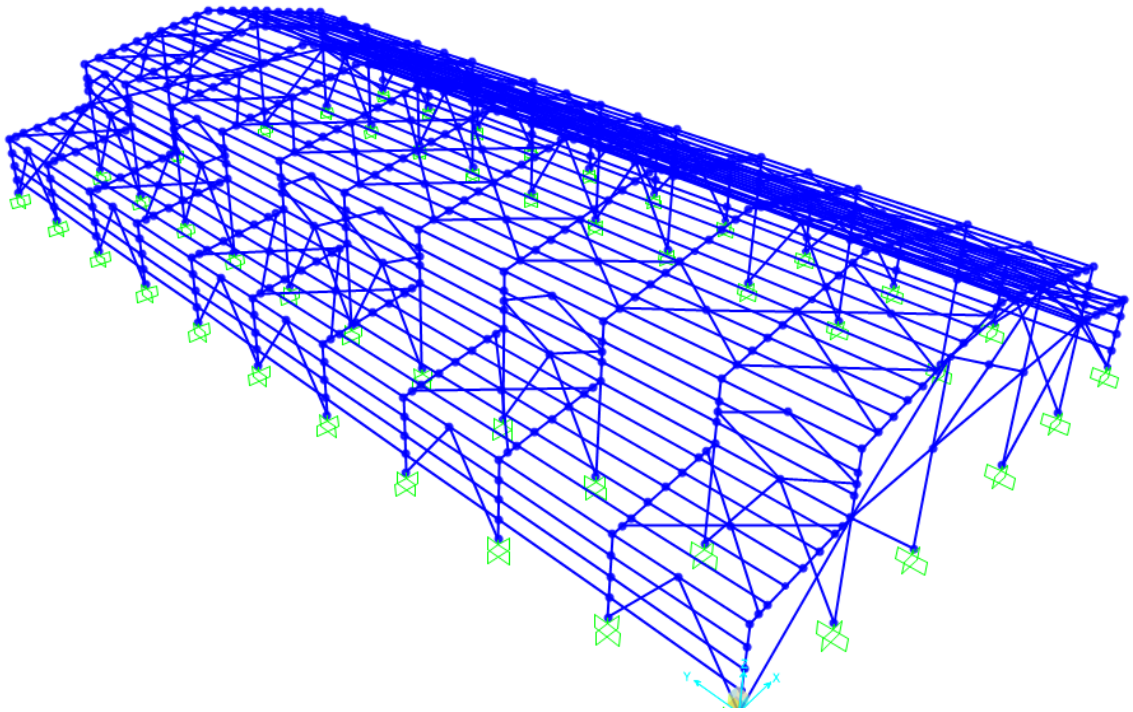

Fig. 1. 3D view of the industrial building.

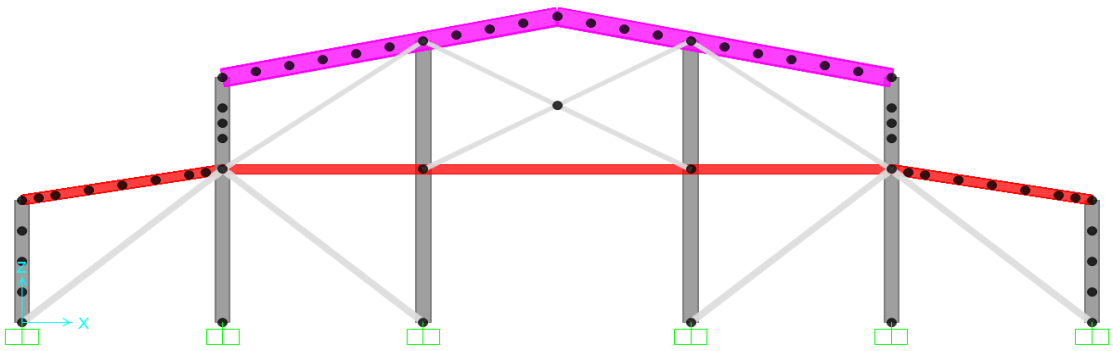

Fig. 2. Front view of the structure.

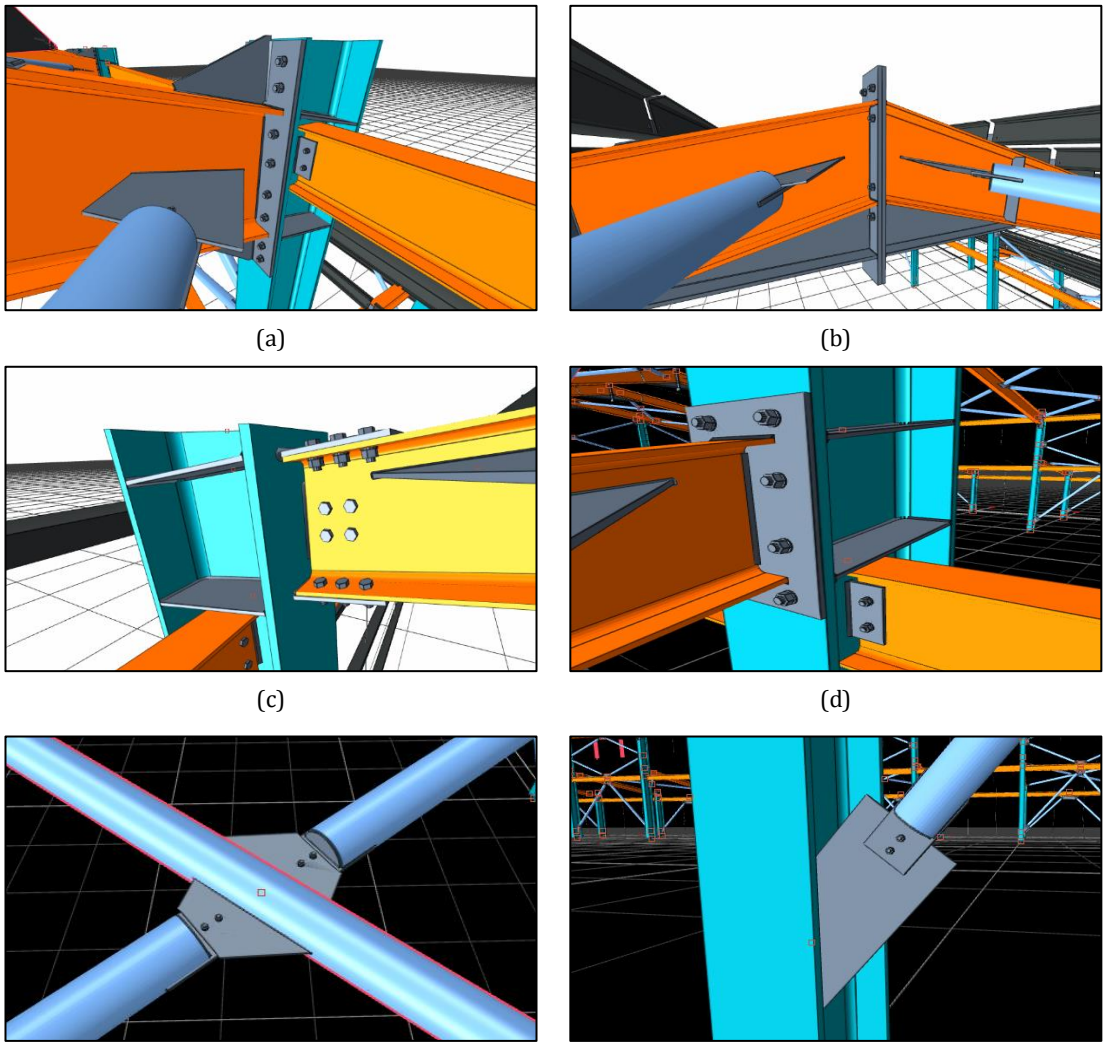

(a) (b) (c) (d) (e) (f)

Fig. 3. (a) Column-beam (ridge) joint with rigid face plate; (b) Beam-beam connection with face plate; (c) Bolt joint with head plate (side ridge 1); (d) Cross-beam junction (side ridge 2); (e) Cross-body combination; (f) Cross-end combination.

2. Determination of Loads

The load calculations required for the model are classified as dead loads (fixed and roofing loads) and moving loads (snow, wind, fire and earthquake loads) and required calculations for the design have been performed with the help of relevant regulations TSE 498, TBDY-2018, ÇYTHY-2016. In this study, fire loads are taken into account in the load combinations by taking 50% of the total of all moving loads that will affect the structure (CEN, 2005). The general load table for the loads calculated and considered for the structure is shown in Table 1.

Table 1. Main loads for the design.

Roofing load (kN/m²)	0.150	
Snow load (kN/m²)	1.950	
Fire load (kN/m²)	1.325	
Wind load in Y-direction (kN/m²)	Input = 0.64	Output = 0.32
Wind load in X-direction (kN/m²)	Input (0-4 m) = 0.40	Output (0-4 m) = 0.20
	Input (4-5 m) = 0.10	Output (4-5 m) = 0.20
	Input (5-8 m) = 0.40	Output (5-8 m) = 0.20
	Input (8-10 m) = 0.13	Output (8-10 m) = 0.32

3. Dimensioning the Structural System

The analysis and design of the system was done in SAP2000. After the necessary material definitions, loads and freedoms were adjusted in the program, changes were made in the design part in accordance with the project design criteria and the sections were dimensioned according to AISC 360/10-LRFD. In addition, framing type, simple moment frame type (OMF), which is suitable for the ductility level of the model, was made in SAP2000 program. Since the earthquake load that will affect the structure is calculated by mode coupling method, the effect of seismic behavior to be created and effected by the selected regulation is limited. The sections obtained as a result of SAP2000 design are presented in Table 2.

Table 2. Dimensioned sections.

Columns	HEB450
Front (facade) purlins	UPN140
Roof purlins	UPN180-200
Diagonals	TUBOD168.3*4-177.8*4
Brace members	S420 Ø0.012 m
Beams between trusses	IPE330
Ridge	IPE600

4. Fire Design

4.1. Thermal properties of steel material

4.1.1. Specific heat (C_{st})

The specific heat-temperature relation is:

If $20°C \leq T_{st} < 600°C$;

$$C_{st} = 425 + 7.73 \times 10^{-1} T_{st} - 1.69 \times 10^{-3} {T_{st}}^2 + 2.22 \times 10^{-6} {T_{st}}^3 \quad (1)$$

If $600°C \leq T_{st} < 735°C$;

$$C_{st} = 666 + \frac{13002}{738 - T_{st}} \quad (2)$$

If $735°C \leq T_{st} < 900°C$;

$$C_{st} = 545 + \frac{17820}{T_{st} - 731} \quad (3)$$

If $900°C \leq T_{st} < 1200°C$;

$$C_{st} = 650 \quad (4)$$

where C_{st} is the specific heat $\left(\frac{\mathrm{J}}{\mathrm{kg}} \cdot \mathrm{K}\right)$.

4.1.2. Thermal conductivity (λ_{st})

The thermal conductivity, specific heat and density of steel structural steel has been obtained from Eurocode 3 Part 1.2 (CEN, 2005).

The thermal conductivity of steel is:

If steel temperature T_{st} (K) is lower than 800°C ;

$$\lambda_{st} = 54 - 3.33 \times 10^{-2} \, T_{st} \quad (5)$$

If steel temperature is higher than 800°C;

$$\lambda_{st} = 27.3 \quad (6)$$

where λ_{st} is the steel thermal conductivity (W/mK). Fig. 4 presents the thermal conductivity of steel-temperature relationship based on EN 1993-1-2.

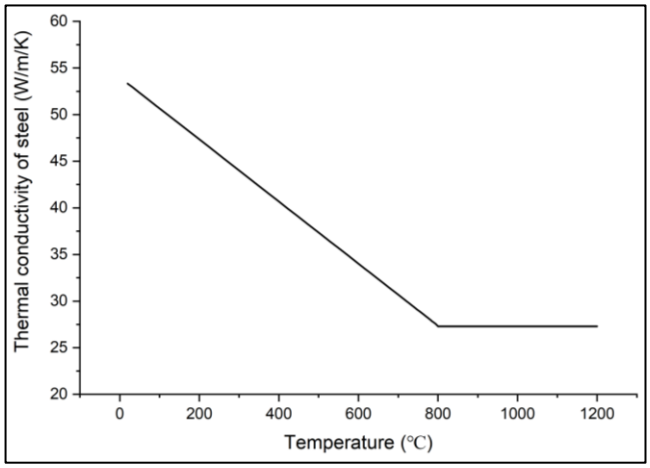

Fig. 4. Variation of thermal conductivity of steel with temperature (CEN, 2005).

4.2. Fire design of unprotected steel

Calculation method for unprotected steel structural element; the heat entering the surface area exposed to heat over a short period of time (Δ_t) is equal to the heat required to raise the temperature of the steel.

$$\varepsilon = \varepsilon_f \times \varepsilon_m \quad (7)$$

Emissivity coefficient (ε) is calculated by multiplying emissivity coefficient under fire condition (ε_f) with emissivity of the material (ε_m).

$$\varepsilon_f = 1.0 \quad \varepsilon_m = 0.5 \quad (8)$$

$$h_{con} = 25 \times (T_{g,t} - T_{st}) \quad (9)$$

$$h_{rad} = \varepsilon_f \times \varepsilon_m \times \sigma \times \times \left[(T_{g,t} + 273.15)^4 - (T_{st,unprotected} + 273.15)^4\right] \quad (10)$$

$$h_{net} = h_{rad} + h_{con} \quad (11)$$

h_{con} – Amount of heat passing through the unit area by convection
h_{rad} – Amount of heat passing through the unit area by radiation
h_{net} – Net (total) heat quantity per unit area
$T_{g,t}$ – Time-dependent fire (gas) temperature
$T_{st,unprotected}$ – Unprotected steel temperature

$$k_{sh} = \frac{0.9\times\left(\frac{A_m}{V}\right)_b}{\left(\frac{A_m}{V}\right)} \tag{12}$$

$$\Delta\theta_{st,t} = k_{sh} \times \frac{\frac{A_m}{V}}{C_{st}\times\rho_{st}} \times h_{net} \times \Delta_t \tag{13}$$

k_{sh} – Temperature correction factor
ρ_{st} – Unit mass of steel material (kg/m^3)
Δ_t – Time interval (sn)
$\Delta\theta_{st,t}$ – Steel temperature rise per unit time

For the time interval, the maximum time specified in Eurocode 3 is 30 s. However, in this study, the temperature calculations were made in 5 second time steps for both protected and unprotected cases to obtain more accurate results.

4.3. Fire design of protected steel

The calculation method is similar to unprotected steel, but the equation is slightly different. Because the heat transfer coefficients are not included in the equation due to the assumption that the outer surface temperature of the fire protection material is the same as the fire gas temperature (Wang, 2002).

$$\emptyset = \frac{C_p\times\rho_p}{C_{st}\times\rho_{st}} \times d_p \times \frac{A_m}{V} \tag{14}$$

$$\Delta\theta_{st,t} = \frac{\lambda_p \times\frac{A_m}{V}}{d_p\times p_{st}\times C_{st}} \times \frac{(T_{g,t}-T_{st,protected})}{\left(1+\frac{\emptyset}{3}\right)} \times \Delta t - \left(e^{\frac{\emptyset}{10}} - 1\right) \times \Delta\theta_{g,t} \tag{15}$$

$\emptyset$ - Shape factor of steel with protection material
λ_p - Thermal conductivity coefficient of fire protection material (W/mK)
C_p – Specific heat of fire protection material (J/kgK)
ρ_p – Unit mass of fire protection material (kg/m^3)
d_p – Thickness of fire protection material (mm)
$\Delta\theta_{g,t}$ – Fire (gas) temperature rise per unit time

4.3.1. Fire protection systems

Many fire protection coatings are produced from calcium silicates or gypsum plasters with low thermal conductivity. Coatings made of calcium silicate are in layers and the inner layer is the least damaging layer in fire. Gypsum plaster coatings have good fire insulation property. Coating systems are very easy to apply, they are applied dry and finished with decorative materials (Fig. 5). However, they are slow and expensive compared to spray applied systems.

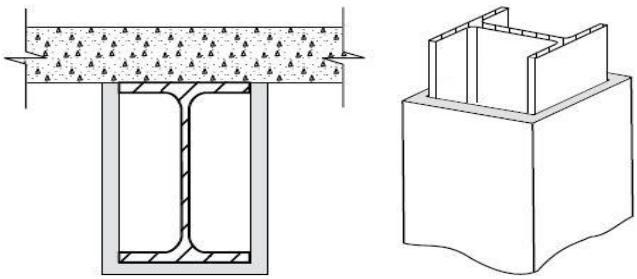

Fig. 5. Panel protection representation.

5. Structural Fire Design

5.1. Column design

In order to facilitate the calculations before moving to the fire design section, the mapping of the columns was performed and then, according to this mapping, both symmetrical columns and the load they would carry could easily be determined by the areas to be exposed to fire.

Box coating was chosen as the fire protection material in the columns.

Since the fire design calculations in steel structures are very long and complicated by hand procedure, fire design program was created by using Microsoft Excel program. Macros section was used in Microsoft Excel. Loads to columns are classified for easier analysis, including inner, edge and corner columns, as the columns will vary according to their position Fig. 6.

SC001	SC002	SC045	SC046	SC003	SC004
SC005	SC006			SC007	SC008
SC009	SC010			SC011	SC012
SC013	SC014			SC015	SC016
SC017	SC018			SC019	SC020
SC021	SC022			SC023	SC024
SC025	SC026			SC027	SC028
SC029	SC030			SC031	SC032
SC033	SC034			SC035	SC036
SC037	SC038			SC039	SC040
SC041	SC042	SC047	SC048	SC043	SC044

Fig. 6. Settlement map of columns in considered industrial structure.

Internal Columns (6-7-10-11-14-15-18-19-22-23-26-27-30-31-34-35-38-39):

Numbered inner columns shown in Fig. 6, span openings, column heights, material properties and most importantly the areas to be exposed to fire were calculated and entered into the developed FIRE_EXCEL spreadsheet as shown in Figs. 7 and 8.

As a result of the analyses, the temperature distributions that will occur in the inner columns under the effect of Standard fire (ISO 834) are shown in Fig. 9 as unprotected and protected against fire. Non-uniform temperature distribution has been obtained for the unprotected members since the specific heat (C_{st}) changes dramatically after around 650°C whereas this behavior has not seemed for the protected members due to the low temperature values. Hence, non-uniform temperature values have been obtained for all unprotected steel members including columns and beams. The application of a 25 mm plasterboard box coating resulted in temperatures less than 550-600°C which were critical temperatures for steel at the end of 1 hour in the inner columns. When we look at the unprotected steel column, it has reached 900°C, which is a critical temperature for the steel to deform and lose its load-bearing capacity.

Edge Columns (2-3-5-8-9-12-13-16-17-20-21-24-25-28-29-32-33-36-37-40-42-43):

20 mm plasterboard fire-protected and unprotected steel temperatures of edge columns are shown in Fig. 10. Since the fire is exposed from the 3 surfaces on the side columns, slightly lower temperatures (temperature difference of 60°C at the end of 60 minute) were obtained than the corner columns. It can be concluded that a slightly thinner fire-retardant material can be used for the side columns.

Corner Columns (1-4-41-44):

For the corner columns, 15 mm plasterboard has been used as the fire protection material to decrease the steel temperatures at the end of fire design time (60 min). As the fire exposure side of these columns is less than the other column types, low insulation thickness might be preferred. The obtained protected steel temperature results are around 500°C which was the aimed design temperature for the steel (Fig. 11).

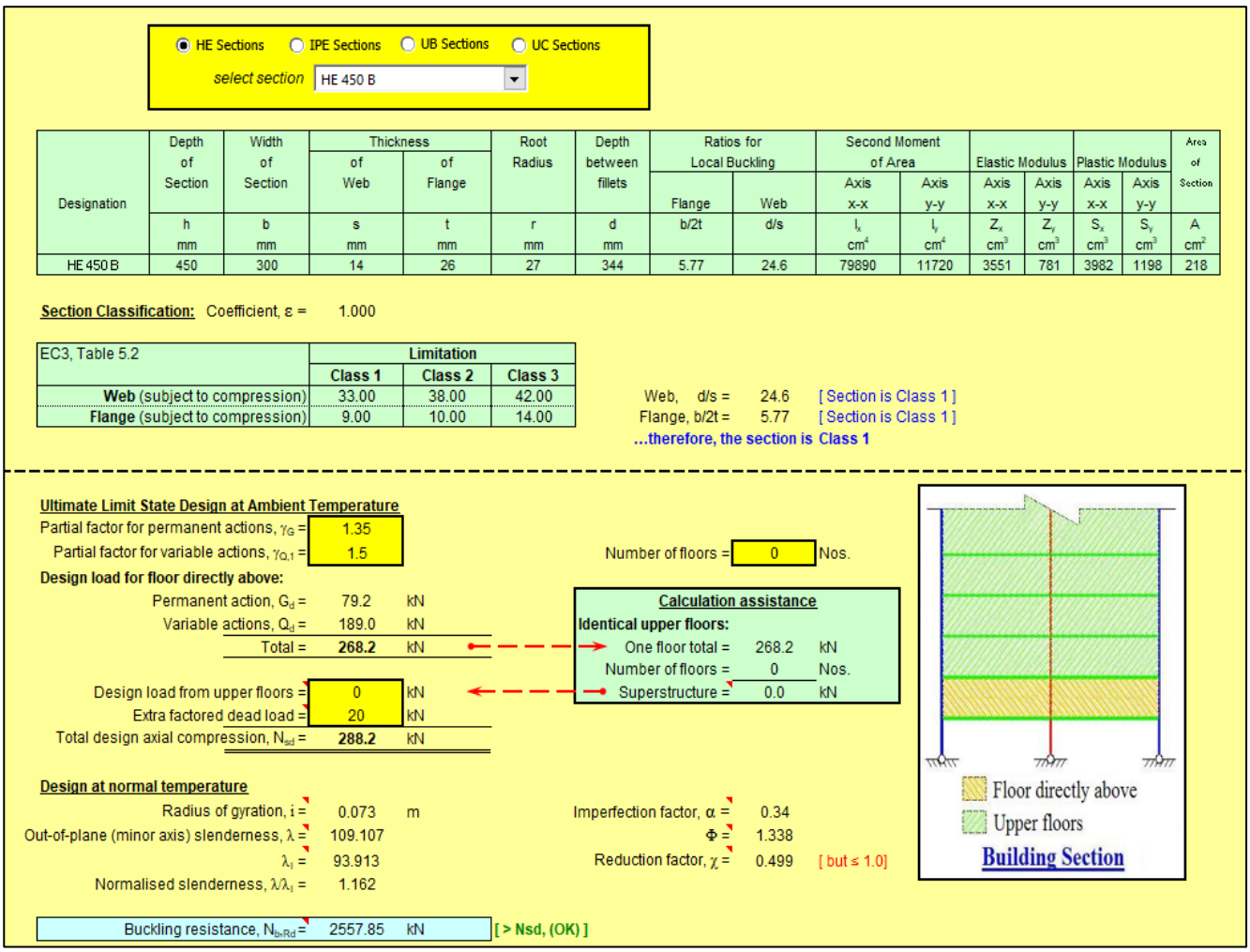

Fig. 7. Entering the necessary properties for fire design of inner columns in FIRE_EXCEL.

HE Sections ○ IPE Sections ○ UB Sections ○ UC Sections

select section: HE 450 B

Designation	Depth of Section	Width of Section	Thickness of Web	Thickness of Flange	Root Radius	Depth between fillets	Ratios for Local Buckling: Flange	Ratios for Local Buckling: Web	Second Moment of Area: Axis x-x	Second Moment of Area: Axis y-y	Elastic Modulus: Axis x-x	Elastic Modulus: Axis y-y	Plastic Modulus: Axis x-x	Plastic Modulus: Axis y-y	Area of Section
	h	b	s	t	r	d	b/2t	d/s	I_x	I_y	Z_x	Z_y	S_x	S_y	A
	mm	mm	mm	mm	mm	mm			cm^4	cm^4	cm^3	cm^3	cm^3	cm^3	cm^2
HE 450 B	450	300	14	26	27	344	5.77	24.6	79890	11720	3551	781	3982	1198	218

Section Classification: Coefficient, ε = 1.000

EC3, Table 5.2	Limitation Class 1	Class 2	Class 3
Web (subject to compression)	33.00	38.00	42.00
Flange (subject to compression)	9.00	10.00	14.00

Web, d/s = 24.6 [Section is Class 1]
Flange, b/2t = 5.77 [Section is Class 1]
...therefore, the section is Class 1

Ultimate Limit State Design at Ambient Temperature

Partial factor for permanent actions, γ_G = 1.35
Partial factor for variable actions, $\gamma_{Q,1}$ = 1.5

Number of floors = 0 Nos.

Design load for floor directly above:

Permanent action, G_d = 79.2 kN
Variable actions, Q_d = 189.0 kN
Total = **268.2** kN

Calculation assistance
Identical upper floors:
One floor total = 268.2 kN
Number of floors = 0 Nos.
Superstructure = 0.0 kN

Design load from upper floors = 0 kN
Extra factored dead load = 20 kN
Total design axial compression, N_{sd} = **288.2** kN

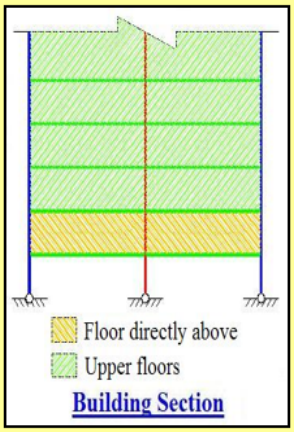

Design at normal temperature

Radius of gyration, i = 0.073 m
Out-of-plane (minor axis) slenderness, λ = 109.107
λ_1 = 93.913
Normalised slenderness, λ/λ_1 = 1.162

Imperfection factor, α = 0.34
Φ = 1.338
Reduction factor, χ = 0.499 [but ≤ 1.0]

Buckling resistance, $N_{b,Rd}$ = 2557.85 kN [> Nsd, (OK)]

Fig. 8. Performing the necessary controls for the column (buckling, etc.).

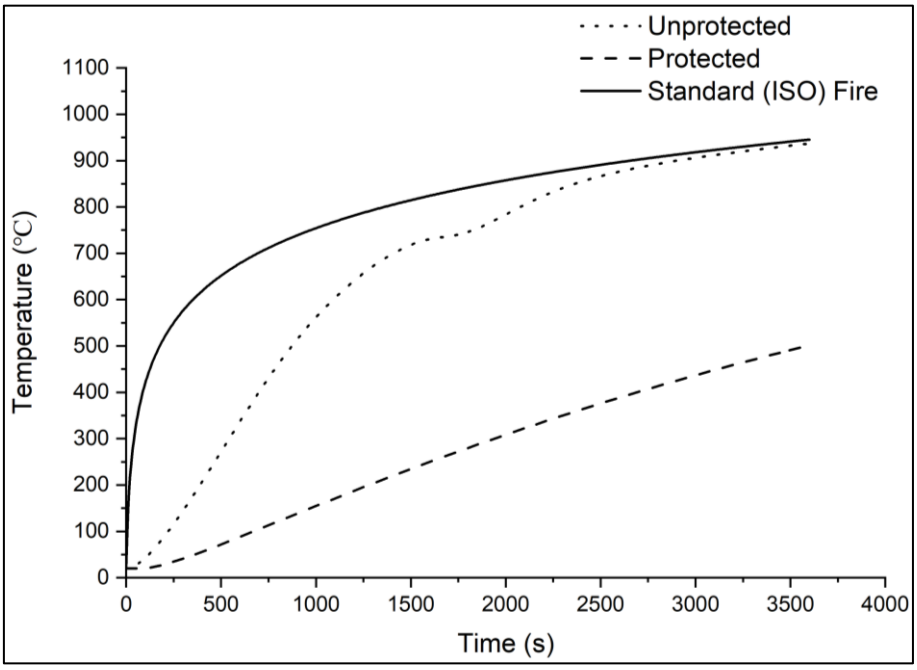

Fig. 9. Temperature distributions for inner columns.

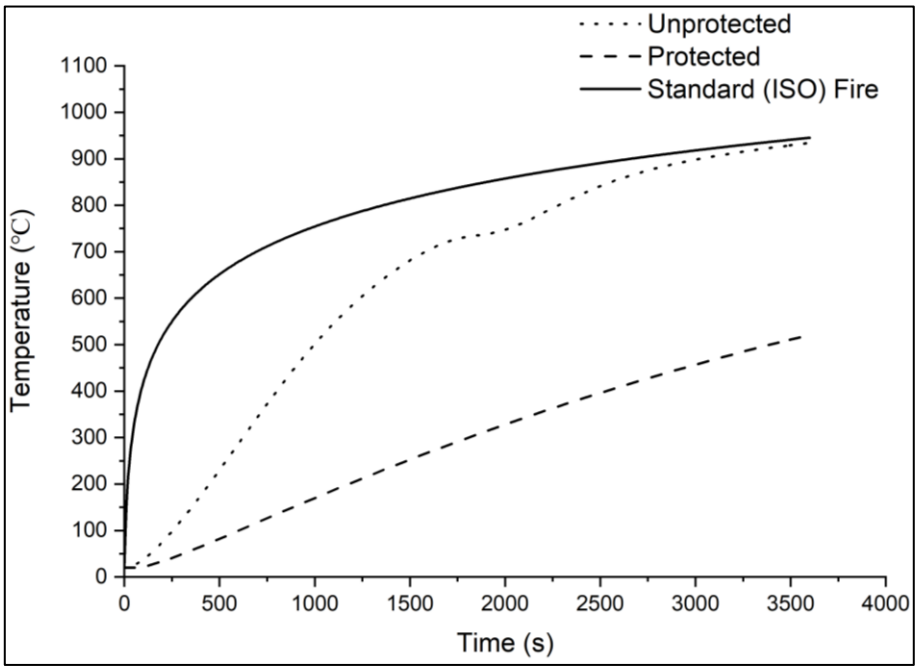

Fig. 10. Temperature distributions for edge columns.

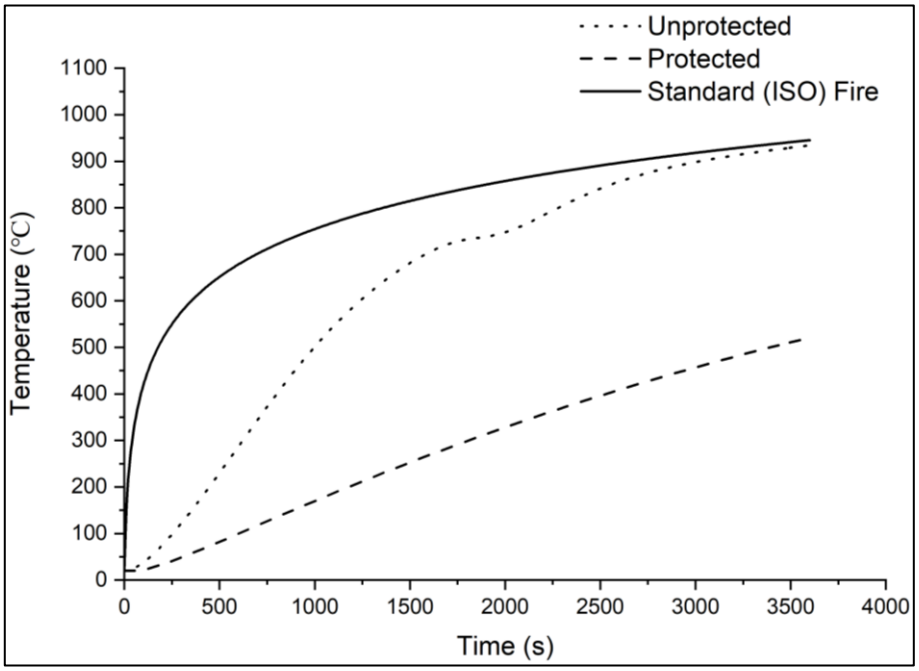

Fig. 11. Temperature distributions for corner columns.

5.2. Beam design

Beam placement map, shown in Fig. 12, is created to provide ease of operation and to make calculations faster and more accurately, just as columns and areas to be used in the fire, loads, and symmetrical beams were determined from this map and colored with the same color. Selected and fire-designed beams are different beams (loading, span openings, etc.) in the system. Different fire performance and temperature distributions were obtained due to differences in physical properties. The remaining beams are symmetrical and identical to the selected beams. Intumescent coating was applied to the beams, as it would be more suitable to manufacture and apply (Cirpici et al., 2016a; Cirpici et al., 2016b), (Cirpici et al., 2019a; Cirpici et al., 2019c; Cirpici et al., 2019d; Cirpici et al., 2019b).

Figs. 14-18 present the temperature distribution on protected and unprotected steel beams designed in the industrial building. Unprotected beam temperatures reach to the fire temperature (ISO-834) within 25 minutes while the protected steel temperatures are kept at around proposed temperature (500°C) by applying 15-20 mm intumescent paint.

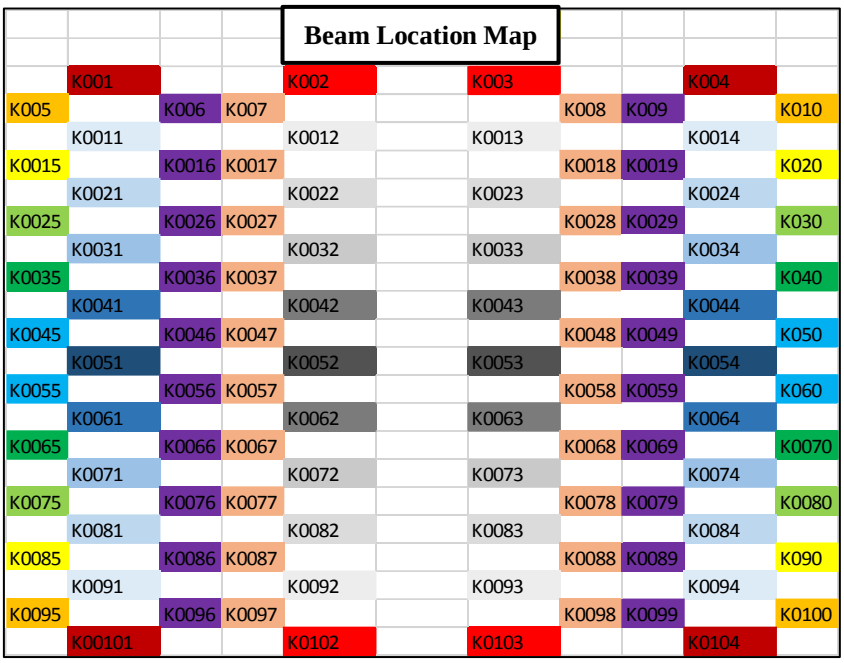

Fig. 14. Settlement map of beams in considered industrial structure.

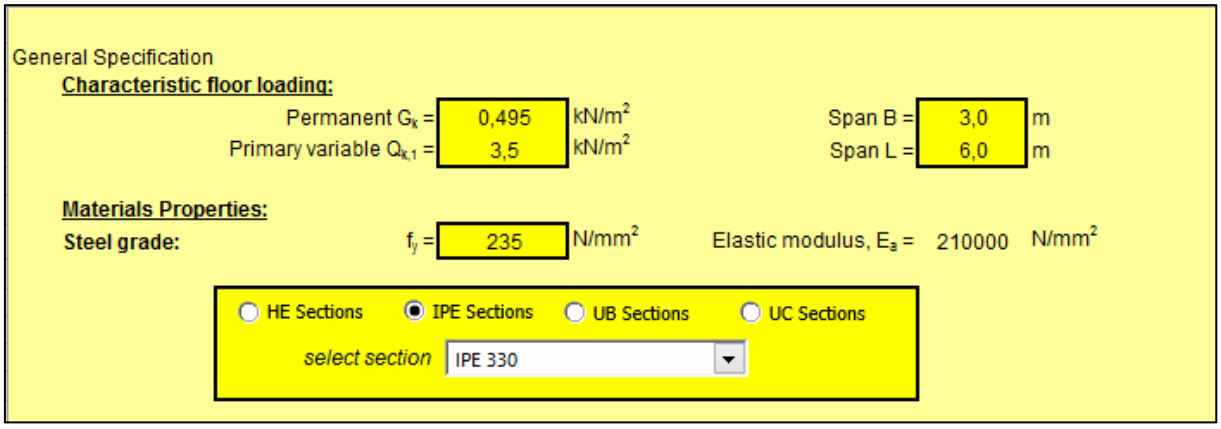

Fig. 13. Entering the necessary properties for fire design of inner columns in FIRE_EXCEL.

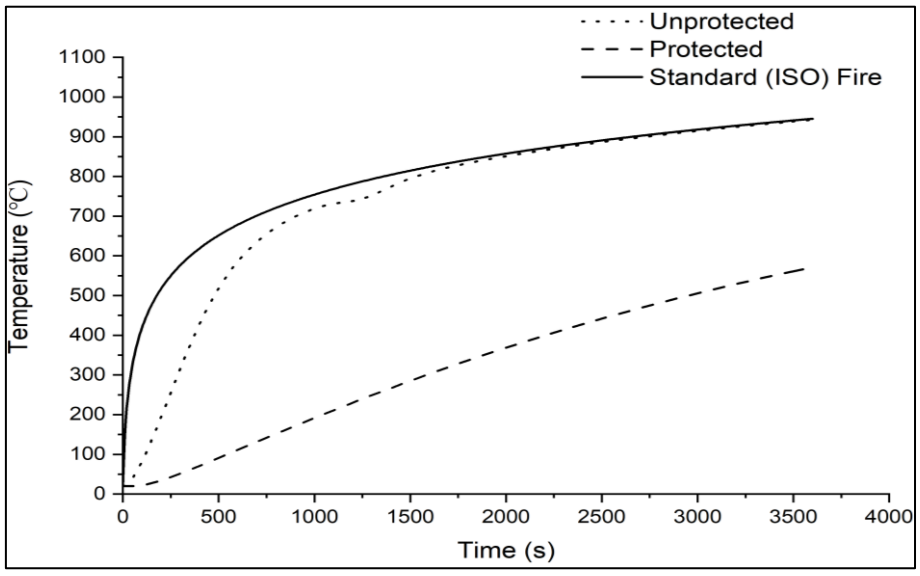

Fig. 14. Temperature distributions on beam numbered as (01).

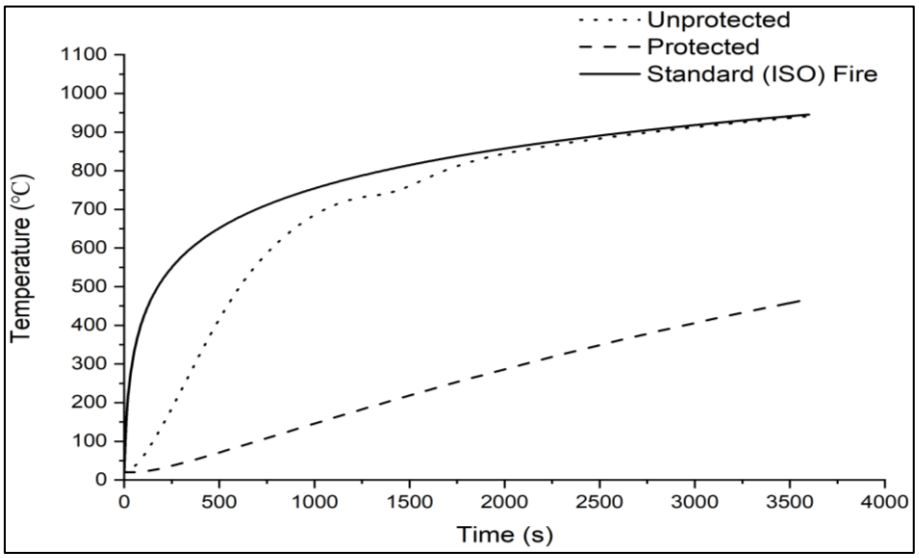

Fig. 15. Temperature distributions on beam numbered as (02).

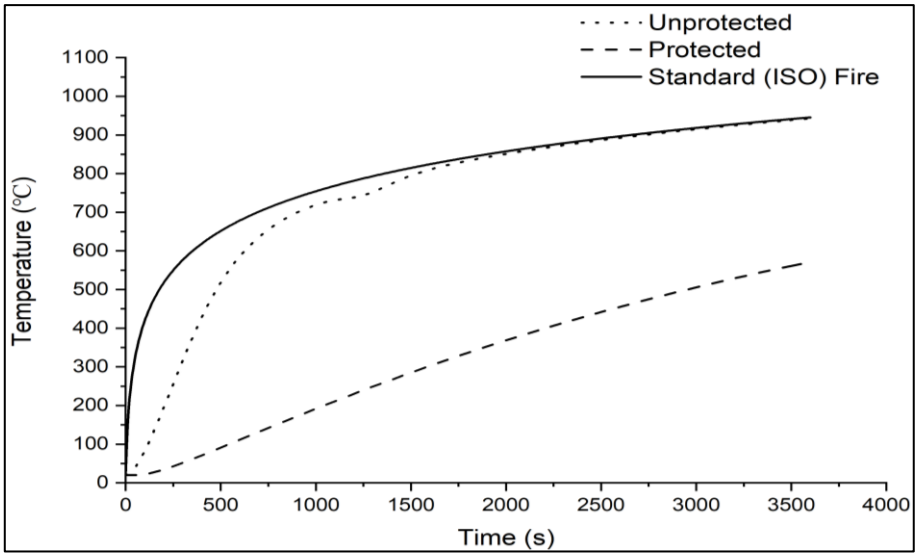

Fig. 16. Temperature distributions on beam numbered as (45-46-47).

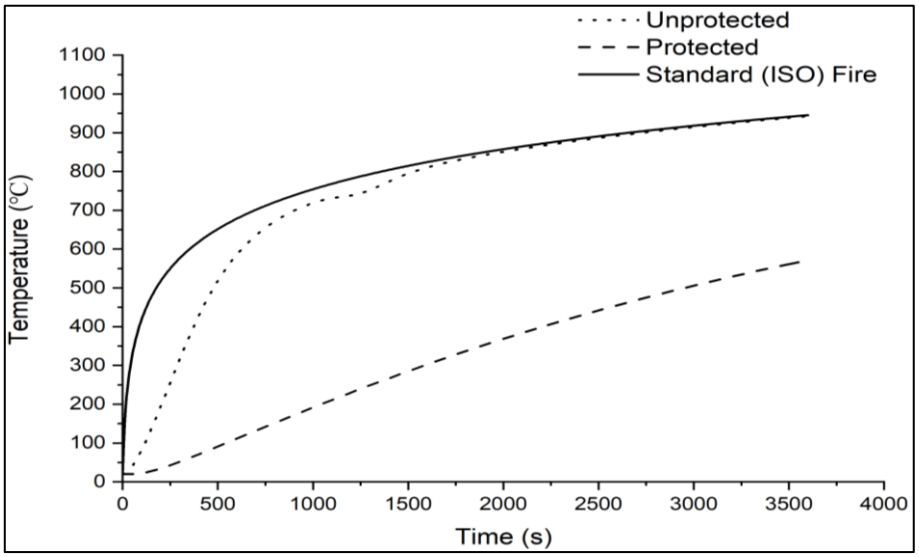

Fig. 17. Temperature distributions on beam numbered as (51).

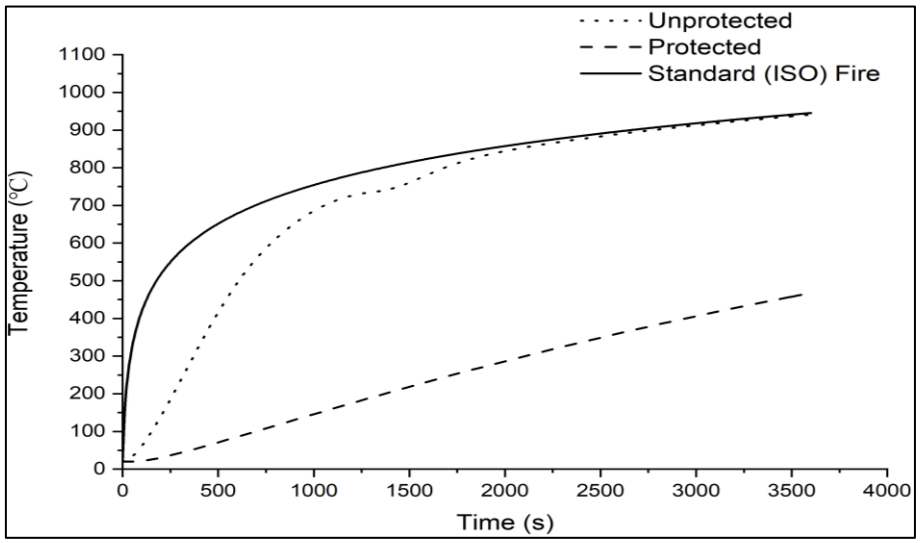

Fig. 18. Temperature distributions on beam numbered as (52).

6. Conclusions

In this study, the behavior of a large steel industrial structure with wide openings under fire effect (Standard Fire - ISO 834) and temperature distributions in the structural elements were determined as fire protected and unprotected. Model analysis, downloads and dimensions, joint calculations and verifications were performed with the help of SAP2000 v18, Tekla Structures 2016i, Idecad 8.62 and IdeaStatica 9 programs. Fire design of columns and beams, which are critical in the fire, among the types of structural elements dimensioned, were made. The thickness of the protection material (plasterboard box protection) in the inner columns was determined as 25 mm, 20 mm in edge columns and 15 mm in corner columns. For the beams, the same intumescent paint protection thickness as 20 mm has been considered for all beams. The load that the columns and beams reach to temperatures of approximately 950°C without protection after 1 hour in a standard fire and is between approximately 450-550°C for the protected steel depending on the load, span openings and fire exposure surfaces. This is the temperature at which the steel begins to lose its strength considerably. When steel rises above these temperatures, more than fifty percent of its strength will be lost, so collapse might be expected. However, the 60-minute design is sufficient for the necessary evacuation.

References

Bilotta A, De Silva D, Nigro E (2017). Structural fire safety of existing steel buildings: Possible general approach and application to the case of the intumescent coatings. *Applications of Structural Fire Engineering*, 80-85.

CEN (2005). EN 1993-1-2: Eurocode 3. Design of Steel Structures. Part 1.2: General Rules - Structural Fire Design. BSI: London.

Cirpici BK, Orhan SN, Kotan T (2019a). Numerical modelling of heat transfer through protected composite structural members. I*nternational Civil Engineering and Architecture Conference 2019 (ICEARC 2019)*, Trabzon, Turkey.

Cirpici BK, Orhan SN, Kotan T (2019b). Numerical modelling of heat transfer through protected composite structural members. *Challenge Journal of Structural Mechanics*, 5(3), 96-107.

Cirpici BK, Orhan SN, Kotan T (2019c). Thermal performance and response of composite slabs profiled with protected steel decking under various fire scenarios. *4th International Conference on Advances in Natural & Applied Sciences (ICANAS 2019)*, Ağrı, Turkey.

Cirpici BK, Orhan SN, Kotan T (2019d). Thermal performance of protected composite slab-beam systems exposed to fire. *3rd International Conference on Advanced Engineering Technologies*, Bayburt, Turkey.

Cirpici BK, Wang YC, Rogers B (2016a). Assessment of the thermal conductivity of intumescent coatings in fire. *Fire Safety Journal*, 81, 74-84.

Cirpici BK, Wang YC, Rogers BD, Bourbigot S (2016b). A theoretical model for quantifying expansion of intumescent coating under different heating conditions. *Polymer Engineering & Science*, 56(7), 798-809.

ÇYTHY-2016 (2016). Çelik Yapıların Tasarım, Hesap ve Yapım Esasları Yönetmeliği. Çevre ve Sehircilik Bakanlığı, Ankara, Turkey.

Kmet S, Tomko M, Demjan I, Pesek L, Priganc S (2016). Analysis of a damaged industrial hall subjected to the effects of fire. *Structural Engineering and Mechanics*, 58(5), 757-781.

Molkens T, Hanus F (2017). Contribution of non-structural concrete walls to the fire resistance of unprotected steel frames. *Applications of Structural Fire Engineering*, 86-91

Piroglu F, Baydogan M, Ozakgul K (2017). An experimental study on fire damage of structural steel members in an industrial building. *Engineering Failure Analysis*, 80, 341-351.

TBDY-2018 (2018). Türkiye Bina Deprem Yönetmeliği. Deprem Etkisi Altında Binaların Tasarımı için Esaslar. Afet ve Acil Durum Yönetimi Başkanlığı, Ankara, Turkey.

TS-498 (1997). Yapı Elemanlarının Boyutlandırılmasında Alınacak Yüklerin Hesap Değerleri. Turkish Standard Institute, Ankara, Turkey.

Wang L, Dong Y, Zhang C, Zhang D (2015). Experimental Study of Heat Transfer in Intumescent Coatings Exposed to Non-Standard Furnace Curves. *Fire Technology*, 51(3), 627-643.

Wang LL, Wang YC, Yuan JF, Li GQ (2013). Thermal conductivity of intumescent coating char after accelerated aging. *Fire and Materials*, 37(6), 440-456.

Wang YC (2002). Steel and Composite Structures - Behaviour and Design for Fire Safety. Spon Press, London, UK.

Zhang Y, Wang YC, Bailey CG, Taylor AP (2012a). Global modelling of fire protection performance of an intumescent coating under different furnace fire conditions. *Journal of Fire Sciences*, 31(1), 51-72.

Zhang Y, Wang YC, Bailey CG, Taylor AP (2012b). Global modelling of fire protection performance of intumescent coating under different cone calorimeter heating conditions. *Fire Safety Journal*, 50, 51-62.

Challenge Journal of Structural Mechanics

Research Article

Moment-rotation behavior of semi-rigid web cleat connections

Merve Sağıroğlu [a], Mahyar Maali [a], Abdulkadir Cüneyt Aydın [b,*], Mahmut Kılıç [b]

[a] *Department of Civil Engineering, Erzurum Technical University, 25050 Erzurum, Turkey*
[b] *Department of Civil Engineering, Atatürk University, 25240 Erzurum, Turkey*

ABSTRACT

The behavior of beam-column semi-rigid connection plays an important role in the response of a steel moment resisting, stiffness and rotation capacity framed structure, especially under static loading conditions. In this study, the moment-rotation characteristics of semi-rigid bolted connections using web cleat connections with IPE standard profile is discussed, based on the experimental investigation. The study revealed that the moment resistance of beam-column semi-rigid connection is improved by increasing the height of the beam to the height of web cleat joint (H), and the increasing thickness of web and flange in web cleat joints. The aim was to provide necessary data to improve the Eurocode 3 and efficiently use residue IPE standard profiles, rather than send them back to the consumption cycle. While the resistance moment increased with an increase in H from H_{min} to H_{max}.

ARTICLE INFO

Article history:
Received 8 January 2020
Revised 3 February 2020
Accepted 24 February 2020

Keywords:
Moment-rotation curve
Semi-rigid connection
Web cleat connection
Joint
Rotation capacity
Eurocode 3

1. Introduction

Experimental tests can be used to obtain the moment-rotation curve of beam-column joints, but it is too expensive for everyday design. The behavior of beam-column semi-rigid connection plays an important role in the response of a steel moment resisting, stiffness and rotation capacity framed structure, especially under static loadings. The use of semi-rigid connections provides a good response under static loadings. It is necessary to consider the behavior of connections in the design and analysis of steel frames because it represents the actual behavior (Sağıroğlu and Aydin, 2015). In addition to considering the behavior of connections in the main axes, some researchers (Lima et al., 2002) considered the behavior of minor axis beam-to-column connections. In the last decade, many researchers were carried out to study the behavior of semi-rigid web cleat connections. Table 1 presents some experimental research of beam-column web cleat connections. T-shaped combinations created using the IPE standard profile and T-shaped elements are different from those in the literature, which utilize welded plates. Thus, the elimination of the problems occurring at the welds of connections such as the occurrence of fracture points and the inability to perform well in place is expected. To recommend the use of weld-less T connections, a knowledge of their behavior is needed. However, web cleat connections that use the IPE standard profile are not mentioned and investigated in either Eurocode 3 or the literature, as in this research (Eurocode 3 investigated cleat leg connections in the section bolted T-stubs). Thus, the aim of this study was to analyze the influence of T connections that utilize the IPE standard profile and the height of beam to height of web cleat joint (H) of web cleat joints on the behavior of steel connections, to provide the necessary data to improve Eurocode 3 (section 3.5.2. Bolted T-stubs which investigated cleat leg connections) and efficiently use residue IPE standard profiles, rather than send them back to the consumption cycle. Moment-rotation curves were used to predict the main characteristics of the relevant connections, such as the resistance moment, the rotation capacity, the stiffness, and the energy dissipation.

2. Experimental Investigation

2.1. Specimens

The experimental program is presented in Fig. 1 and Table 2. This paper presents, the nine experimental

* *Corresponding author*. Tel.: +90-442-231-4781 ; Fax: +90-442-231-4910 ; E-mail address: acaydin@atauni.edu.tr (A. C. Aydın)
ISSN: 2149-8024 / DOI: https://doi.org/10.20528/cjsmec.2020.03.002

models were developed to predict of the behavior of bolted web cleat semi-rigid connections with IPE standard profile under statically loaded in three groups: C300, C270, and C240 groups (C300 cut from of IPE300 standard Profile, C270 cut from of IPE270 standard Profile, and C240 cut from of IPE240 standard Profile). The behaviors of the web cleat joints were compared within their groups (C300-H_{max}, C300-H_{min}, C300-H_{av}, C270-H_{max}, C270-H_{min}, C270-H_{av}, C240-H_{max}, C240-$H_{min,}$ and C240-H_{av}) (H = height of beam to height of web cleat joint). Column stiffeners with a thickness equal to 10 mm were welded to the column by means of a continuous 45° fillet weld. Thus, columns with a large cross-section were chosen, and the use of the stiffener prevented excessive deflection in the flange column (Maali et al., 2017). The plate stiffener was S355 and web cleat profile, and the steel type was S235. HE160B was used for the columns, and IPE240 was selected for the beams. Hand-tightened full-threaded grade 8.8 M14 bolts in 16-mm drilled holes were used consistently for all the tested specimens. The aim of this study was to analyze the influence of T connections that utilize the IPE standard profile and the height of beam to height of web cleat joint (H) of web cleat joints on the behavior of steel connections, to provide the necessary data for improving Eurocode 3 (section 3.5.2. Bolted T-stubs which investigated cleat leg connections) and efficiently use residue IPE standard profiles, rather than send them back to the consumption cycle.

2.2. Material properties

The coupon tension test of the column stiffener, web cleat profile, column, flange and web of the beam, and the mechanical properties of the bolt material were performed in accordance with the relevant standards (UNE-EN 10002-1, 2002). The characteristic of steels and bolts (8.8) are presented in Table 3.

2.3. Test setup

The applied force is static and applied by a 900 kN hydraulic jack with 300 mm maximum piston stroke and a constant displacement speed of 0.01 mm/s until the collapse. To prevent the torsion of the beam, a two-column guide close to the beam was used (Aydın et al., 2015a, 2015b). Merely, the experiments did not exhibit lateral torsion. The testing equipment is shown in Fig. 2. According to relevant given literature, and to obtain more realistic behavior with the specific testing machine the beam and column lengths are chosen as 1500 mm (Aydın et al., 2015a, 2015b).

The main requirements for the instrumentation were measurements of (1) the applied load (P), which was measured using a load cell and hydraulic pump; (2) the displacements (DT) of the connection, beam, web cleat joint, and flange of the column, which were measured using linear variable displacement transducers (LVDT) with a maximum displacement of 100 mm (Figs. 2,3); and the strains at the web cleat connections, which were measured using strain gauges (TML YEFLA-5 (a maximum strain of 15%–20%)) (Maali et al., 2012, 2018, 2019; Fatemi et al., 2013; Niloufari et al., 2014). A data logging device recorded all of the measurements and load cell values at 1-s intervals during the tests. Four strain gauges (ST) were added to the web cleat connection, to observe the strain distribution (Fig. 1). All of the tests used the same arrangement for the locations of the strain gauges and measuring devices.

Nomenclature

h	Height of web cleat joint
h_y	Height of the beam without thickness of flange
H	Web cleat ratio (h_y/h)
F_u	Ultimate or tensile stress
F_y	Yield stress
E_{st}	Strain hardening modulus
$\rho_y=f_y/f_u$	Yield ratio
ε_{st}	Strain at the strain hardening point
ε_{uni}	Uniform strain
ε_f	Strain at rupture load,
X	Cartesian axis; distance
E	Young's modulus
I	Moment of inertia
M	Bending moment
$M_{j.Rd}$	Joint flexural plastic (design) resistance
$M_{j.\max}$	Maximum bending moment
$M_{\min.K-R}$	Lower resistance bound of the knee-range of the joint moment-rotation curve
$M_{\sup.K-R}$	Upper resistance bound of the knee-range of the joint moment-rotation curve
$M_{\Theta.Cd}$	Bending moment at fracture of the joint
P	Concentrated force
$S_{j.ini}$	Initial rotational stiffness of a joint
$S_{j.p-1}$	Post-yield rotational stiffness of a joint
Θ_{Cd}	Rotation capacity of a connection
$\Theta_{Mj.\max}$	Rotation of the connection at maximum load
$\Theta_{M.j.Rd}$	Connection rotation analytical value at which the moment resistance first reaches $M_{j.Rd}$
$\Theta_{\min.K-R}$	Rotation between the lower bound of the knee-range of the joint moment-rotation curve and the rotation capacity
$\Theta_{\sup.K-R}$	Rotation between the upper bound of the knee-range of the joint moment-rotation curve and the rotation capacity
$\Psi_{j.\max\ load}$	Joint ductility index evaluated for the rotation at maximum load
Ψ_j	Joint ductility index
Θ	Rotation
DT_i	LVDT
ST_i	Strain gauge

Table 1. Beam-column web cleat connections.

Author(s) and Year	Explanation	Experimental number
Coelho et al. (2004)	Experimental assessment of the behavior of bolted T-stub connections made up of welded plates	32
Piluso and Rizzano (2008)	Experimental analysis and modeling of bolted T-stubs under cyclic loads	1

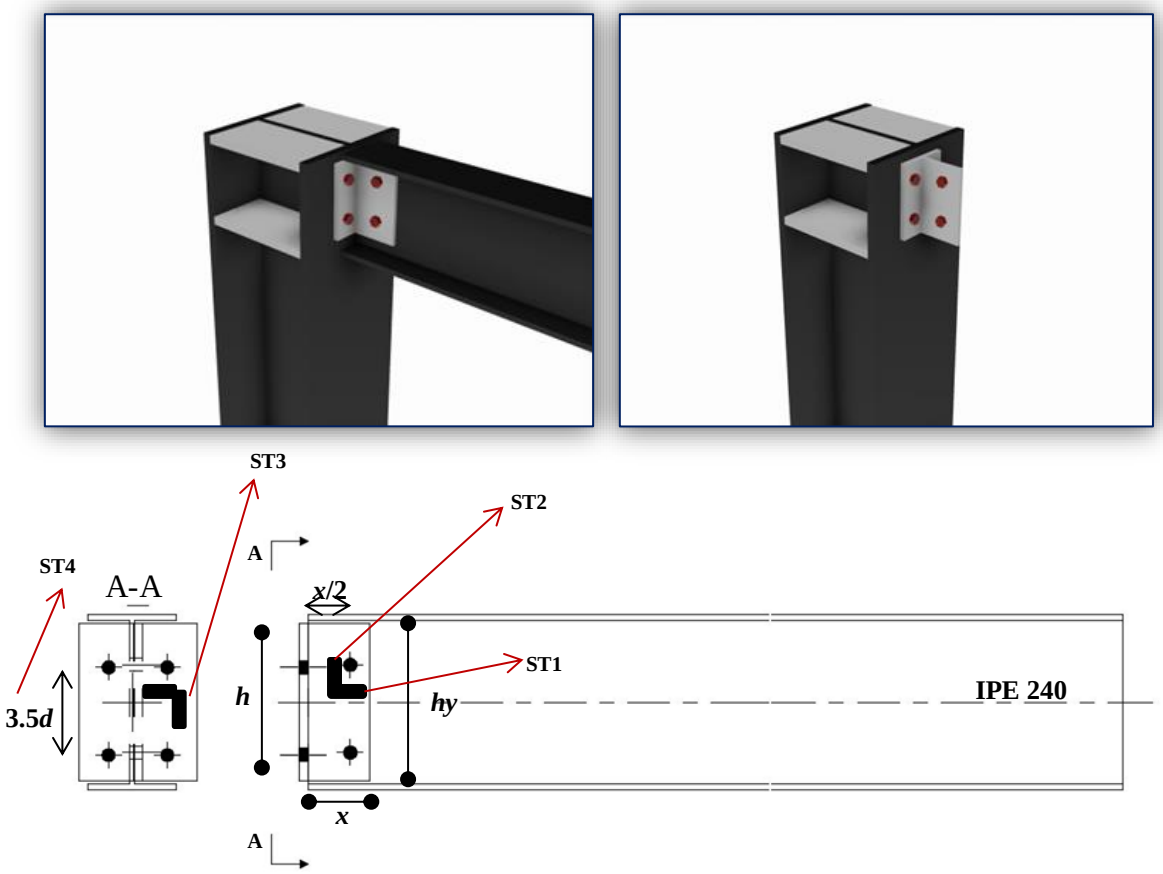

Fig. 1. Web cleat geometry, proposed semi-rigid connection, and locations of strain gauges (ST1 = parallel to beam on Web cleat; ST2 = perpendicular to beam on Web cleat; ST3 = parallel to the column on Web cleat; ST4 = perpendicular to the column on Web cleat; *d* = diagonal to bolts).

Table 2. Test details.

Groups Name	Experiment	Web cleat joint	$H_{max}=hy_{max}/h$	$H_{min}=hy_{min}/h$	$H_{av}=Hy_{av}/h$	X (mm)
C300 group	C300-H_{max}	IPE 300	1	-	-	89
	C300-H_{min}		-	0.63	-	
	C300-H_{av}		-	-	0.82	
C270 group	C270-H_{max}	IPE 270	1	-	-	
	C270-H_{min}		-	0.63	-	
	C270-H_{av}		-	-	0.82	
C240 group	C240-H_{max}	IPE 240	1	-	-	
	C240-H_{min}		-	0.63	-	
	C240-H_{av}		-	-	0.82	

h_y=height of the beam without the thickness of the flange, h=height of Web cleat joint, av= average, max=maximum, min= minimum, x=length of Web cleat connection.

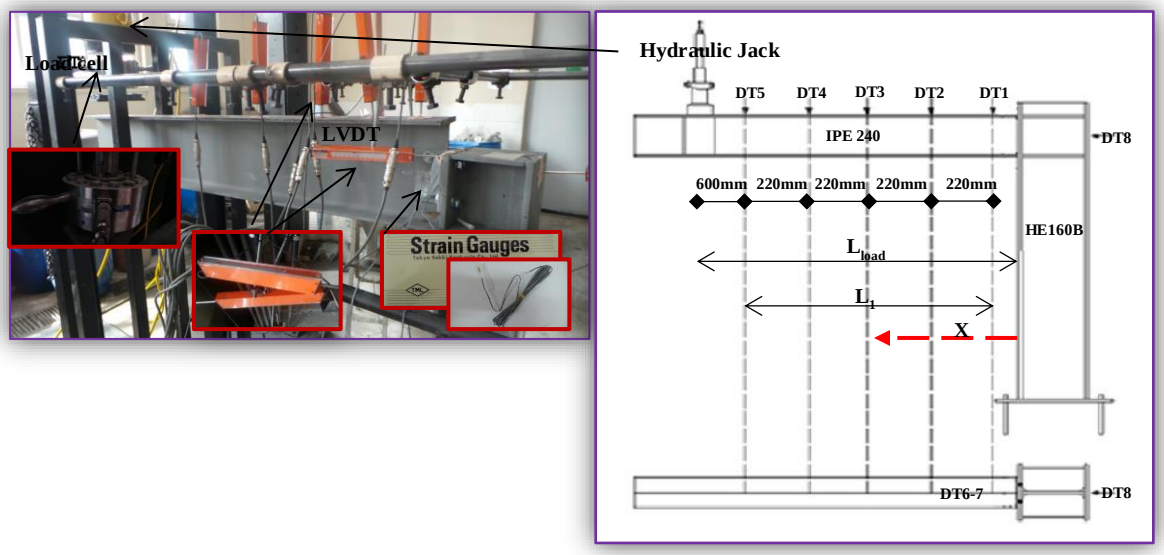

Fig. 2. Test set-up.

Table 3. Average characteristic values for structural steels and bolt (8.8).

	E (MPa)	E_{st} (MPa)	f_y (MPa)	f_u (MPa)	$\rho_y = f_y/f_u$	ε_{st}	ε_{uni}	ε_f
10 mm plate	205352	1798	687	721	0.95	2.71×10^{-2}	2.68×10^{-2}	1.62×10^{-1}
Bolt	-----	-----	1127	1247	0.90	-----	-----	-----
Beam Web	203521	1374	521	649	0.80	1.81×10^{-2}	1.59×10^{-2}	1.09×10^{-1}
Beam Flange	204399	1399	562	685	0.82	1.97×10^{-2}	1.68×10^{-2}	1.15×10^{-1}
Column Web	204424	1396	541	637	0.85	1.89×10^{-2}	1.63×10^{-2}	1.11×10^{-1}
Column Flange	208242	1928	831	945	0.88	2.99×10^{-2}	2.81×10^{-2}	1.78×10^{-1}
T300-stub web	204121	1425	581	705	0.82	2.18×10^{-2}	1.80×10^{-2}	1.38×10^{-1}
T300-stub Flange	204781	1499	638	735	0.87	2.43×10^{-2}	1.99×10^{-2}	1.69×10^{-1}
T270-stub web	204001	1394	545	671	0.81	1.90×10^{-2}	1.66×10^{-2}	1.13×10^{-1}
T270-stub Flange	204498	1428	588	702	0.84	2.00×10^{-2}	1.70×10^{-2}	1.21×10^{-1}

E= the Young's modulus, E_{st}= the strain hardening modulus, f_y= the static yield, f_u= tensile stresses, ε_{st}= the strain at the strain hardening point, ε_{uni}=the uniform strain, ε_f= the strain at rupture load.

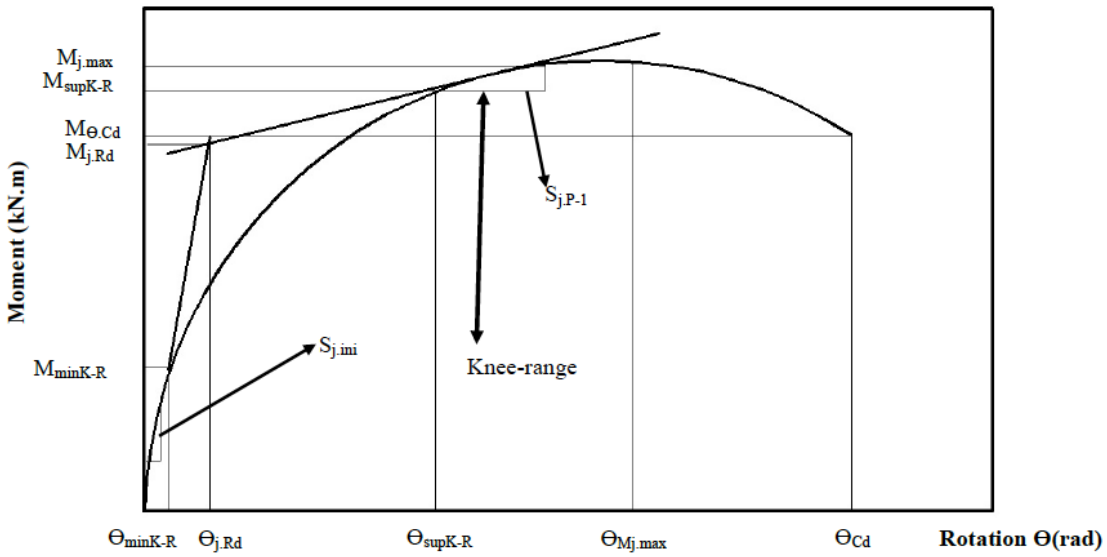

Fig. 3. Typical moment-rotation curve.

The designed connections form various moment-rotation curves that describe the relationship between the applied moment (M) and the corresponding rotation (θ) (Sağıroğlu and Aydin, 2015). The bending moment (M) and the rotation are predicted by using displacements of the beam or top-and-seat angle connection as given below formulation:

$$M = P\,L_{load} \tag{1}$$

The rotational deformation of the joint (θ) is equal to the connection rotation. The beam rotation is approximately given by (Fig. 2.):

$$\theta = \frac{arctan\left(\delta_{DT1}-\delta_{DT5}-\left(-\frac{P}{EI}\right)\left(\frac{X_{DT1}^3}{6}-\frac{L_{load}X_{DT1}^2}{2}\right)\right)}{L1} \tag{2}$$

where I is the moment of inertia and E is Young's modulus of the beam. All deformations values presented throughout the remainder of the section refer to the readings from DT1 (Maali et al., 2015, 2017).

3. Eurocode 3: Moment-rotation curve

The M–θ curve of the connection may be described by using the aforementioned relationships. The main features are the plastic flexural resistance, $M_{j.Rd}$, which corresponds to the intersection point of the previous two regression lines obtained for the initial stiffness ($S_{j.ini}$) and for the post-limit stiffness ($S_{j.p-l}$) and its corresponding rotation $\theta_{M.Rd}$; the maximum bending moment, $M_{j.\max}$, and its corresponding rotation, $\theta_{M.j.\max}$; The knee-range of the M–θ curve, which is defined as the transition zone between the initial and post-limit stiffness, with its lower boundary at $M_{\min k-R}$ and rotation $\theta_{\min k-R}$, and with its upper limit at $M_{\sup k-R}$ and rotation $\theta_{\sup k-R}$; The bending moment capacity, $M_{\theta.Cd}$, and its corresponding rotation capacity, θ_{cd}. In particular, the following characteristics were assessed for the different experimental tests (UNE-EN 10002-1, 2002; Maali et al., 2016; Sağıroğlu et al., 2018), as drawn in Fig. 3:

The ductility of a joint (Ψ_j) reflects the length of the yield plateau of the moment-rotation response. The proposed definition of the ductility of a joint is the difference between the rotation corresponding to the joint plastic resistance, θ_{MRd}, and the total rotation capacity, θ_{Cd} (Schleich et al. 1998; Gil et al., 2003) (Fig. 3). Thus, the joint ductility relates the maximum rotation of the joint, θ_{Cd}, to the rotation corresponding to the joint's plastic flexural resistance, θ_{MRd} (UNE-EN 10002-1, 2002; Piluso and Rizzano, 2008):

$$\Psi_j = \frac{\theta_{Cd}}{\theta_{MRd}} \tag{3}$$

Also, the rotation values at the maximum load and corresponding ductility, $\Psi_{j.\max\ load}$, can be derived from:

$$\Psi_{j.\max\ load} = \frac{\theta_{Mj.\max}}{\theta_{MRd}} \tag{4}$$

Eurocode 3 (2005) gives quantitative rules to obtain the joint flexural plastic resistance and initial rotational stiffness for major beam-to-column joints of end-plate connections. These properties are evaluated below using the geometric and mechanical nominal properties in the Eurocode 3 (Gil et al., 2003).

4. Results and Discussion

The moment-rotation responses for the nine full-scale specimens of steel-bolted, beam-to-column connections with web cleat joints in three groups are reported in Fig. 4 and listed in Tables 4 and 5. Showed that percent of the H characters of all models.

Table 4. Moment–rotation characteristics.

Group	Experiment	KR (knee-range)	Resistance (kN.m)			Stiffness (kN.m/rad)			Rotation (rad)					Ψ_j	$\Psi_{j.\max\ load}$	Energy Dissipated (kN.m.rad)
			$M_{j.Rd}$	$M_{j.\max}$	$M_{\theta Cd}$	$S_{j.ini}$	$S_{j.p-l}$	$S_{j.ini}/S_{j.p-l}$	$\theta_{M.Rd}$	$\theta_{Min.K.R}$	$\theta_{M\sup.k.R}$	$\theta_{Mj.\max}$	Θ_{Cd}			
C300	C300-$H_{\max}$	1.67-8.34	4.93	10.3	10.29	1.82	0.39	4.64	0.019	0.0057	0.063	0.09	0.09	4.79	4.79	0.47
	C300-$H_{\min}$	1.79-8.56	4.64	10.1	10.14	0.74	0.63	1.18	0.062	0.033	0.12	0.14	0.14	2.23	2.23	0.70
	C300-H_{av}	1.13-7.85	3.89	10.1	9.96	1.03	0.52	1.99	0.034	0.0083	0.099	0.13	0.14	4.06	3.94	0.70
C270	C270-$H_{\max}$	0.28-9.76	7.68	11.3	11.17	0.95	0.52	1.84	0.039	0.00002	0.055	0.07	0.07	1.79	1.74	0.39
	C270-$H_{\min}$	0.28-10.77	5.44	11.2	11.19	1.04	0.59	1.76	0.049	0.0014	0.12	0.13	0.13	2.55	2.55	0.70
	C270-H_{av}	2.02-6.62	4.91	7.84	7.8	9.3	0.28	33.29	0.006	0.0027	0.065	0.10	0.11	17.67	17	0.42
C240	C240-$H_{\max}$	0.88-9.33	2.99	10.6	9.96	2.87	0.64	4.44	0.011	0.000016	0.098	0.11	0.12	10.73	10.45	0.63
	C240-$H_{\min}$	1.23-9.04	4.07	9.97	9.61	1.39	0.58	2.41	0.024	0.0087	0.094	0.10	0.11	4.463	4.30	0.53
	C240-H_{av}	0.47-7.59	4.4	9.06	7.7	1.52	0.63	2.41	0.031	0.0022	0.08	0.099	0.11	3.55	3.19	0.50

Table 5. Percent of the H characteristics of all models.

Group	Experimental	$(M_{j.Rd}\,(H_{max})$- $M_{j.Rd}\,(H_{min}$ and $H_{av}))/$ $M_{j.Rd}\,(H_{max})$	$(M_{j.max}\,(H_{max})$- $M_{j.max}\,(H_{min}$ and $H_{av}))/$ $M_{j.max}\,(H_{max})$	$(\theta_{M.Rd}\,(H_{max})$- $\theta_{M.Rd}\,(H_{min}$ and $H_{av}))/$ $\theta_{M.Rd}\,(H_{max})$	$(\theta_{Mj.max}\,(H_{max})$- $\theta_{Mj.max}\,(H_{min}$ and $H_{av}))/$ $\theta_{Mj.max}\,(H_{max})$	$(\Psi_j\,(H_{max})$- $\Psi_j\,(H_{min}$ and $H_{av}))/$ $\Psi_j\,(H_{max})$	$(\Psi_{j.max\ load}\,(H_{max})$- $\Psi_{j.max\ load}\,(H_{min}$ and $H_{av}))/$ $\Psi_{j.max\ load}\,(H_{max})$
C300	C300-H_{max}	-	-	-	-	-	-
	C300-H_{min}	21	1	69	-	54	54
	C300-H_{av}	6	-	45	3	15	18
C270	C270-H_{max}	-	-	-	-	-	-
	C270-H_{min}	36	31	88	-	-	-
	C270-H_{av}	29	1	20	18	86	86
C240	C240-H_{max}	-	-	-	-	-	-
	C240-H_{min}	-	15	-	-	67	70
	C240-H_{av}	8	6	54	4	59	59

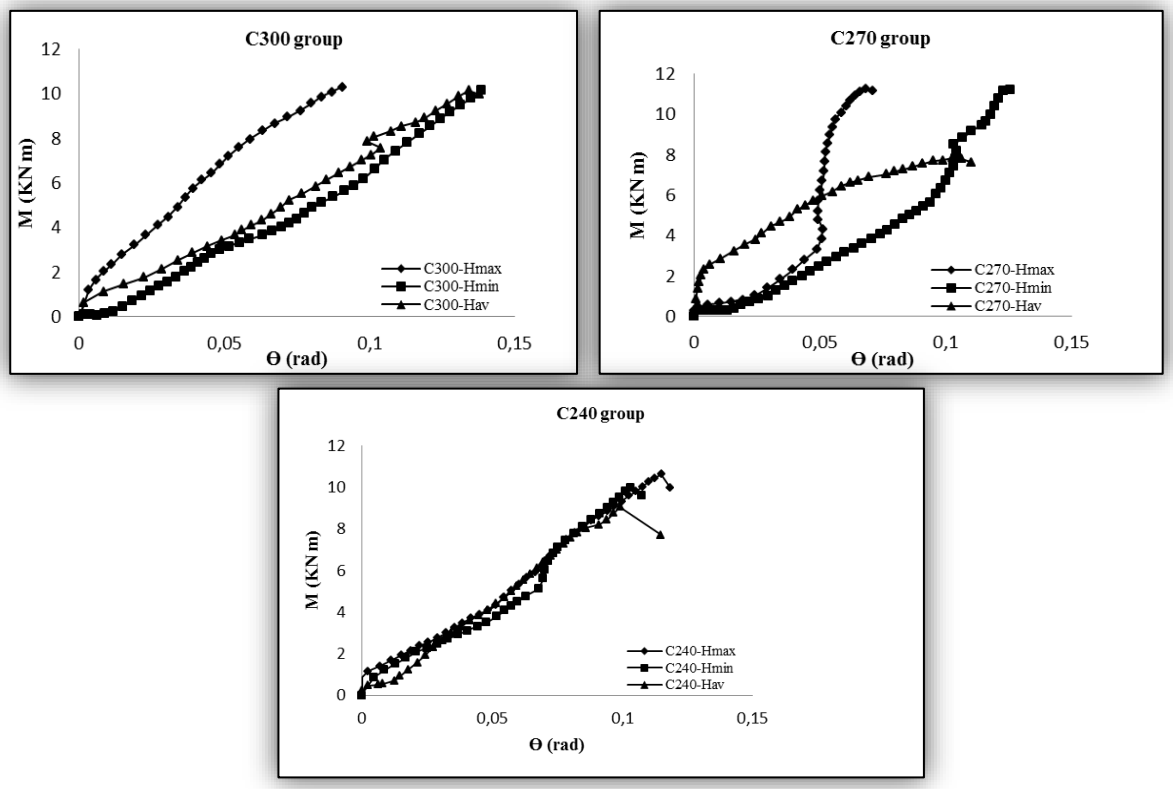

Fig. 4. Moment-rotation curves for three groups.

These curves and tables showed that:

The increasing web cleat ratio (H) increased the plastic flexural resistance about 6%-21%, 29%-36%, and 8%, for all the models. Furthermore, the thickness increase of the joints (from C270 to C300), increased the plastic flexural resistance about 39%–61%, 12%–25%, and 10%, also.

The maximum bending moments of all models increased about 1%, 1%–31%, and 6%–15%, with an increase in the web cleat ratio from H_{min} to H_{max}. Furthermore, the increasing joint thickness (C270 to C300 group of models), increased the maximum bending moments about 6%, 2%–11% and 11%–23%, also. Likewise, the bending moment capacities are increased with the increasing web cleat ratio and joint thickness.

As mentioned above, increasing web cleat ratio, also increased the initial to post-limit stiffness ratio about 41%-75%, 4%-95%, and 46%, for the models C300, C270, and C240, respectively. Moreover, the initial to post-limit stiffness ratios are increased about 4%–60% and 93%, for the increasing joint thickness (C270 to C300). Generally, the rate of the initial stiffness to the post-limit stiffness increased with an increase in the H from H_{min} to H_{max}.

The rotations of the plastic flexural resistance for the C300, C270, and C240 groups decreased by about 45%–69%, 20%–88%, and 54%, respectively, with an increase in H from H_{min} to H_{max}. The rotations of the plastic flexural resistance for the H_{max}, H_{min}, and H_{av} models increased by about 42%–72%, 51%–61%, and 9%, respectively, with an increase of the thickness of the joints (from T270 to T300 group). The maximum rotations for the C300, C270, and C240 groups decreased by about 3%, 18%, and 4%, respectively, with an increase in H from H_{min} to H_{max}. The maximum rotations for the H_{min} and H_{av} model groups increased by about 18%–25% and 26%–39%, respectively, with an increase of the thickness of the joints (from C270 to C300 group).

Meanwhile, the maximum rotation for the H_{max} model decreased by about 21%–41% with an increase of the thickness of the joints (from C270 to C300 group). Generally, the maximum rotation decreased with an increase in H from H_{min} to H_{max}. The rotation capacities for the H_{min} and H_{av} model groups increased by about 9%–23% and 20%–23%, respectively, with an increase of the thickness of the joints (from C270 to C300 group). Meanwhile, the rotation capacities for the H_{max} model decreased by about 23%–41% with an increase of the thickness of the joints (from C270 to C300 group). The Ψ_j (the joint ductility) values for the C300, C270, and C240 groups increased by about 15%–54%, 86%, and 59%–67%, respectively, with an increase in H from H_{min} to H_{max}. The Ψ_j values for the H_{max} and H_{min} models decreased by about 56%–83% and 43%–50%, respectively, with an increase in the thickness of the web and flange in the C240 to C300 web cleat joints. Meanwhile, the Ψ_j values for the H_{av} model increased by about 13%–80% with an increase of the thickness of the joints (from C270 to C300 group). The $\Psi_{j.max.load}$ (the rotation values at the maximum load and corresponding ductility) values for the C300, C270, and C240 groups increased by about 18%–54%, 86%, and 59%–70%, respectively, with an increase in H from H_{min} to H_{max}. The $\Psi_{j.max.load}$ values for the H_{max} and H_{min} models decreased by about 54%–83% and 41%–48%, respectively, with an increase of the thickness of the joints (from C270 to C300 group). Meanwhile, the $\Psi_{j.max.load}$ values for the H_{av} model increased by about 19%–81% with an increase of the thickness of the joints (from C270 to C300 group). The energy dissipations for the C270, and C240 groups increased by about 15%–40%, respectively, with an increase in H from H_{min} to H_{max}. Meanwhile, the energy dissipations for the C270 model decreased by about 33.33% with an increase with an increase in H from H_{min} to H_{max}. The energy dissipations for the H_{min} and H_{av} models increased by about 23%–39%, respectively, with an increase of the thickness of the joints (from C270 to C300 group). Meanwhile, the energy dissipations for the H_{max} model decreased by about 26%–37% with an increase of the thickness of the joints (from C270 to C300 group).

5. Failure Modes and Strain

Fig. 5 shows the moment–strain responses for the nine full-scale specimens of steel-bolted connections with web cleat joints in all groups. According to these curves, there is a correlation between the moment-rotation and moment–strain curves of both tools, which can be taken as further proof of the installation and measurement precision. As can be observed in Fig. 5, at the point of failure for each specimen, all of the strains changed from elastic to plastic for the three groups of specimens. There are three failure modes in the Eurocode 3 for the web cleat connections. Mode 1 is the complete flange yielding without bolt failure. Mode 2 is the flange yielding with bolt failure, and Mode 3 is the bolt failure. The failure modes were observed during the tests: the bolt being directly overloaded by the applied forces on the beam of the Web cleat connection (Mode 3) (Fig. 6). The failure modes of the specimens appeared after necking positions on the beam of the Web cleat connection (Fig. 6).

6. Conclusions

In this study, new connection types were suggested, and their behaviors were determined using full-scale experiments. T-shaped combinations created using the IPE standard profile and T-shaped elements are different from those in the literature, which utilize welded plates. Thus, the elimination of the problems occurring at the welds of connections such as the occurrence of fracture points and the inability to perform well in place is expected. To recommend the use of weld-less T connections, a knowledge of their behavior is needed. However, web cleat connections that use the IPE standard profile are not mentioned and investigated in either Eurocode 3 or the literature, as in this research. Thus, the aim of this study was to analyze the influence of T connections that utilize the IPE standard profile and the height of beam to height of web cleat joint (H) of web cleat joints on the behaviour of steel connections, to provide the necessary data for improving Eurocode 3 and efficiently use residue IPE standard profiles, rather than send them back to the consumption cycle. The main conclusions can be summarized as follows:

- The resistance moment increased with an increase in H from H_{min} to H_{max}.
- The resistance moment increased with the increase in the thickness of the web and flange in the C240 to C300 web cleat joints.
- The rate of the initial stiffness to the post-limit stiffness increased with an increase in the H from H_{min} to H_{max}.
- The rates of the initial stiffness to the post-limit stiffness for the H_{max} and H_{av} model groups increased with an increase of the thickness of the joints (from C270 to C300 group). The rotations of the plastic flexural resistance and the maximum rotations decreased with an increase in H from H_{min} to H_{max}.
- The rotations of the plastic flexural resistance increased with an increase of the thickness of the joints (from C270 to C300 group).
- The maximum rotations and the rotation capacities for the H_{min} and H_{av} model groups increased with an increase of the thickness of the joints (from C270 to C300 group).

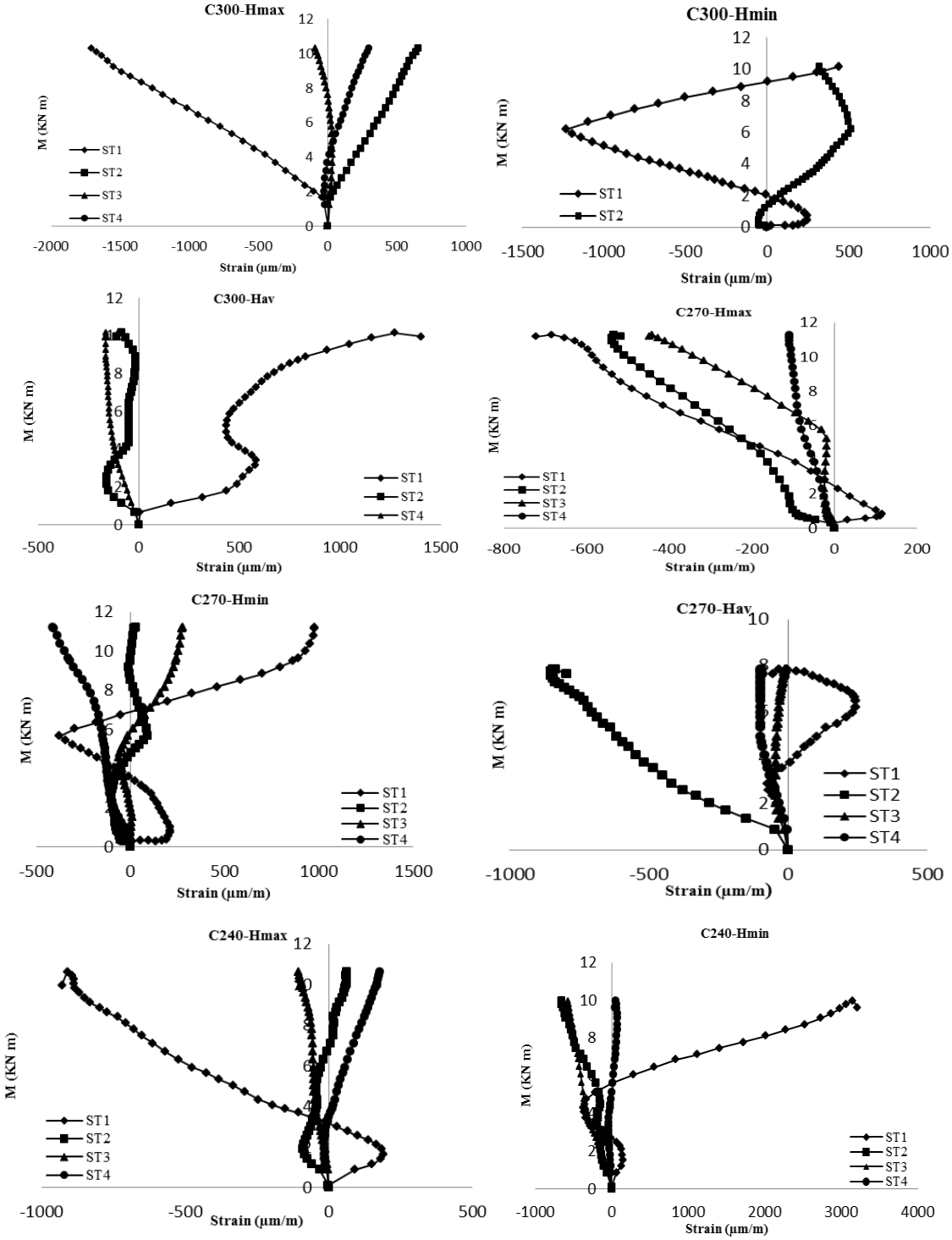

Fig. 5. Moment–strain curves.

- The Ψ_j (the joint ductility) values and the $\Psi_{j.max.load}$ (the rotation values at the maximum load and corresponding ductility) values increased with an increase in H from H_{min} to H_{max}.
- The Ψ_j (the joint ductility) values and the $\Psi_{j.max.load}$ (the rotation values at the maximum load and corresponding ductility) values for the H_{max} and H_{min} models decreased with an increase of the thickness of the joints (from C270 to C300 group). Meanwhile, the Ψ_j (the joint ductility) values and the $\Psi_{j.max.load}$ (the rotation values at the maximum load and corresponding ductility) values for the H_{av} model increased with an increase of the thickness of the joints (from C270 to C300 group). Thus, the model with H_{av} was ideal model.
- The energy dissipations for the C270, and C240 groups increased with an increase in H from H_{min} to H_{max}. Meanwhile, the energy dissipations for the C270 model decreased with an increase with an increase in H from H_{min} to H_{max}. The energy dissipations for the

H_{min} and H_{av} models increased with an increase of the thickness of the joints (from C270 to C300 group). Meanwhile, the energy dissipations for the H_{max} model decreased with an increase of the thickness of the joints (from C270 to C300 group).

- The failure modes were observed during the tests: the bolt being directly overloaded by the applied forces on the beam of the Web cleat connection (Mode 3). The failure modes of the specimens appeared after necking positions on the beam of the Web cleat connection.

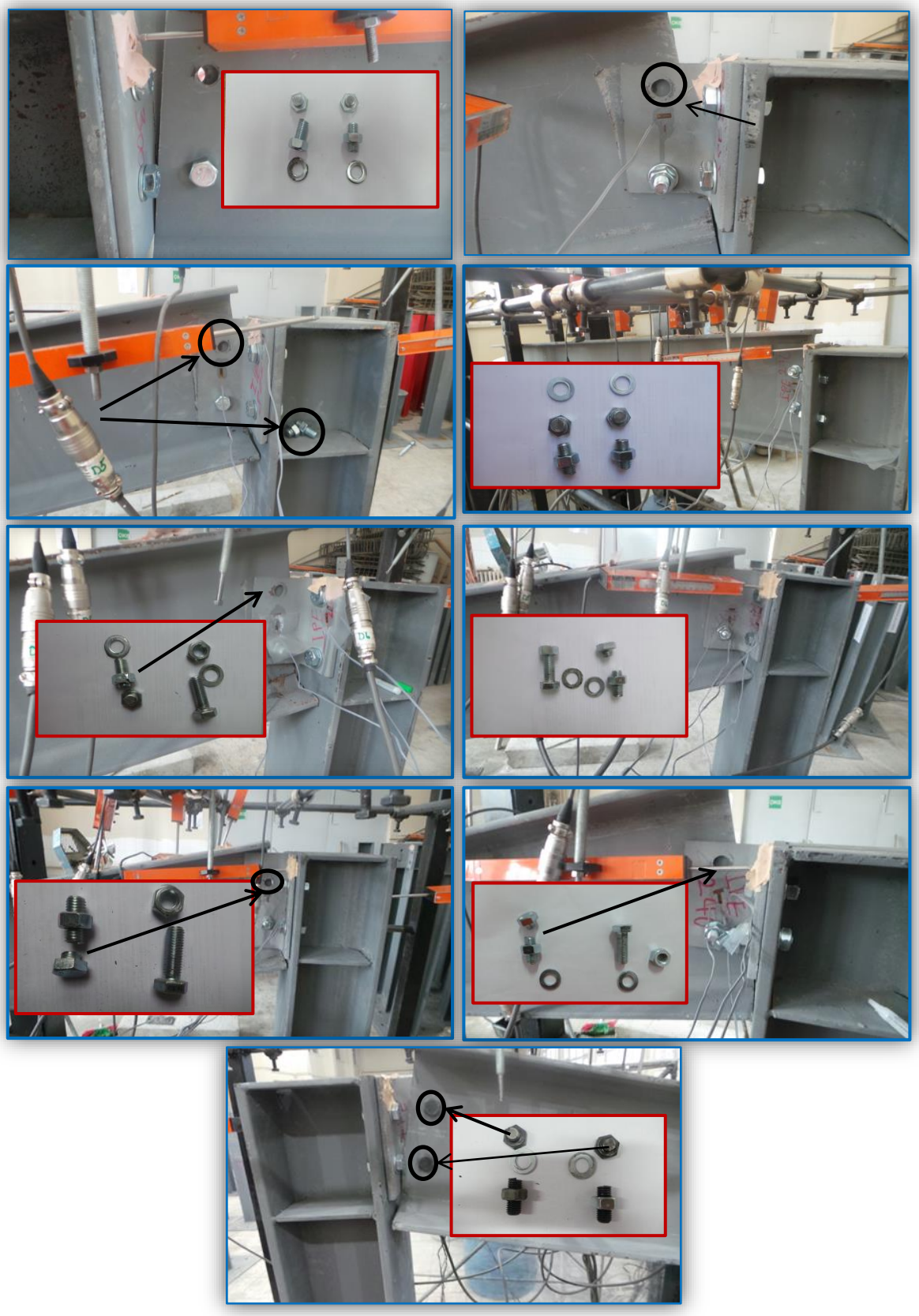

Fig. 6. Failure of models.

Acknowledgements

The writers gratefully acknowledge the financial support given by the BAP project (2015/126) of Ataturk University and the financial support given by the TÜBİTAK (2215) for Mahyar Maali and the support provided by the Gençler Metal steel company in making test specimens available. Their support in conducting the tests is most appreciated.

References

Aydın AC, Kılıç M, Maali M, Sağıroğlu M (2015a). Experimental assessment of the semi-rigid connections behavior with angles and stiffeners. *Journal of Constructional Steel Research*, 114, 338–348.

Aydın AC, Maali M, Kılıç M, Sağıroğlu M (2015b). Experimental investigation of sinus beams with end-plate connection. *Thin-Walled Structures*, 97, 35–43.

CEN (2005). Design of steel structures. Part 1.8: Design of joints, Stage 49 draft. European Committee for Standardization, Brussels.

Coelho AMG, Bijlaard FSK, Gresnigt N, Silva LS (2004). Experimental assessment of the behaviour of bolted T-stub connections made up of welded plates. *Journal of Constructional Steel Research*, 60, 269–311.

EN10002-1 (2001).Metallic materials– tensile testing–part 1: Method of testing at ambient temperature. European Standard, CEN, Brussels.

Fatemi SM, Showkati H, Maali M (2013). Experiments on imperfect cylindrical shells under uniform external pressure. *Thin-Walled Structures*, 65, 14–25.

Gil B, Cabrero JM, Goñi R, Bayo E (2003). An assessment of the rotation capacity required by structural hollow sections for plastic analysis. In: Jaurrieta MA, Alonso A, Chica JA (ed) *Tubular Structures*, A.A. Balkema Publishers, X. Lisse Holland, 277–292.

Lima LRO, Andrade SAL, Vellasco PCGS, Silva LS (2002). Experimental and mechanical model for predicting the behavior of minor axis beam-to-column semi-rigid joints. *International Journal of Mechanical Sciences*, 44, 1047–1065.

Maali M, Aydın AC, Sağıroğlu M (2015). Investigation of innovative steel runway beam in industrial building. *Sadhana - Academy Proceedings in Engineering Sciences*, 40, 2239–2251.

Maali M, Kılıç M, Sağıroğlu M, Aydın AC (2016). Experimental model of the behavior of bolted angles connections with stiffeners. *International Journal of Steel Structures*, 16(3), 719–733.

Maali M, Kılıç M, Sağıroğlu M, Aydın AC (2017). Experimental model for predicting the semi-rigid connections' behaviour with angles and stiffeners. *Advances in Structural Engineering*, 20(6), 884–895.

Maali M, Kılıç M, Yaman Z, Ağcakoca E, Aydın AC (2019). Buckling and post-buckling behavior of various dented cylindrical shells using CFRP strips subjected to uniform external pressure: Comparison of theoretical and experimental data. *Thin-Walled Structures*, 137, 29–39.

Maali M, Sagiroglu M, Solak MS (2018). Experimental behaviour of screwed beam-to-column connections in cold-formed steel frames. *Arabian Journal of Geosciences*, 11(9), 205.

Maali M, Showkati H, Fatemi SM (2012). Investigation of the buckling behavior of conical shells under weld-induced imperfections. *Thin-Walled Structures*, 57, 13–24.

Niloufari A, Showkati H, Maali M, Fatemi SM (2014). Experimental investigation on the effect of geometric imperfections on the buckling and post-buckling behavior of steel tanks under hydrostatic pressure. *Thin-Walled Structures*, 74, 59–69.

Piluso V, Rizzano G (2008). Experimental analysis and modeling of bolted T-stubs under cyclic loads. *Journal of Constructional Steel Research*, 64(6), 655–669.

Sağıroğlu M, Aydin AC (2015). Design and analysis of non-linear space frames with semi-rigid connections. *Steel and Composite Structures*, 18(6), 1405–1421.

Sagiroglu M, Maali M, Kılıç M, Aydın AC (2018). A novel approach for bolted T-Stub connections. *International Journal of Steel Structures*, 18(3), 891–909.

SB EN ISO 898-1:1999 (2009). Mechanical properties of fasteners made of carbon steel and alloy steel: Bolts, screws and stud. (Published: October 1999 Replaced By: SB EN ISO 898-1:2009, Revised, Withdrawn)

Schleich JB, Chantrain P, Chabrolin B, Galéa Y, Bureau A, Anza J, Espiga F (1998). Promotion of plastic design for steel and composite cross sections: New required conditions in Eurocodes 3 and 4, practical tools for designers. European Commission, Luxembourg.

Challenge Journal of Structural Mechanics

Research Article

Blast-induced ground motion effect on dynamic response of a cylindrical vertical water tank with piled raft foundation

Kemal Hacıefendioğlu [a,*], Gökhan Demir [b], Ahmet Can Altunışık [a]

[a] *Department of Civil Engineering, Karadeniz Technical University, 61080 Trabzon, Turkey*
[b] *Department of Civil Engineering, Ondokuz Mayıs University, 55139 Samsun, Turkey*

ABSTRACT

This paper studies to estimate the dynamic behavior of a demineralized water tank with a piled raft foundation system considering soil-pile-structure-fluid interaction to shock-ground motion. A three-dimensional finite element model of a coupled system is constituted in ANSYS software. Interaction between pile and soil is represented with the frictional contact element. The frictionless contact elements are utilized to model between the water and tank shell to allow for displacement of the free surface adjacent to the tank wall. Shell elements are used for the tank body and its vault. The dynamic analyses of the tank including soil-pile-structure-fluid interaction are presented by using shock response spectra. Ground shock acceleration time histories, generated by using a developed computer program based on Fortran programming language, produce shock response spectra. The effects of the different charge weights and distances from the charge center are examined in the analyses. Also, the effect of the water fill level in the tank and the number of piles is also investigated. The results of the research are presented with the directional displacements and equivalent stresses. It seen from the analyses that the dynamic responses of the tank increase with the charge weight, while decreasing with the charge center distance. Moreover, the water fill level and the number of piles extremely affect the displacement and stress values of the coupled interaction system.

ARTICLE INFO

Article history:
Received 26 December 2019
Revised 30 January 2020
Accepted 16 March 2020

Keywords:
Blast ground motion
Charge weight
Shock spectrum analysis
Soil-pile-structure-fluid interaction
Water tank

1. Introduction

Circular storage tanks, such as reinforced concrete/steel water tanks, are widely used to store water, oil and gas. These type tanks transfer loads from liquid and self-weight to a foundation and layers of soil or rock. Storage tanks located in soft soil can easy to be threatened by earthquakes, traffic load, explosion induced ground vibrations. In such situations, it is necessary to study dynamic responses of storage tanks in soft soils during ground motion. A conventional raft foundation under storage tanks constructed in soft soils does not provide adequate support, it can be enhanced by the addition of piles to the reduction of settlement and increase in bearing capacity of the raft.

Limited studies were carried out in analyzing storage tanks considering soil-pile-structure-fluid interaction under seismic excitation. The first study titled "Foundations for Cylindrical Storage Tanks" belongs to Roberts (1961). This study investigated the effect of the types of foundations used for a variety of soil conditions. These foundation solutions include the use of a sand pad, concrete or crushed rock ring wall, an interlocking sheet pile ring wall, and a pile foundation with a crushed rock pile cap. Xinliang and Xuecheng (1992) simulated the soil-pile system as an anisotropic elastic solid. They developed special software to analyze the dynamic behavior of liquid-structure-pile-soil interaction system. Dieterman (1993) presented the effects of the liquid and foundation including pile-soil interaction on the structural

* *Corresponding author*. Tel.: +90-462-377-2669 ; E-mail address: kemalhaciefendioglu@ktu.edu.tr (K. Hacıefendioğlu)
ISSN: 2149-8024 / DOI: https://doi.org/10.20528/cjsmec.2020.03.003

dynamics using an analytical model. Higuchi et al. (2000) described the results of shaking table tests on LNG facilities on the reclaimed land using the centrifuge apparatus. The study investigated the seismic responses of multi-layered grounds and piled foundations of LNG facilities. Ruifu et al. (2011) studied the seismic response of an isolated vertical, cylindrical, extra-large liquefied natural gas (LNG) tank by a multiple friction pendulum system (MFPS). The results showed that the isolation system has excellent adaptability for different liquid levels and is very effective in controlling the seismic response of extra-large LNG tanks. Yamashita et al. (2014) confirmed the validity of the foundation design. They performed field measurements on the foundation settlement and the load sharing between the piles and the raft from the beginning of the construction to 80 months after the end of the construction. Ximei et al. (2014) conducted the dynamic responses of the LNG tank structures under seismic excitation considering the influences of pile-soil interaction, liquid level of LNG, the site classification, direction and intensity of earthquake, and the leakage of LNG liquid. Park et al. (2017) purposed a dynamic centrifuge model test method for the accurate simulation of the behaviors of a liquid storage tank with different types of foundations during earthquakes. The study investigated the effects of the soil-foundation-structure interactions of a simplified storage tank under two different earthquake motions, simulated using a shaking table installed in a centrifuge basket. Cheng and Jing (2017) proposed two simplified methods to quantify the stability of composite foundation treated with a large number of compaction piles. Kim et al. (2017) investigated the cathodic protection design improvement. In this study, the current distribution was studied using the Boundary Element Method (BEM) and the Finite Element Method (FEM) numerical analysis methods. End of the study, it was implemented that the construction cost was reduced significantly without any under-protection area on the steel piles. Ha et al. (2017) performed the dynamic centrifuge tests to observe the seismic behaviors of the liquefied natural gas (LNG) storage tank with different foundation conditions. Two typical foundation types were used as shallow foundation and pile foundation. The accelerations at soil surface, slab and structure were compared. Fiore et al. (2018) researched the influence of sloshing effects and of the soil-structure interaction. Also, the tank founded on piles, soil-structure interaction is taken into account by computing the dynamic impedances. Sahraeian et al. (2018) performed dynamic centrifuge model tests to investigate the mechanical behavior of oil tanks supported by piled raft foundation on liquefiable saturated sand and non-liquefiable dry sand. In the tests, two types of foundations were modelled for oil storage tanks, namely, slab foundation (SF) and piled raft foundation (PRF). Purnama et al. (2018) carried out the study on improvement of foundation structure system with concrete slab supported by piles on the outside around and "Sistem Cakar Ayam" that spread evenly in the area of the foundation. The numerical study of the proposed improvement of structure model was conducted using SAP2000 and ABAQUS. Zhang et al. (2018) studied the seismic response of the tank-fluid system considering soil-structure interaction. A three-dimensional FEM model of soil-pile-structure-fluid interaction system was built based on ANSYS software, in which, the structure and fluid interaction are considered by Lagrangian fluid FEM approximation.

In underground mining and civil engineering, drilling and blasting are generally using excavation techniques. Ground shock and vibrations have been a major problem for the surrounding structures such as buildings, bridges, dams and tunnels, etc. This type of vibration threat can cause cracks or other kinds of damages in buildings and other types of structural systems. Only recently, a limited number of studies have been performed to define the potential threat of blast type loadings on above structures. Some valuable researches are regarding dynamic analyses of water storage tanks against blast ground motion (Blair et al., 2007; Haciefendioğlu et al., 2012).

There is no enough study about the dynamic response of the soil-pile-structure-fluid interaction system under blast ground motion. This study presented the dynamic behavior of a demineralized water tank with a piled raft foundation subjected to blast ground motion, with 3D modeling in ANSYS software (2013). Shock spectra are utilized to determine dynamic response calculations of the coupled system subjected to blast loading. In the analyses, three different charge weights with three different charge centers are taken into account for parametric studies.

2. Shock Response Spectrum

Controlled blasting techniques may be useful in stages of construction of some structures, tunnel, embedded foundations, etc. or rock removal, quarrying and preparation of finished slopes, because of the extreme complexity of each setting. While surface blasting produces ground motion and airwaves, underground blasting produces only ground motion waves, which cause ground vibration. The analyses of this study include underground blasts. Blasting-induced ground motions under controlled explosions are measurable excitations. However, these excitations occur at different frequency amplitude depending on soil types, blast distances and charge weights. The difficulty of determining the time histories of ground motions due to blast loads is obvious. In such a situation, utilizing the response spectrum method, which is generalized shock excitation, instead of time history analysis having various amplitudes can be convincing for engineers.

Underground shock ground motions are determined from an empirical formula. These equations are for TNT detonations at or near the ground surface. The charge weight and distance from the explosion are effective for the ground shock parameters. Eq. (1) demonstrates maximum horizontal acceleration (PPA) of the ground surface for rock media (Hao and Wu, 2005).

$$PPA = 3.379R^{-1.45}\,Q^{1.07} \quad \text{(g)} \tag{1}$$

where R is the distance (in meters) from the point of the explosion and Q is the TNT charge weight (in kilograms).

A computer program based on Fortran programming language was developed to simulate shock response spectra producing from the ground shock acceleration time histories. Ground shock accelerations are simulated by using a non-stationary random process method. To this process, time-dependent ground motion accelerations are produced by help of the parameters of a deterministic shape function of time (i.e. a time-intensity envelope function) $p(t)$ and stationary white noise $w(t)$ of intensity S_0 (Bolotin, 1960; Jennings et al., 1969; Ruiz and Penzien, 1969). To determine non-stationary blast ground motions, Amin and Ang (1698) generated a formulation as follows:

$$a_b(t) = p(t)\, w(t)_{sta} \tag{2}$$

A time-intensity envelope function and frequency characteristics are crucial parts of a non-stationary stochastic process, well-known an earthquake ground motion is given as an example. The time-dependent envelope function $p(t)$ obtained from the Hilbert transform (Hahn 1996) of blast ground motion may be represented as an exponential function given by Eq. (3) (Hao and Wu 2005).

$$p(t) = \begin{cases} 0, & t \le 0 \\ m\, t\, e^{-nt^2} & t > 0 \end{cases} \tag{3}$$

where m and n depend on the non-stationary ground motion and e is the base of the natural logarithm. The general envelope function of blast ground motion is depicted in Fig. 1.

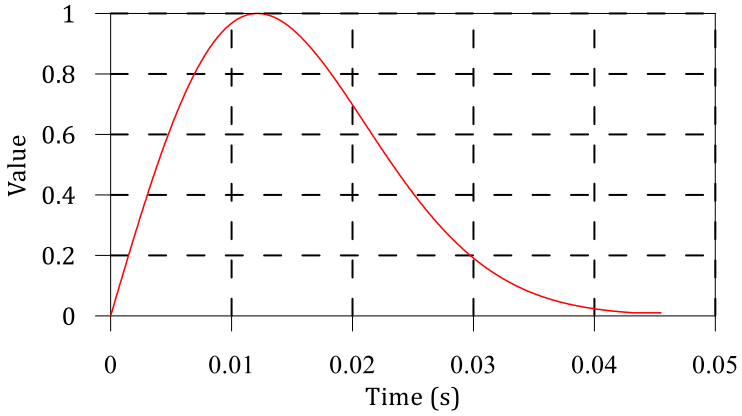

Fig. 1. Envelope function of shock ground motion.

PSD functions used to represent the blast ground motion which was thought of as a stationary random process $w(t)_{sta}$ have been proposed by Wu and Hao (2005). The power spectrum based on Tajimi (1960) and Kanai (1957) studies is adopted for blast ground motion as follows:

$$S(f) = \frac{1+4\xi_g^2 f^2/PF^2}{(1-f^2/PF^2)+4\xi_g^2 f^2/PF^2} \tag{4}$$

where PF is the principal frequency, ξ_g is the soil damping coefficient, S_0 is the intensity of the ideal white noise excitation at the bedrock-overburden interface. The principle frequency can be formulated as follows:

$$PF = 465.62\left({}^{R}\!/_{Q^{\frac{1}{3}}}\right)^{-0.13}$$

$$0.3 \le {}^{R}\!/_{Q^{1/3}} \le 10 \quad \text{(Hz)} \tag{5}$$

A constant value ξ is taken as 0.6. S_0 is calculated by

$$S_0 = 1.49 \times 10^{-4} R^{-2.18} Q^{2,89} \quad (\text{m}^2/\text{s}^3) \tag{6}$$

Power spectral density functions are constituted by the frequency range of 0.3–10 Hz (Wu et al., 2005; Wu and Hao, 2007; Singh and Roy, 2010). The waveforms of bedrock acceleration are derived from a second-order differential equation as given by Eqs. (7) and (8).

$$\ddot{x}(t) + 2\xi_g \omega_g \dot{x}(t) + \omega_g^2 x(t) = -a_b(t) \tag{7}$$

$$\ddot{x}(t) = -2\xi_g \omega_g \dot{x}(t) - \omega_g^2 x(t) \tag{8}$$

where $a_b(t)$ is a stationary Gaussian white noise process; ω_g is natural frequency; x is the first filtered response.

The shock response spectrum is calculated by considering a transient shock input signal which is generally provided as the time evolution of displacement, velocity or acceleration. A series of SDOF linear oscillators (like a mass-spring system) with increasing natural frequencies is used to build a shock response spectrum. The calculation uses an amplification factor Q=10 corresponding to a viscous damping ratio of 5% (Tuma et al., 2011).

Shock response spectrum with damping can be defined as:

$$S_l = \left|\omega \int_0^t \ddot{x}(\tau) e^{-\xi\omega(t-\tau)} sin\omega(t-\tau) d\tau\right|_{max} \tag{9}$$

where, $\ddot{x}$ is the base acceleration of an SDOF system as a function of time, and S_l is the spectral acceleration.

2000 kg, 1000 kg and 500 kg charge weights and 50 m, 100 m, and 200 m distances from the point of the

explosive are taken into account to analyze the demineralized water tank with a piled raft foundation subjected to shock ground motion. The shock response spectra depending on the time history ground motions for each case are depicted in Figs. 2 and 3. In this study, the displacement and stresses obtained here are maximum values using the CQC modal combination methods.

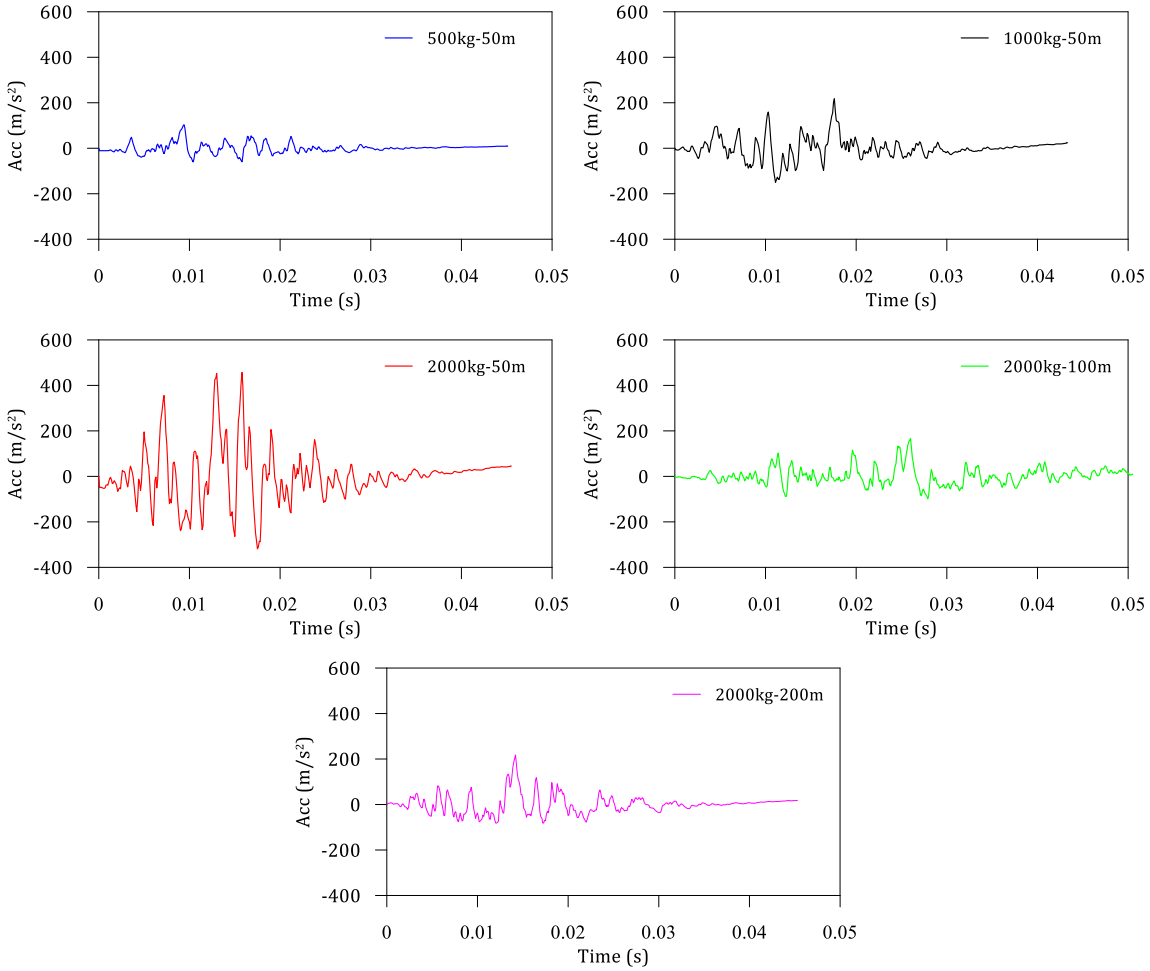

Fig. 2. Acceleration time histories for different blast distances and charge weights.

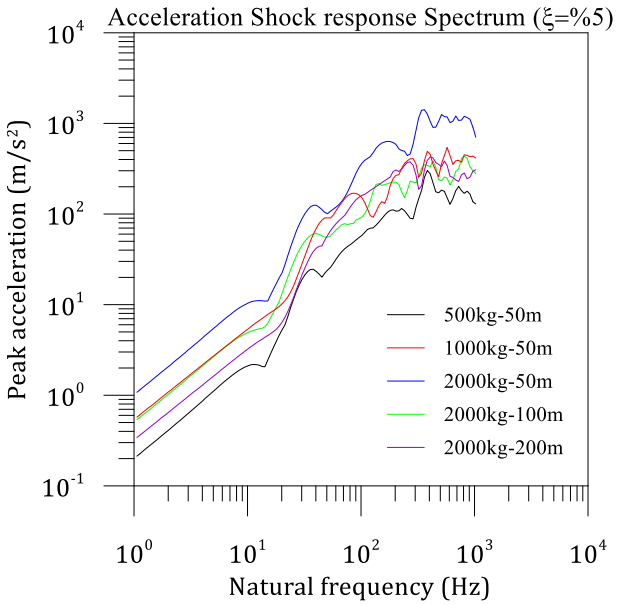

Fig. 3. Shock response spectrum due to for different blast distances and charge weights.

3. Application

3.1. Geometry and material properties

This study aims to investigate the dynamic behavior of the demineralized water tank with a piled raft foundation under blast-induced ground motion. The picture and a piled raft foundation system of the demineralized water tank are indicated in Fig. 4. Also, the geometry of the soil-pile-structure-fluid interaction system and the simplified geometry measures of the tank and soil layer are shown in Figs. 5 and 6, respectively. As indicated in Fig. 6, the inner diameter of the tank is 16.0 m, the height is 16 m. The maximum height of the water surface is 15.0 m. The tank wall is assumed as a constant thickness, which is 10 mm from the bottom to roof of the tank. The tank was made of the stainless-steel material. The elastic modulus, Poisson's ratio and density of the tank are 200 GPa, 0.3 and 7850 kg/m^3, respectively. The density and Bulk modulus of the water are assumed as 1000 kg/m^3 and 2.07 GPa, respectively. To achieve the required settlement performance of the tank and to reach the most economic foundation design, the calculations were carried out with an optimal number of piles. The cast in place 19 concrete piles calculated according to the soil parameters and loads caused by tanks are 800 mm in diameter and are 19 m long. All piles are the same diameter. The tank is constructed on a reinforced concrete foundation with 19.0 m outer diameter and 80 cm height. The material properties of the concrete are as follows, the elastic modulus is 30 GPa, Poisson's ratio is 0.18 and density is 2300 kg/m^3.

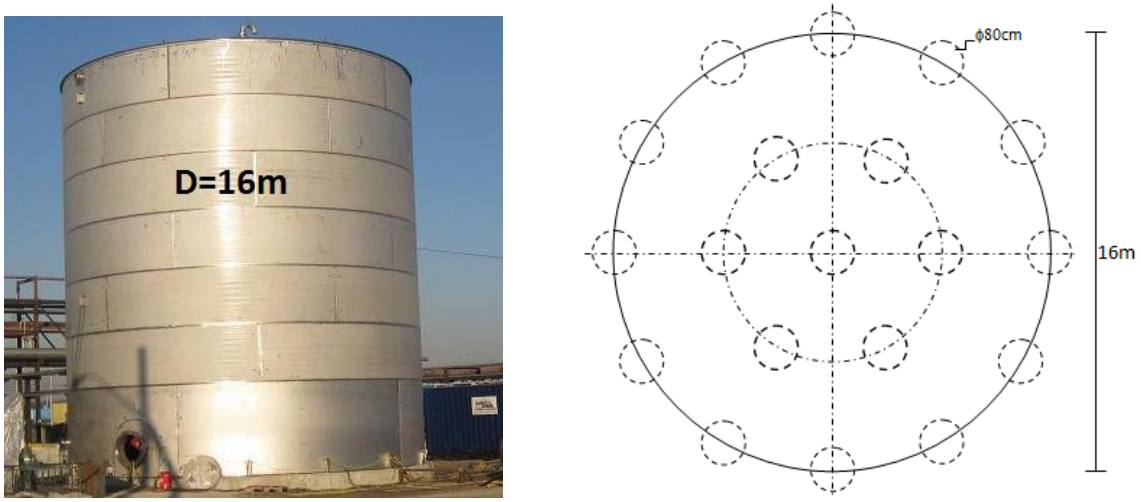

Fig. 4. Demineralized water tank with a piled raft foundation.

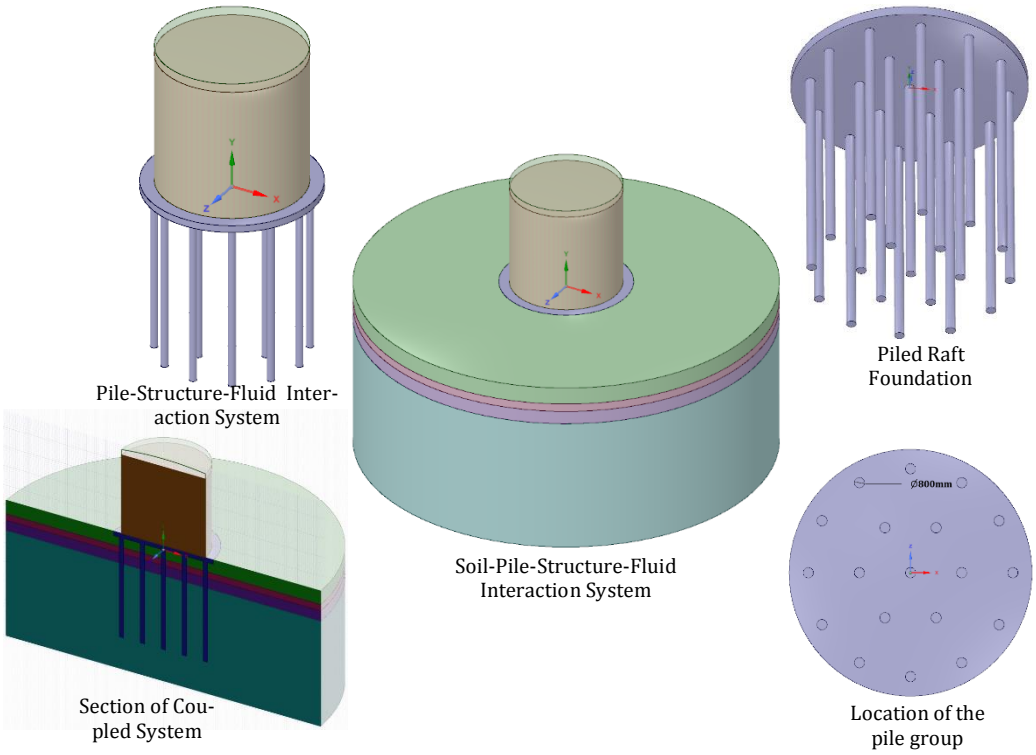

Fig. 5. The geometry of soil-pile-structure-fluid interaction system.

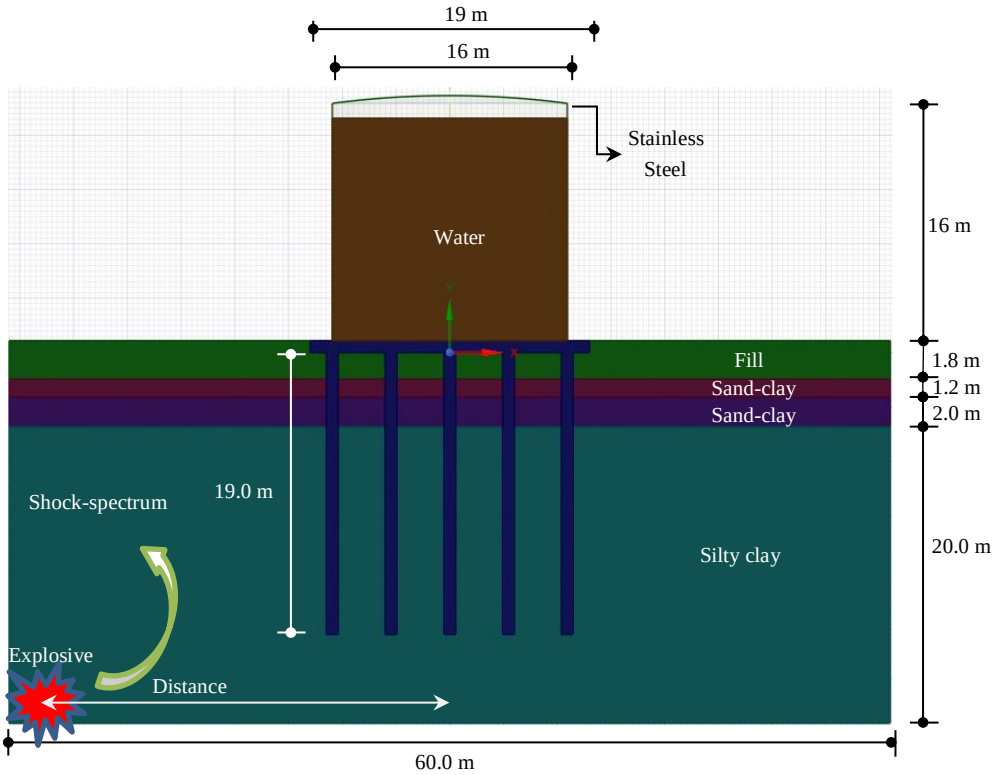

Fig. 6. Demineralized water tank with a piled raft foundation.

In the coupled system, the pile, soil and concrete foundation all use solid elements, simulate-ion of the incompressible fluid in the tank is represented with the fluid element. The tank and its vault use shell elements. The frictional contact element (CONTA174) are utilized to provide the interaction between the pile and soil. CONTA174, which is used for general rigid-flexible and flexible-flexible contact analysis, is an 8-node element. The elements can be appropriate to represent contact and sliding between 3D surfaces. In this system, the isotropic friction model was used with a variable coefficient ranging between 0.35 and 0.55 and a starting value of 0.45 that corresponds to the coupling materials. The friction coefficient values of the fill, sand-clay and silty-clay soil types are assumed as 0.40, 0.35 and 0.50, respectively. The frictionless contact elements are utilized between the water and the tank shell to allow for displacement of the free surface adjacent to the tank wall.

4. Results of Analyses

The shock spectrum analysis of a demineralized water tank with a piled raft foundation to shock-induced ground vibration is carried out using the finite element analysis package (ANSYS 2013). This study investigates the effect of the shock-induced ground motions on the dynamic response of the considered coupled system for the different charge weights and distances from the charge center by using the shock response spectrum method. In addition, the effects of the water fill level of the tank reservoir and the number of piles are studied as a parametric model.

4.1. The effect of charge weight

In order to the charge weight effects on the dynamic behavior of the demineralized water tank with a piled raft foundation system, the charge weight values of 500, 1000 and 2000 kg are taken into account. The distance from the charge center to the coupled system center is assumed as 50 m in all analyses in this section. The displacement and equivalent stress values of the tank are indicated in Figs. 8 and 9 for the charge weight values of 500, 1000 and 2000 kg, respectively.

Fig. 8(a) shows the displacement contour distribution on the tank consisting of a piled raft foundation. The displacement distributions for all of the charge weight values are close to each other, here, it was given only the displacement distribution for the charge weight value of 500kg. It can be seen that the displacement values increase with increasing the tank's height. Maximum displacements occur at the top of the tank. The displacement distributions along the tank's height with the various charge weights are shown in Fig. 8(b). Fig. 8(b) shows that the displacement values neatly increase with the tank's height. Also, it must be said that the charge weight values affect displacement values. Increasing the charge weight cause to increase the displacement values along with the tank's height.

Fig. 9(a) and Fig. 9(b) indicate the Equivalent stress contour distribution (for 500kg) and along with the tank's height, respectively. It can be seen from Fig. 9(a) that the stress distribution contours at the bottom of the tank are generally higher than those at the top of the tank. As expected, the higher stress concentrations rise

near the bottom of the tank. The stress contour distribution graphics for the charge weights of 1000 kg and 2000 kg are almost the same. When compared the stress distributions for the various charge weight values, the difference between the stress values is extremely high. Also, the stress distribution values near the top and bottom of the tank are highest. Clearly, it can be observed that the increase of the charge weight values causes to increase the stress values on all tank body and along with the tank.

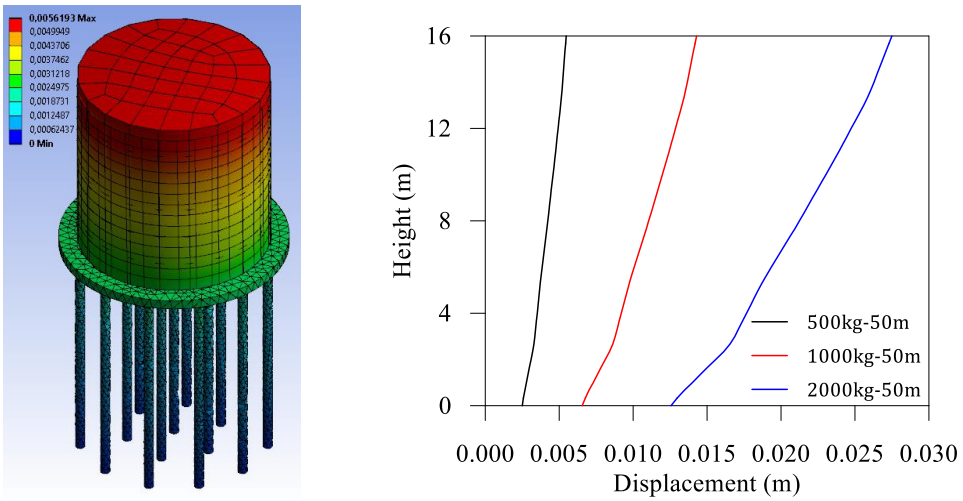

Fig. 8. The displacement: (a) contour distribution; (b) along with the tank's height for the charge weights of 500, 1000 and 2000 kg.

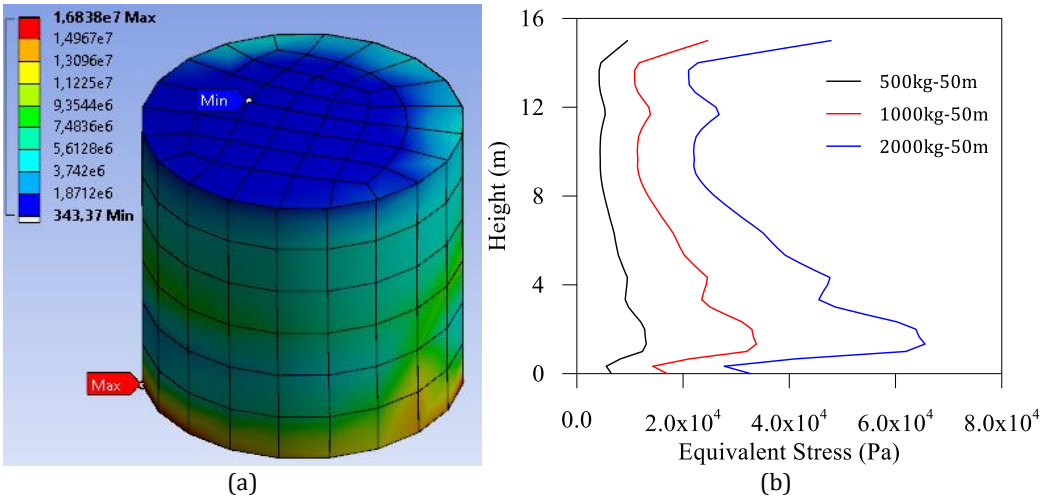

Fig. 9. The equivalent stress: (a) contour distribution; (b) along with the tank's height for the charge weights of 500, 1000 and 2000 kg.

4.2. The effect of charge center distance

The charge center distance effects on the dynamic behavior of a demineralized water tank with a piled raft foundation system are estimated by using the different charge center distances. In this part, the charge center distances of 50 m, 100 m and 200 m are utilized with the charge weight of 2000 kg. The displacement and equivalent stress of the tank are indicated in Figs. 10 and 11 for the charge center distance values of 50 m, 100 m and 200 m, respectively. Fig. 10(a) and Fig. 11(a) only show the displacement and equivalent stress distributions for the charge center distance of 50 m, because of the fact that the result contours for the other distance values have almost the same distributions.

In Fig. 10(a), the displacement values along the tank's height (Section 1-2) are the highest at the top of the tank while the lowest values at the bottom of the tank, also seen in Fig. 10(b). As observed in Fig. 11(a), the highest stress concentrations generally occur at the boom of the tank (junction point of the bottom of the tank and piled-raft foundation). It is also seen from Fig. 11(b), the stress values at the top and near the bottom of the tank are the highest values when compared to those of other height levels of the tank. The thing that needs to be mentioned from Fig. 10(b) and Fig. 11(b) is that both the displacement and equivalent stress values increase with decreasing the charge center distances.

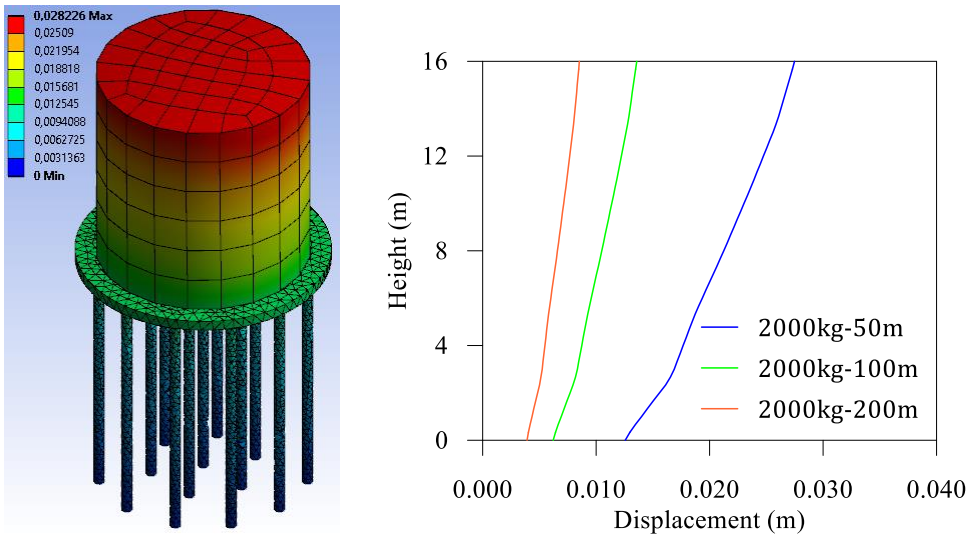

Fig. 10. The displacement: (a) contour distribution; (b) along with the tank's height for the charge weights of 50, 100 and 200 m.

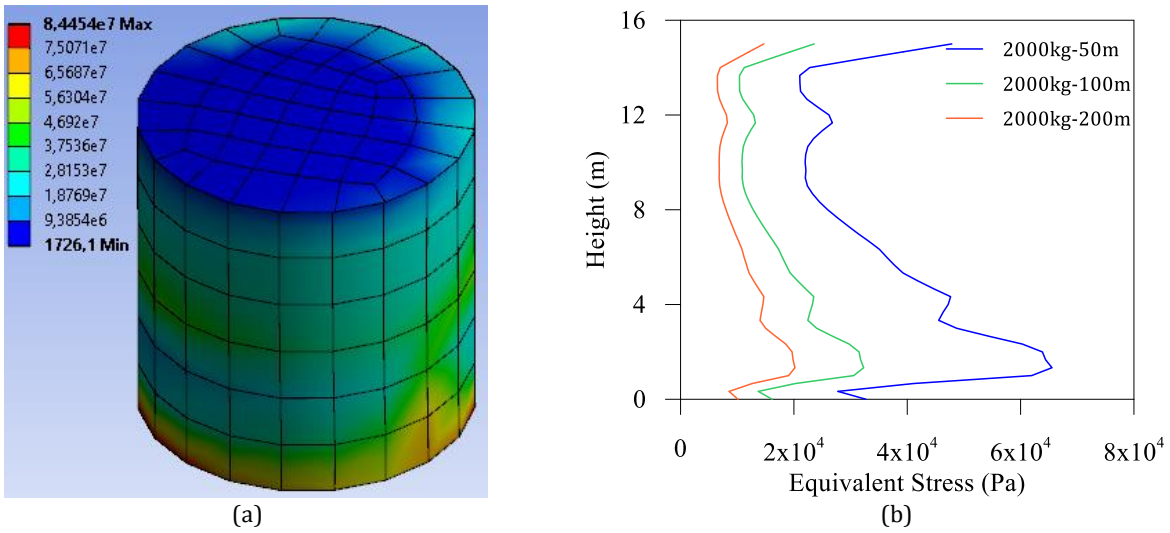

Fig. 11. The equivalent stress: (a) contour distribution; (b) along with the tank's height for the charge weights of 50, 100 and 200 m.

4.3. The effect of water fill level

In this section, the effects of water fill level on the dynamic behavior of the demineralized water tank with a piled raft foundation system are investigated. For this purpose, the water fill level height is assumed as 15 m from the bottom of the tank. As an external load, the blast charge weight and the charge center distance are taken as 2000 kg and 50 m, respectively. The water fill level cases in the tank are considered as 15 m (3/3 full), 10m (2/3 water fill level) and 5 m (1/3 water fill level). According to these cases, the displacement and equivalent stress distributions are presented in Figs. 12 and 13.

The displacement contour distribution and the displacements on Section 1-2 in the case of full water level, 2/3 water fill level and 1/3 water fill level in the tank with a piled raft foundation system subjected to blast ground motion are presented in Figs. 12 and 13. It can be seen from the figures that the displacement values increase with the tank's height. Maximum displacement values occur at the top of the tank. Also, it can clearly be observed that the displacement values increase with increasing the water fill level in the tank.

The equivalent stress contour distribution and the equivalent stress values on Section 1-2 in the case of full, 2/3 and 1/3 full of water in the tank are shown in Figs. 14 and 15. Fig. 14 shows that the Equivalent stress contour concentrations occur at the water fill levels and lower levels in the tank. While the stress concentrations in the case of 1/3 water fill level seem about 5 m tank's height from the bottom, those in the case of 2/3 water fill level occur at about 10 m tank's height. As can be seen in Fig. 15, the extreme jumps occur in the equivalent stresses at the level of 1/3 and 2/3 full of water. The stress values in the case of full of water can be ignored when compared to those of 1/3 and 2/3 full of water.

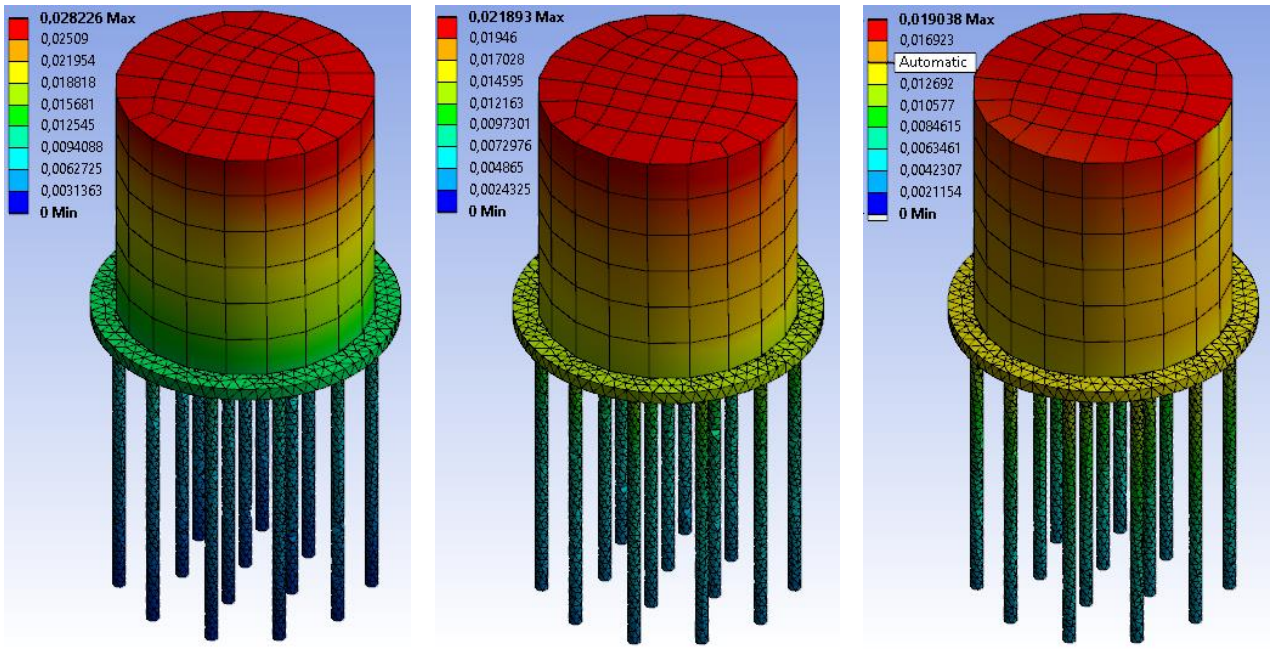

(a) (b) (c)

Fig. 12. The displacement contour distributions for (a) full, (b) 2/3 and (c) 1/3 of the water fill level in the tank.

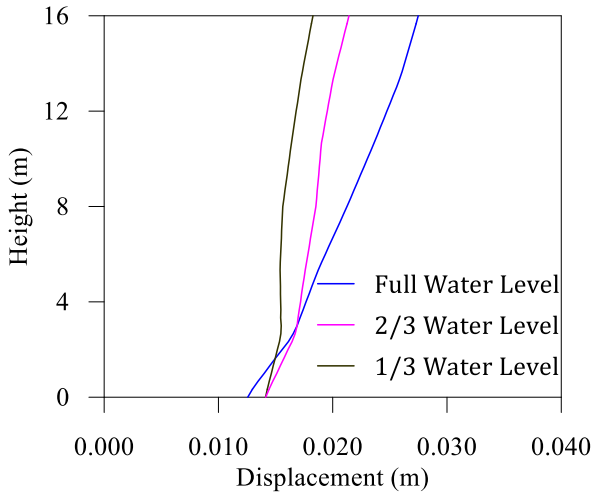

Fig. 13. The displacement values along with the tank's height for full, 2/3 and 1/3 of the water fill level in the tank.

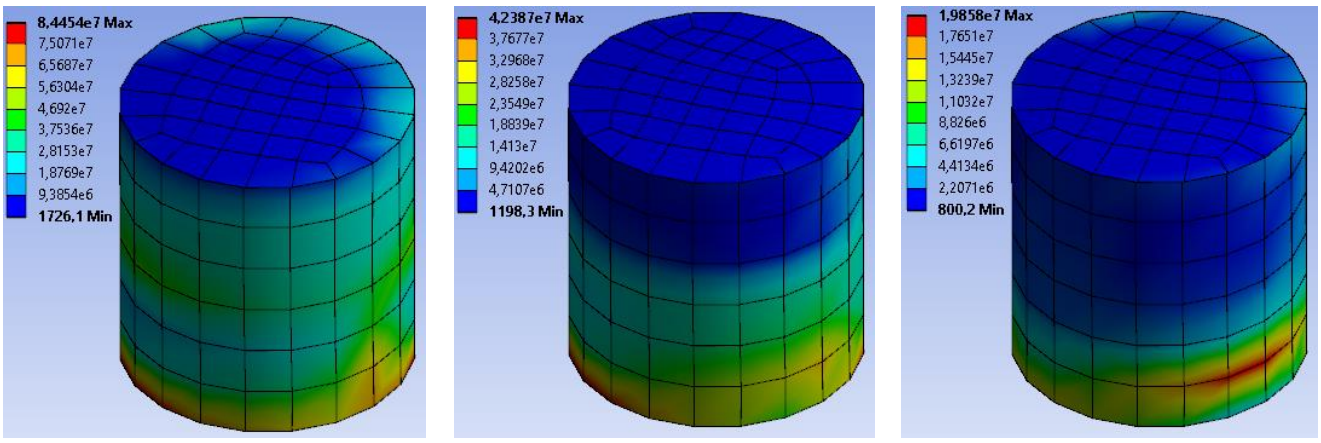

(a) (b) (c)

Fig. 14. The equivalent contour stress distributions for (a) full, (b) 2/3 and (c) 1/3 of the water fill level in the tank.

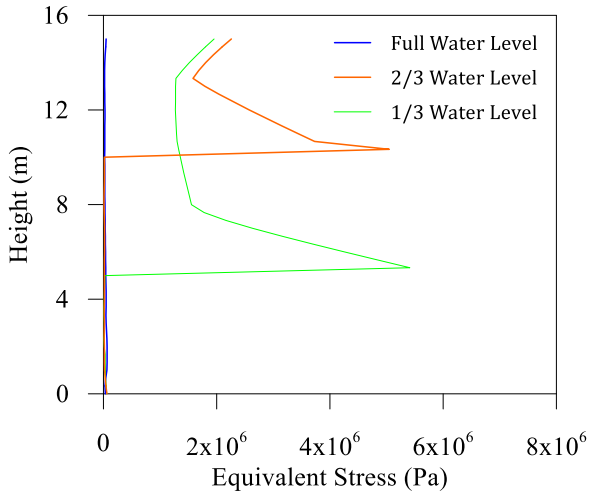

Fig. 15. The equivalent stress values along with the tank's height for full, 2/3 and 1/3 of the water fill level in the tank.

4.4. The effect of the number of piles

This study also investigates the effect of the number of piles to estimate the dynamic behavior of the demineralized water tank with a piled raft foundation system. To this aim, it is first assumed that the tank is designed with a piled raft foundation consisting of 19 piles (model 1) on a soil whose properties are obtained experimentally. The number of piles is then assumed as 12 piles (model 2) and no-pile (model 3). The displacement and equivalent stress distributions are indicated in Figs. 16-19. In this section, the blast charge weight and the charge center distance are taken as 2000 kg and 50 m, respectively. The tank's water level is assumed as 15 m.

Fig. 16 compares the displacement contour distributions on the tank in the case of 19 piles, 12 piles and no-pile. The displacement values along the tank's height are also presented in Fig. 17. As shown in these figures, the displacement values in the case of 12 piles are smaller than those of 12 piles. The displacements in the case of no-pile have maximum values when comparing the other cases. It is also seen in Fig. 17 that the displacement values on Section 1-2 increase with increasing the height of the tank. Figs. 18-19 show the equivalent stress contour distribution and the equivalent stress values on Section 1-2 in the case of 19 piles, 12 piles and no-pile. It is seen from the figures that the equivalent stress concentrations occur at the bottom of the tank for all cases. The stress distribution values near the bottom of tank have quite different. While the stress values in the case of no-pile are higher than those in the case of 12 piles. Minimum stress values in the same region of the tank take place in the case of 19 piles.

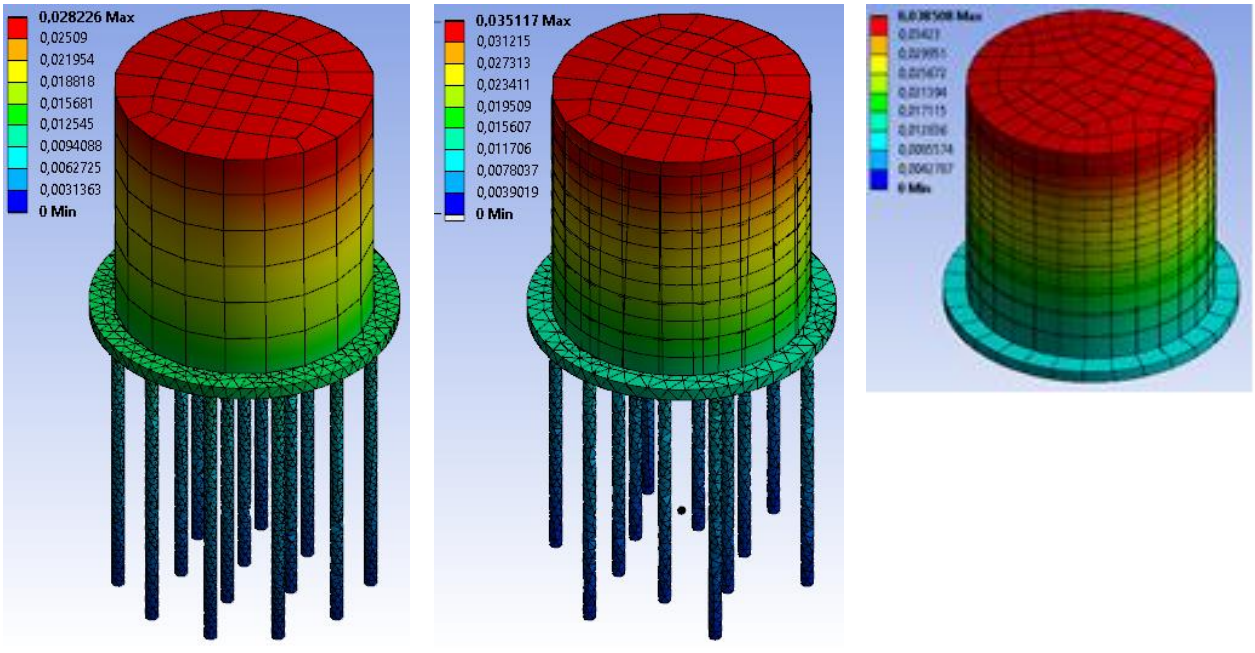

(a) (b) (c)

Fig. 16. The displacement contour distributions for (a) 19 piles, (b) 12 piles and (c) no-pile.

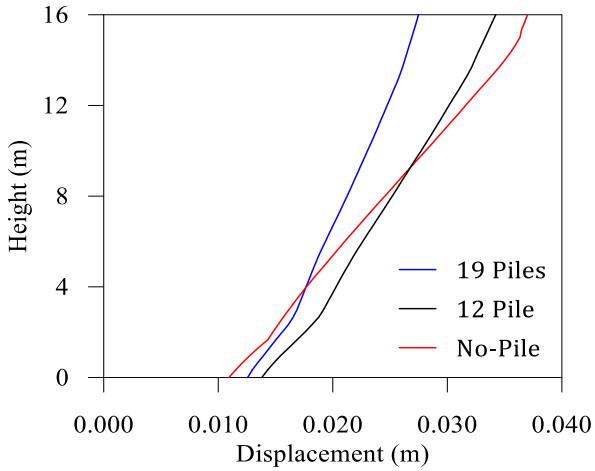

Fig. 17. The displacement values along with tank's height for19 piles, 12 piles and no-pile.

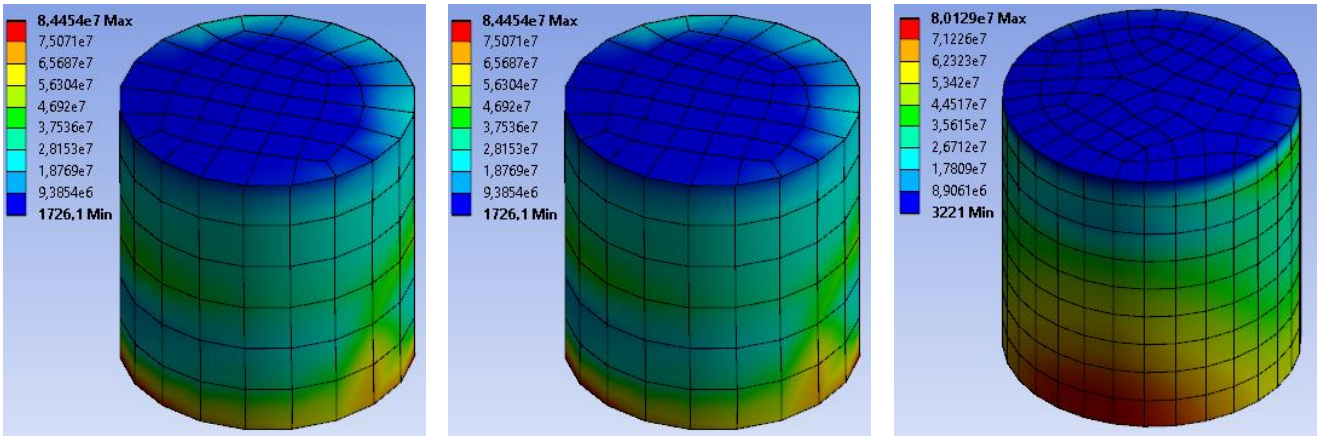

(a) (b) (c)

Fig. 18. The equivalent contour stress distributions for (a) 19 piles, (b) 12 piles and (c) no-pile.

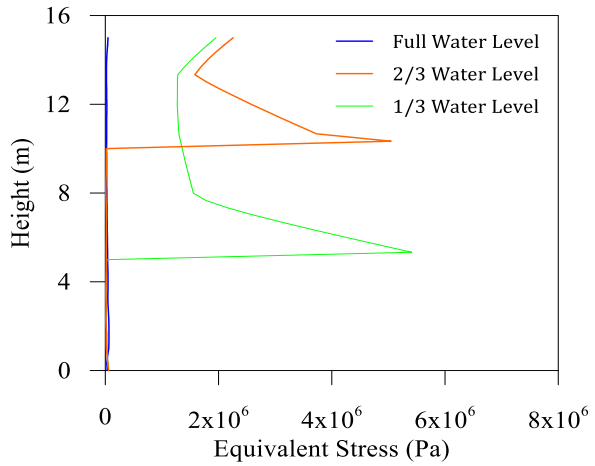

Fig. 19. The equivalent stress values along with tank's height for19 piles, 12 piles and no-pile.

5. Conclusions

The current study mainly focuses on the effect of blast-induced ground motion on the dynamic behavior of a demineralized water tank with a piled raft foundation considering soil-pile-structure-fluid interaction. ANSYS software uses to establish the 3-D finite element model of the soil-pile-structure-fluid interaction system. The shock response spectrum method determined from the blast ground motions are used to estimate the dynamic behavior of the soil-pile-structure-fluid interaction system.

Through the results determined the shock response spectrum analyses, there were observed that the charge

weight, charge center distance, tank's water level and the number of piles have extreme effects on the dynamic behavior of the demineralized water tank- fluid-soil-pile-interaction coupled system. While the displacement and stress values on the tank increase with the increase of the charge weight of the blast and water fill level, decrease due to the increase of the charge center distances and number of piles.

In general terms, it is observed that especially the maximum equivalent stress contour distributions are located at the middle and bottom part of the tank. Of course, the peak displacement values are expected to be at top of the tank. In addition, as a result of the analysis, it was observed that the water level change in the tank played an important role in the sudden stress change of the tank. It turns out that the displacement values also change visibly. The number and distribution of piles caused quite remarkable changes in the dynamic behavior of the water tank. Especially in the region where the water tank meets the basic part, there are significant differences in the stresses that occur.

As a result, although it is rarely encountered, besides the earthquake effect, perhaps blast ground motion should be taken into consideration in the design of such structures. Especially today, when the need for water has reached important dimensions, it is important to design such tanks in a reliable way.

References

Amin M, Ang AHS (1698). A non-stationary stochastic model of earthquake motion. *Journal of Engineering Mechanics* Division, ASCE, 94, 559–583.

ANSYS (2013). Workbench 2013. User's manual, Ansys Incorporation, Ansys, Inc., Canonsburg, PA.

Blair DP, Miller DK, Armstrong LW (2007). The response of water storage tanks under blasting. *EXPLO Conference 2007*, Australasian Institute of Mining and Metallurgy, Wollongong, New South Wales, 204.

Bolotin VV (1960). Statistical theory of the aseismic design of structures. *Proceedings of the 2nd World Conference on Earthquake Engineering*, Tokyo, 1365–1374.

Cheng X, Jing W (2017). Calculation models and stability of composite foundation treated with compaction piles. *Geomechanics and Engineering,* 13, 929–946.

Dieterman HA (1993). Liquid-structure-foundation interaction of slender water towers. *Archive of Applied Mechanics*, 63, 176–188.

Fiore A, Demartino C, Greco R, Rago C, Sulpizio C, Vanzi I (2018). Seismic performance of spherical liquid storage tanks: a case study. I*nternational Journal of Advanced Structural Engineering*, 10, 121–130.

Ha JG, Park HJ, Lee MK, Lee H, Kim D-S (2017). Seismic behavior of LNG storage tank considering soil-foundation-structure interaction with different foundation types. *ICSMGE 2017 - 19th International Conference on Soil Mechanics and Geotechnical Engineering,* 931–934.

Haciefendioğlu K, Soyluk K, Birinci F (2012). Numerical investigation of stochastic response of an elevated water tank to random underground blast loading. *Stochastic Environmental Research and Risk Assessment*, 26, 599–607.

Hahn SL (1996). Hilbert Transforms in Signal Processing. Artech House, Norwood, Maryland

Hao H, Wu C (2005). Numerical study of characteristics of underground blast induced surface ground motion and their effect on above-ground structures. Part II. Effects on structural responses. *Soil Dynamics and Earthquake Engineering,* 25, 39–53.

Higuchi S, Mori T, Matsuda T, Goto Y, Kutter BL, Akiyama H, Toki K, Kobayashi M (2000). Seismic performance of Lng storage tank foundations during the very large earthquake. *12th World Conference on Earthquake Engineering (12WCEE2000)*, 1–8.

Jennings PC, Housner GW, Tsai NC (1969). Simulated earthquake motions for design purposes. In: *Proceedings of the 4th World Conferences on Earthquake Engineering*, 1, 145–160.

Kanai K (1957). Semi-empirical formula for the seismic characteristics of the ground. *Bulletin of the Earthquake Research Institute*, University of Tokyo, 35, 309–324.

Kim YK, Song HS (2017). A study on the cathodic protection design optimization of steel piles for LNG storage tanks by numerical analysis. *Corrison Science and Technology,* 16, 294–297.

Park H-J, Ha J-G, Kwon S-Y, Lee M-G, Kim D-S (2017). Investigation of the dynamic behaviour of a storage tank with different foundation types focusing on the soil-foundation-structure interactions using centrifuge model tests. *Earthquake Engineering & Structural Dynamics,* 46, 2301–2316.

Purnama AY, Rifa A, Hardiyatmo HC (2018). Fuel tank foundation improvement system on soft soil layer based on 3D numerical simulation. *International Journal of Geomate*, 14, 13–19.

Roberts DV (1961). Foundations for cylindrical storage tanks. *Proceedings of the 5th International Conference on Soil Mechanics and Foundation Engineering*, Paris, France, 785–788.

Ruifu Z, Dagen W, Xiaosong R (2011). Seismic analysis of a LNG storage tank isolated by a multiple friction pendulum system. *Earthquake Engineering and Engineering Vibration,* 10, 253–262.

Ruiz P, Penzien J (1969). PSEQN: Artificial generation of earthquake accelerograms. *National Technical Information Service*, University of California, Berkeley.

Sahraeian SMS, Takemura J, Seki S (2018). An investigation about seismic behavior of piled raft foundation for oil storage tanks using centrifuge modelling. *Soil Dynamics and Earthquake Engineering*, 104, 210–227.

Singh PK, Roy MP (2010). Damage to surface structures due to blast vibration. *International Journal of Rock Mechanics and Mining Sciences*, 47, 949–961.

Tajimi H (1960). A statistical method for determining the maximum response of a building structure during an earthquake. *Proceedings of the 2nd World Conference on Earthquake Engineering*, Tokyo and Kyoto, Japan, 781–797.

Tuma J, Babiuch M, Koci P (2011). Calculation of a shock response spectra. *Acta Montanistica Slovaca*, 16, 66–73.

Wu C, Hao H (2005). Numerical study of characteristics of underground blast induced surface ground motion and their effect on above-ground structures. Part I. Ground motion characteristics. *Soil Dynamics and Earthquake Engineering,* 25, 27–38.

Wu C, Hao H (2007). Numerical simulation of structural response and damage to simultaneous ground shock and airblast loads. *International Journal of Impact Engineering,* 34, 556–572.

Wu C, Hao H, Lu Y (2005). Dynamic response and damage analysis of masonry structures and masonry infilled RC frames to blast ground motion. *Engineering Structures,* 27, 323–333.

Ximei Z, Haosong W, Feng FAN (2014). Multi-physics coupling method and applications of fluid-structure interaction on LNG storage tanks. *11th World Congress on Computational Mechanics (WCCM XI), 5th European Conference on Computational Mechanics (ECCM V), 6th European Conference on Computational Fluid Dynamics (ECFD VI),* 1–11.

Xinliang J, Xuecheng D (1992). Vibration analysis of liquid-storage tank-pile-soil under seismic excitation. *Proceedings of the World Conference on Earthquake Engineering,* 1797–1800.

Yamashita K, Hashiba T, Ito H, Tanikawa T (2014). Performance of piled raft foundation subjected to strong seismic motion. *Geotechnical Engineering Journal of the Seags & Agssa*, 45, 33–39.

Zhang R, Zhang Z, Wang H (2018). Influence of soil-pile-structure-fluid interaction on seismic behavior of a liquid storage tank. *Proceedings of GeoShanghai 2018 International Conference: Advances in Soil Dynamics and Foundation Engineering: Advances in Soil Dynamics and Foundation Engineering,* Springer Singapore, 70–77.

Challenge Journal of Structural Mechanics

Research Article

Numerical investigation on damage performance of a reinforced concrete structure subjected to machine loads

Memduh Karalar [a,*], Murat Çavuşli [a]

[a] *Department of Civil Engineering, Zonguldak Bülent Ecevit University, İncivez, 67100 Zonguldak, Turkey*

ABSTRACT

Investigation of carrying capacity performance of reinforced concrete (RC) structures is very important for structural engineering. In this study, it is aimed to examine the nonlinear carrying capacity performance of an RC laboratory structure by using three dimensional (3D) modelling approach. For this purpose, Zonguldak Bulent Ecevit University Laboratory Structure is selected and it is modeled as three dimensional by utilizing IDECAD static software. After modelling all beams, columns and floors according to 2018 Turkish earthquake code, concrete classes are determined for all bearing elements and specified concrete classes are defined for all elements of 3D model. Then, structure is analyzed for empty situation (Case 1) and structural performance of building is analyzed to this situation. In the past, a flat of this RC structure has been exposed to strong machine loads. For this reason, a machine which is fixed on the floor is placed in the 3D model and RC structure is analyzed considering nonstructural machine element loads (Case 2). According to analysis results, Case 1 is compared with Case 2 and it is clearly seen that nonstructural machine loads effect nonlinear carrying capacity performance of RC buildings.

ARTICLE INFO

Article history:
Received 19 February 2020
Revised 16 March 2020
Accepted 15 April 2020

Keywords:
Carrying capacity
Damage performance
Three dimensional modelling
Reinforced concrete building

1. Introduction

In the recent years, reinforced concrete (RC) buildings have been frequently used in many world countries for many purposes. Concrete has tremendous compressive strength. Moreover, steel has tremendous tension strength. In the past, a very important idea was suggested about combination of concrete and steel materials. RC buildings have been revealed with this idea that combined concrete and steel. Any defect in concrete or steel element affects all of the structures. The adherence between these materials improves properties of RC elements. The first defect was related with damages in RC buildings that have the weak concrete materials. The importance of studies, researches and prevention about carrying capacity of the RC structures have risen after destructive earthquakes in the world especially in recent years. Demartino et al. (2017) examined an experimental and numerical study about the damage behavior of circular RC columns subjected to impact loading. Numerical study was performed using LS-DYNA software and these numerical results showed a good agreement with the experimental results. Wei et al. (2019) performed an experimental and numerical study about damage performance of reinforced conventional (RC) concrete and ultra-high performance concrete (UHPC) columns subjected important loads. In that study, there are total two different test specimens and these specimens have square and circular cross-section shapes. Moreover, each specimen group includes both RC and UHPC columns. After examined experimental results, numerical simulations were performed to observe residual loading capacity of UHPC column subjected to lateral impacts. Chen et al. (2019) evaluated damage performances of reinforced concrete (RC) columns. In that study, new compression-shear failure mode for RC columns was reported and discussed in detail. A finite element (FE) model was developed by using LS-DYNA. An important equation was proposed to rapidly evaluate the damage situation of the RC columns. Zhao et al.

* *Corresponding author*. Tel.: +90-372-291-2582 ; Fax: +90-372-257-4023 ; E-mail address: memduhkaralar@beun.edu.tr (M. Karalar)
ISSN: 2149-8024 / DOI: https://doi.org/10.20528/cjsmec.2020.03.004

(2020) investigated an experimental and numerical study about steel-concrete (SC) slabs subjected to blast loads. In that study, three small-scale reinforced concrete (RC), single-side- steel-concrete (SSSC) and center steel-concrete (CSC) slabs were tested to acquire the failure modes, mid-span deflection, and dynamic response. 3D numerical models were verified by the experimental tests. According to results, the damaged areas of concrete in SSSC and CSC slabs are larger than RC slab. Biswas et al. (2020) investigated numerical and experimental effects of non-uniform rebar corrosion on damage performance of reinforced concrete (RC) buildings. Damage behavior of RC beams subjected to non-uniform rebar corrosion was examined using three-dimensional (3D) nonlinear finite element (FE) analysis and experimental study. Seven RC beams were tested by using static loads. According to experimental and numerical study results, non-uniform corrosion in the steel bars cause to an important decrease in the load carrying capacity of RC beams. Kumar et al. (2020) performed experimental and numerical study about damage performance of reinforced concrete (RC) slabs subjected to blast loads. The finite element (FE) modelling was performed by using ABAQUS software. According to numerical results, the pressure of blast increase with an increase in the amount of TNT. Mohammed et al. (2020) examine damage performance of reinforced concrete (RC) structures subject to flexural loads. According to results, the damage behaviour of RC systems can be determined with the tensile cracking of the grout and failing of teeth at the joint. Moreover, there are many studies in the literature about damage performance of RC buildings (e.g. Xinchen and Bing (2020), Xian-Liang et al. (2019), Yang et al. (2019), Junsheng et al. (2020), Shuijing et al. (2019), Sulaem and Sudip (2019), Rajib et al. (2020), Li et al. (2020), Tie-shuan et al. (2019), Chen et al. (2019)).

As seen these studies, many investigators have contributed to the literature about nonlinear behaviour of RC buildings. However, effects of machine loads on damage capacity of RC structures have not been examined in the literature. In this study, Zonguldak Bulent Ecevit University laboratory structure is selected for numerical analyses. This structure has a damaged floor at third flat and this floor carries very strong machine loads for a long time. Therefore, examination of this floor is very important for structural engineering. After 3D model of the structure is created according to 2018 Turkish earthquake code, machine loads are applied to this damaged floor and all numerical results are compared with each other.

2. Methodology

In this study, a four story University building frequently exposes very stronger machine loads is examined by using 3D modelling. Because of this RC building carries very serious loads on the floors, examination of damage capacity performance of this structure is very important for the people and structures. First of all, the relievo of the RC building was obtained in detail. Each carrying element is determined in detail and the length information of each carrying element is entered in detail in the AUTOCAD program. Then, information was obtained about the current status of the fittings in the carrying elements using an x-ray device. The 3D model of the building was created with the help of the IDECAD static program. All carrying elements have been carefully entered into the program and the floors have been created in accordance with the project. Finally, core samples were taken from the structure. Considering the historical feature of the building, care was taken not to damage the building too much. Core samples were experimentally tested and their mechanical properties were determined. Total 30 different samples are used to obtained concrete classes of samples. While performing these tests, Turkish TS500 standard was considered and according to test results, average concrete class of these samples is obtained as C20. The material parameters of all carryings are carefully defined in the program. The analyses were first made for the empty status of the building considering 2018 Turkish earthquake code. Then, 30-ton machine load was applied to damaged floor of the structure and 3D model was analyzed taking into account this situation of the structure. According to analysis results, both situations of the structure are compared in detail.

3. Description and 3D Modelling of the RC Building

Zonguldak Bulent Ecevit University Laboratory was constructed in Zonguldak province in 2009. It is located in the University campus. It is a reinforced concrete (RC) building and it has 4 different flats. First and second flats have very heavy machines which are located on the floors and these machines are very critical for civil engineering technology. All flats have coffered slabs and these coffered slabs have very different thicknesses and mechanical properties from each other. These thicknesses are 12 cm, 14 cm, 15 cm, and 18 cm, respectively. Moreover, concrete classes of these slabs are C18, C20 and C22, respectively. Zonguldak Bulent Ecevit University Laboratory building is shown in Fig. 1. Moreover, views of the laboratory building projects are presented for the first floor, second floor, third floor and fourth floor in Fig. 2.

Building has 48 various columns and 88 different beams. Moreover, there are 37 various shear walls in this structure. Height of the first floor is 5 m and height of second, third and fourth floors are 5.2 m, 5.8 m and 4.2 m, respectively. First flat is used for building materials laboratory. Second flat is used for construction technology laboratory and other flats are constructed for office. While creating this structure, one floor of this building collapsed and this floor was rebuilt. This floor is at the third flat of this structure. Then, heavy machines had to be placed on this floor. This structure has been modelled by using 3D modelling approach. While performing modelling, IDECAD static software is used. Firstly, foundation of structure is created according to original project. After columns and beams are modelled, coffered slabs are created in 3D model as seen in Fig. 3. Then, structure is analyzed for empty situation of the building. After that, machine loads are calculated and these loads are applied

to collapsed floor (Fig. 4) and building is analyzed according to this situation. Moreover, fix boundary conditions are defined under the foundation of the building. According to analysis results, both situations of the structure are compared in detail.

4. Three Dimensional Analysis Results

Examination of 3D damage performance of reinforced concrete (RC) buildings is very important for civil engineers. Firstly, x-ray devices were used to determine current situation of the rebars (Fig. 5). Then, the compressive strength of the carrying elements was determined with the Schmidt hammer device. With this device, 15 strokes were applied to each carrying element and concrete classes of these elements are obtained by this device. According to numerical analysis results, empty and full situations of collapsed floor are examined and compared with each other (Tables 1-8). In Tables 1-4, performance analysis results are shown for empty situation of the floor in detail. Moreover, 3D performance results are presented for full situation which there are machine loads on the floor in Tables 5-8. In the numerical results, empty situation of the floor is named as Case 1 and other situation is named as Case 2.

Fig. 1. View of the Laboratory Building.

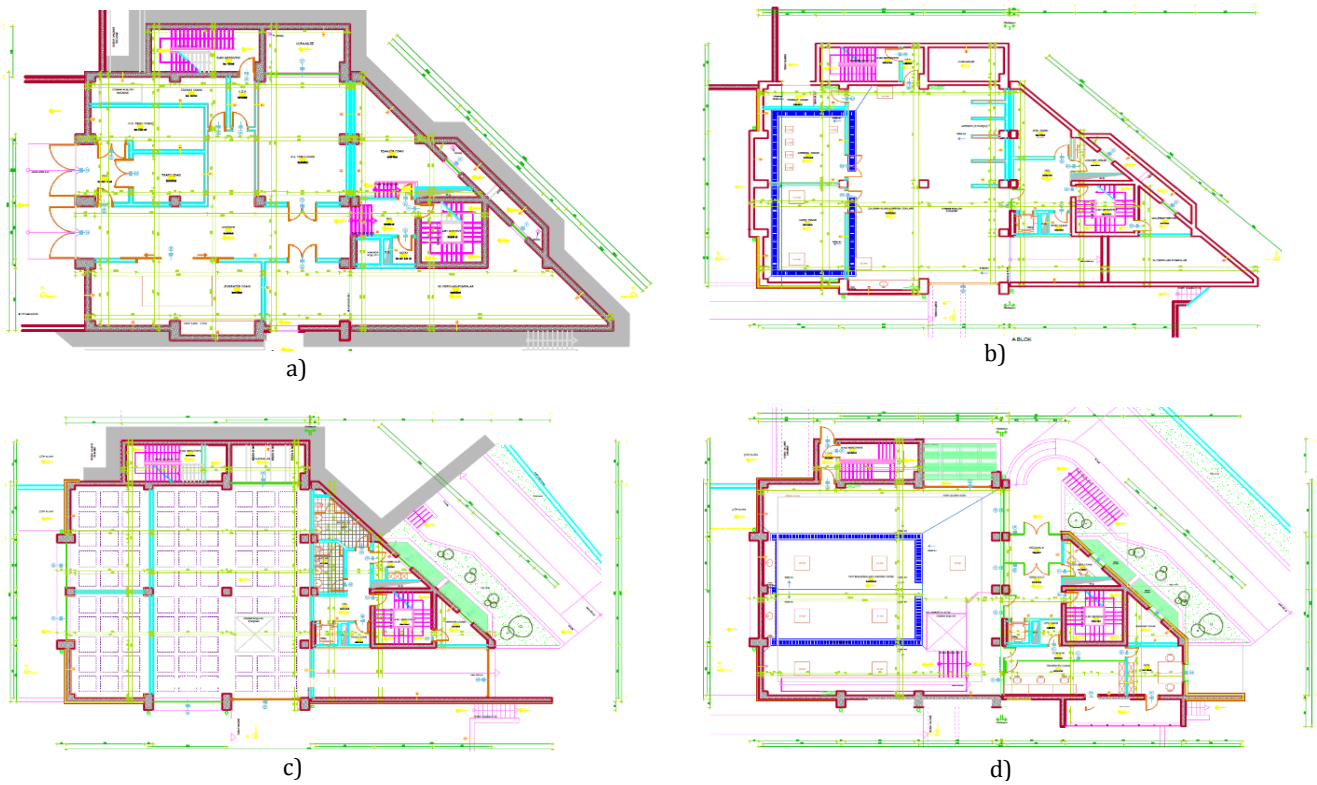

Fig. 1. View of the Laboratory Building projects: a) First floor; b) Second floor; c) Third floor; d) Fourth floor.

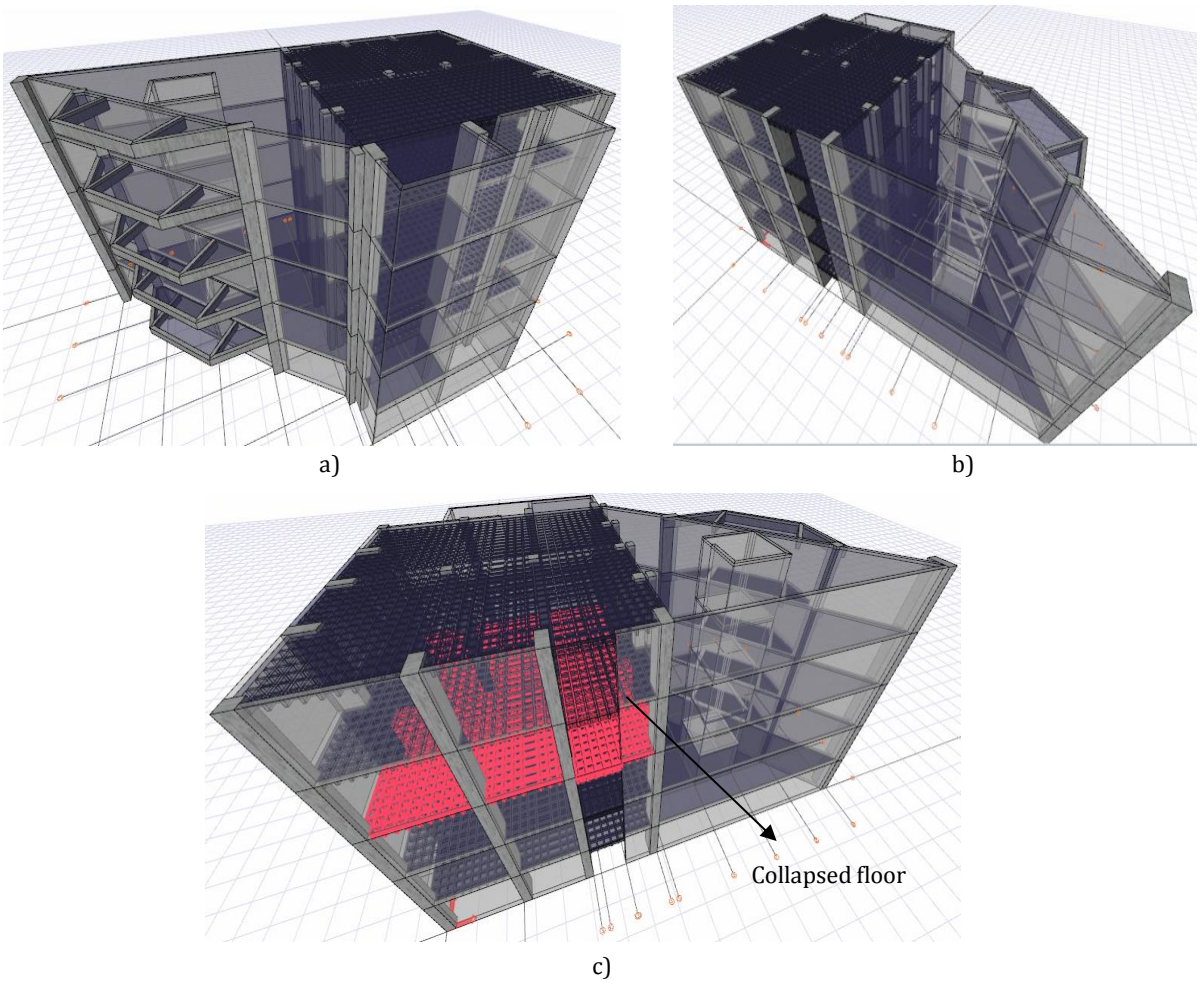

Fig. 3. 3D model of Laboratory Building.

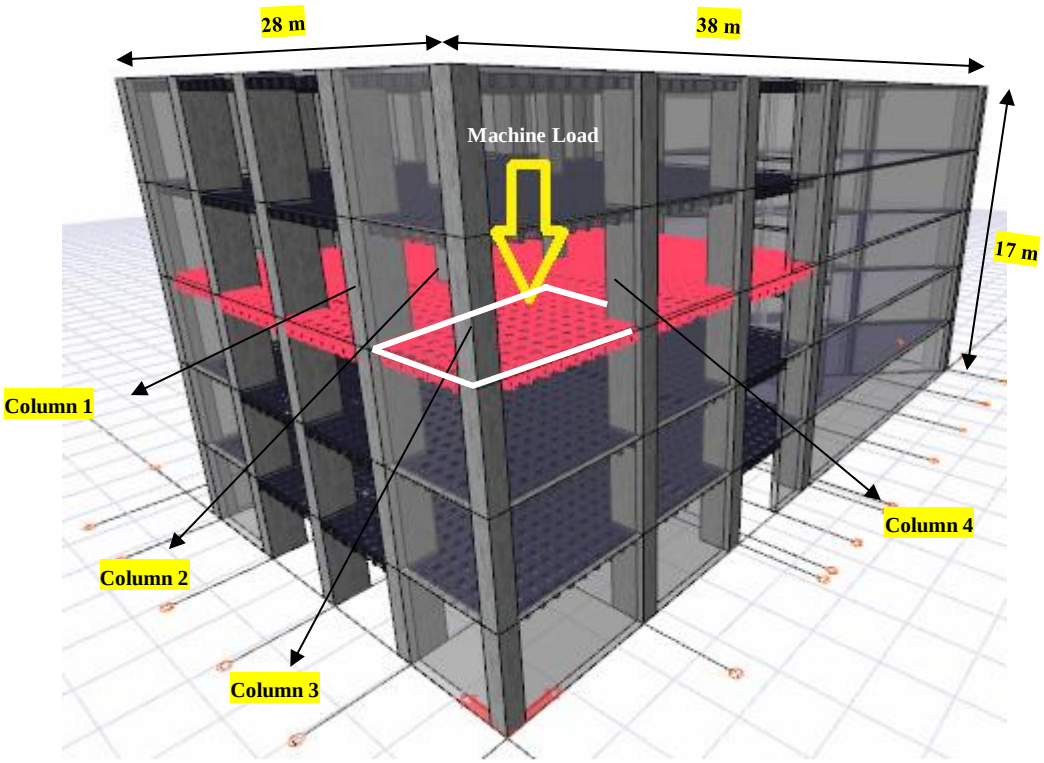

Fig. 4. Machine load on collapsed floor.

Fig. 5. Examination of carrying elements with X-ray device.

In Table 1, numerical results of column 1 (Ni, V2i, V3i, M2i, M3i, Nj, V2j, V3j, M2j, M3j) are shown for Case 1 in detail. Maximum loads are marked in bold. In addition, these loads are presented for 8 different combinations of 2019 Turkish Earthquake Code. According to Table 1, maximum normal load (Ni) is -11.90 kN for G+Q+EY2 combination and maximum shear load (Vi) is 5.24 kN for G+Q+EX2 combination. In addition, maximum moment load (Mi) is 5.71 kNm for G+Q+EY1 combination (Table 1). Maximum normal load (Nj) for j direction of column 1 is 12.42 kN for G+Q-EY1 combination and maximum shear load (Vj) is 4.69 kN. Besides, maximum moment load (Mj) is 7.81 kNm as seen from Table 1.

In Table 2, three dimensional numerical results (Ni, V2i, V3i, M2i, M3i, Nj, V2j, V3j, M2j, M3j) for column 2 are presented for Case 1. -27.82 kN maximum normal load (Ni) is obtained for G+Q+EY1 combination. Moreover, -4.21 kN maximum shear load (Vi) is obtained for G+Q+EY1 combination and maximum moment load (Mi) is 13.72 kNm for G+Q-EY1 combination. When compared Tables 1 and 2, column 2 has more normal load and moment value than column 1 as seen from Tables 1 and 2. Maximum normal load (Nj) for j direction of column 2 is -12.16 kN. This load value is very close to column 1. Maximum shear load (Vj) is -3.31 kN and maximum moment load (Mj) is -3.40 kNm for G+Q+EY1 combination (Table 2).

Table 1. Numerical analysis results of Column 1 for Case 1.

Load	Ni	V2i	V3i	M2i	M3i	Nj	V2j	V3j	M2j	M3j
Unit		kN		kNm			kN		kNm	
G+Q+EX1	-11.25	4.74	1.12	2.79	2.77	4.71	1.12	1.03	1.17	**7.81**
G+Q+EX2	-10.60	**5.24**	1.47	3.61	3.14	5.49	2.58	-1.08	1.25	4.91
G+Q+EY1	-11.00	3.28	2.73	3.72	**5.71**	2.20	**4.69**	-3.59	2.39	2.99
G+Q+EY2	**-11.90**	1.13	2.83	1.99	-5.35	8.49	3.42	-1.25	2.21	1.52
G+Q-EX1	-11.25	-1.17	2.57	-1.29	-2.75	11.98	-2.61	2.47	2.36	-4.71
G+Q-EX2	-11.69	-1.67	2.12	-1.01	-2.71	12.39	-2.02	1.39	3.37	-4.79
G+Q-EY1	-5.60	0.29	-2.37	-2.43	-5.09	**12.42**	3.46	0.77	1. 44	-1.70
G+Q-EY2	-4.70	0.44	-2.57	-2.74	2.73	11.67	2.29	3.24	-2.88	2.97

Table 2. Numerical analysis results of Column 2 for Case 1.

Load	Ni	V2i	V3i	M2i	M3i	Nj	V2j	V3j	M2j	M3j
Unit		kN		kNm			kN		kNm	
G+Q+EX1	-12.46	-1.32	2.45	6.69	3.27	-5.97	-1.11	**-3.31**	-2.75	-0.82
G+Q+EX2	-11. 53	1.17	1.15	5.17	3.26	-6.54	-1.18	-1.11	-2.54	-0.23
G+Q+EY1	**-27.82**	**-4.21**	-1.68	3.87	-7.32	**-12.16**	-2.57	-1.29	**-3.40**	-0.64
G+Q+EY2	-21.61	-3.99	-2.51	-4.98	-6.76	-11.19	-2.97	-1.77	-3.09	-0.72
G+Q-EX1	-13.06	-2.71	-2.77	-4.36	-3.69	-4.97	-1.93	-1.63	-1.97	-0.06
G+Q-EX2	-10.84	-2.77	-2.47	-5.19	-4.82	-6.18	-1.44	-1.51	-1.06	-0.59
G+Q-EY1	-12.07	2.81	-1.14	-6.99	**13.72**	-7.83	-0.58	-1.19	-1.34	0.86
G+Q-EY2	-10.37	2.36	-1.67	4.57	4.26	-2.37	-1.96	-1.97	-1.37	-0.47

According to Table 3, numerical results for column 3 (Ni, V2i, V3i, M2i, M3i, Nj, V2j, V3j, M2j, M3j) are shown for Case 1. Maximum loads are marked in bold. In Table 3, maximum normal load (Ni) is -42.84 kN for G+Q+EY1 combination. More normal load value is acquired for column 3, when compared columns 1, 2. Moreover, maximum shear load (Vi) is 5.92 kN for G+Q+EY1 combination and maximum moment load (Mi) is 13.75 kNm for G+Q-EY1 combination. Maximum normal load (Nj) for j direction of column 3 is 1.93 kN. This load value is very less from columns 1 and 2. Maximum shear load (Vj) is -1.99 kN and maximum moment load (Mj) is 1.97 kNm (Table 3). When compared Tables 1, 2 and 3, less moment values are obtained for j direction of column 3.

Table 3. Numerical analysis results of Column 3 for Case 1.

Load	Ni	V2i	V3i	M2i	M3i	Nj	V2j	V3j	M2j	M3j
Unit		kN		kNm			kN		kNm	
G+Q+EX1	-34.01	1.01	1.87	5.97	-2.75	1.52	-1.75	1.45	-1.58	**1.97**
G+Q+EX2	-36.26	1.52	1.85	4.75	3.14	1.57	-1.65	1.53	-1.74	1.85
G+Q+EY1	**-42.84**	-3.55	1.21	1.57	-11.96	1.59	-1.87	-1.26	1.73	1.56
G+Q+EY2	-42.80	-2.74	1.47	1.41	-10.63	**1.93**	-1.21	-1.22	1.65	1.41
G+Q-EX1	-39.71	1.73	-1.57	-4.17	3.93	1.34	-1.19	-1.78	1.58	1.29
G+Q-EX2	-39.67	1.89	-1.96	-4.58	-3.29	1.08	-1.52	-1.89	1.82	1.87
G+Q-EY1	-35.97	**5.92**	-0.63	-3.99	**13.75**	1.82	-1.48	1.55	-1.27	1.89
G+Q-EY2	-35.88	4.28	0.39	-0.85	12.59	1.27	**-1.99**	1.23	-1.89	1.03

In Table 4, numerical results of column 4 (Ni, V2i, V3i, M2i, M3i, Nj, V2j, V3j, M2j, M3j) are shown for Case 1. Maximum loads are marked in bold and these loads are presented for 8 different combinations of 2019 Turkish Earthquake Code. According to Table 4, maximum normal load (Ni) is -38.39 kN for G+Q+EY1 combination. Less normal load value is acquired for column 4, when compared column 3. Moreover, maximum shear load (Vi) is 5.88 kN for G+Q+EY1 combination and maximum moment load (Mi) is 15.87 kNm for G+Q-EY1 combination. Maximum normal load (Nj) for j direction of column 4 is 3.99 kN. This load value is very less from columns 1 and 2. Maximum shear load (Vj) is -1.91 kN and maximum moment load (Mj) is 1.95 kNm (Table 4). When compared Tables 1, 2, 3 and 4, maximum moment value for j direction is obtained for column 4.

Table 4. Numerical analysis results of Column 4 for Case 1.

Load	Ni	V2i	V3i	M2i	M3i	Nj	V2j	V3j	M2j	M3j
Unit		kN		kNm			kN		kNm	
G+Q+EX1	-32.15	2.58	3.78	5.47	4.87	3.52	-1.75	1.52	-1.67	-0.87
G+Q+EX2	-33.58	2.41	2.94	4.95	5.24	3.08	-1.54	1.26	-1.89	-0.85
G+Q+EY1	**-38.39**	-3.39	1.71	2.28	-11.86	3.57	-1.58	1.45	0.57	-1.56
G+Q+EY2	-33.78	-3.85	-1.05	-3.87	-12.17	3.76	-1.79	-1.64	1.60	-1.33
G+Q-EX1	-32.68	1.52	-1.87	-5.08	-5.46	**3.99**	-1.25	-1.52	1.58	-1.58
G+Q-EX2	-33.54	1.22	-1.87	-5.87	-3.67	3.84	-1.05	-1.42	0.97	-1.38
G+Q-EY1	-34.29	**5.88**	-1.97	-1.57	**15.87**	3.75	**-1.91**	1.55	-1.87	**-1.95**
G+Q-EY2	-37.75	4.57	1.78	1.93	10.97	3.88	-1.72	1.26	-0.56	-1.56

According to Table 5, numerical results of column 5 (Ni, V2i, V3i, M2i, M3i, Nj, V2j, V3j, M2j, M3j) are shown for Case 2. In Table 5, maximum normal load (Ni) is -22.97 kN for G+Q+EY2 combination. Moreover, maximum shear load (Vi) is 9.54 kN for G+Q+EX1 combination and maximum moment load (Mi) is 27.69 kNm for G+Q+EX1 combination. Maximum normal load (Nj) for j direction of column 5 is 21.54 kN. Maximum shear load (Vj) is 12.28 kN and maximum moment load (Mj) is 11.59 kNm (Table 5).

In addition, numerical results of column 6 (Ni, V2i, V3i, M2i, M3i, Nj, V2j, V3j, M2j, M3j) are shown in Table 6. According to Table 6, maximum normal load (Ni) is -26.88 kN for G+Q+EY2 combination. Moreover, maximum shear load (Vi) is -8.92 kN for G+Q-EX1 combination and maximum moment load (Mi) is -35.33 kNm for G+Q-EX2 combination. Maximum normal load (Nj) for j direction of column 5 is -14.44 kN. Maximum shear load (Vj) is -4.67 kN and maximum moment load (Mj) is -6.97 kNm (Table 6).

Table 5. Numerical analysis results of Column 1 for Case 2.

Load	Ni	V2i	V3i	M2i	M3i	Nj	V2j	V3j	M2j	M3j
Unit		kN		kNm			kN		kNm	
G+Q+EX1	-13.58	**9.54**	1.63	8.78	**27.69**	10.64	**12.28**	-0.25	-1.58	**11.59**
G+Q+EX2	-13.92	6.87	2.33	9.89	24.54	12.57	5.59	-0.15	-1.97	6.97
G+Q+EY1	-21.05	1.99	5.24	12.62	-3.57	17.78	0.77	-1.68	-0.82	-3.98
G+Q+EY2	**-22.97**	-1.57	6.85	16.48	-5.73	18.85	1.98	-1.48	-2.05	-1.85
G+Q-EX1	-21.52	-5.26	-0.64	-9.04	-22.67	**21.54**	-4.56	-1.88	4.41	-5.57
G+Q-EX2	-21.04	-6.47	-0.67	-10.07	-21.82	20.78	-5.87	-1.70	5.23	-4.80
G+Q-EY1	-16.89	2.88	-4.62	-16.52	4.06	13.90	1.59	0. 06	4.52	3.05
G+Q-EY2	-15.75	1.16	-5.27	-20.24	10.79	12.06	1.03	0.68	4.22	4.87

Table 6. Numerical analysis results of Column 2 for Case 2.

Load	Ni	V2i	V3i	M2i	M3i	Nj	V2j	V3j	M2j	M3j
Unit		kN		kNm			kN		kNm	
G+Q+EX1	-14.25	4.52	5.55	19.52	13.05	-12.98	-3.00	-2.58	-5.87	-6.28
G+Q+EX2	-16.63	4.72	6.56	18.05	20.77	-11.74	-3.65	-4.26	-5.52	**-6.97**
G+Q+EY1	**-26.88**	-6.26	-2.78	-5.24	-33.52	**-14.44**	**-4.67**	-1.64	-1.67	-4.58
G+Q+EY2	-24.57	-4.37	-1.99	-6.54	-32.72	-12.65	2.99	-1.58	-1.60	-5.54
G+Q-EX1	-22.53	-5.16	**-8.92**	-24.65	-31.25	-12.25	-1.57	-1.57	-1.68	2.17
G+Q-EX2	-23.17	-6.88	-7.59	-20.54	**-35.33**	-11.59	-1.88	-1.58	0.15	1.19
G+Q-EY1	-11.19	6.80	-1.22	4.58	22.58	-12.88	1.82	-2.92	-4.65	-1.58
G+Q-EY2	-15.65	1.71	1.27	7.55	10.89	-11.62	0.28	-1.57	-2.74	1.86

According to Table 7, numerical results of column 7 (Ni, V2i, V3i, M2i, M3i, Nj, V2j, V3j, M2j, M3j) are shown for Case 2. In Table 7, maximum normal load (Ni) is -78.99 kN for G+Q+EY2 combination. Moreover, maximum shear load (Vi) is 19.98 kN for G+Q-EY2 combination and maximum moment load (Mi) is -54.88 kNm for G+Q+EY2 combination. Maximum normal load (Nj) for j direction of column 7 is 42.89 kN. Maximum shear load (Vj) is -6.91 kN and maximum moment load (Mj) is 7.58 kNm (Table 7).

In addition, numerical results of column 8 (Ni, V2i, V3i, M2i, M3i, Nj, V2j, V3j, M2j, M3j) are shown in Table 8. According to Table 8, maximum normal load (Ni) is -77.78 kN for G+Q+EY1 combination. Moreover, maximum shear load (Vi) is 12.88 kN for G+Q-EY1 combination and maximum moment load (Mi) is -52.91 kNm for G+Q+EY1 combination. Maximum normal load (Nj) for j direction of column 8 is 54.78 kN. Maximum shear load (Vj) is 6.92 kN and maximum moment load (Mj) is 5.92 kNm (Table 8).

Table 7. Numerical analysis results of Column 3 for Case 2.

Load	Ni	V2i	V3i	M2i	M3i	Nj	V2j	V3j	M2j	M3j
Unit		kN		kNm			kN		kNm	
G+Q+EX1	-70.28	-1.57	9.85	36.25	-24.54	41.54	-4.85	5.28	6.37	5.58
G+Q+EX2	-70.85	-2.58	9.74	36.64	-26.42	41.24	-4.80	5.52	**7.58**	6.45
G+Q+EY1	-73.84	-15.97	-4.25	7.58	-52.27	42.67	-3.56	3.19	6.57	6.68
G+Q+EY2	**-78.99**	-16.52	3.64	8.73	**-54.88**	**42.89**	-3.66	2.10	4.88	6.99
G+Q-EX1	-73.95	3.27	-4.55	-37.34	26.89	39.52	-3.85	**-6.91**	2.28	3.82
G+Q-EX2	-72.57	3.44	-9.41	-37.48	27.92	39.54	-4.57	-5.58	2.48	-2.58
G+Q-EY1	-66.08	14.66	-4.58	-6.59	48.11	38.59	-4.12	-3.77	4.08	1.71
G+Q-EY2	-62.57	**19.98**	-4.87	-8.85	50.57	38.97	-4.26	-2.52	4.14	-1.29

Table 8. Numerical analysis results of Column 4 for Case 2.

Load	Ni	V2i	V3i	M2i	M3i	Nj	V2j	V3j	M2j	M3j
Unit		kN		kNm			kN		kNm	
G+Q+EX1	-72.28	4.88	9.47	34.93	18.25	44.22	-1.67	**6.92**	5.38	2.52
G+Q+EX2	-72.68	5.54	9.85	34.26	24.78	44.07	-2.58	5.23	**5.92**	2.25
G+Q+EY1	**-77.78**	-9.46	-1.29	8.38	**-52.91**	**54.78**	2.77	2.67	4.47	2.29
G+Q+EY2	-76.62	-9.67	-1.97	-8.18	-46.28	44.89	1.20	2.56	5.42	2.71
G+Q-EX1	-73.05	-3.20	-9.97	-36.55	-36.44	43.55	-2.11	-4.29	2.50	5.85
G+Q-EX2	-74.64	-3.58	-9.48	-35.22	-33.56	43.52	-2.13	-4.71	1.77	5.29
G+Q-EY1	-69.17	**12.88**	-1.26	-8.20	45.69	41.17	-6.17	2.58	3.70	5.33
G+Q-EY2	-69.28	10.45	-1.58	8.84	40.33	41.69	-4.59	2.93	2.59	5.19

5. Conclusions

In this study, it is aimed to understand and show how important the non-structural elements are for the bearing capacities of the structures. For this purpose, in this study, Zonguldak Bulent Ecevit University laboratory building was selected for 3D modeling. After the building was modeled, machine load was given to the building and it was analyzed for two different situations (Cases 1and 2). Empty floor is named as Case 1 and floor with machine loads is named as Case 2 in this study. Considering the results of the analysis, it will be useful to consider the below suggestions:

- As seen these numerical results, nonstructural machines clearly affect the carrying loads (Ni, V2i, V3i, M2i, M3i, Nj, V2j, V3j, M2j, M3j) on carrying elements of the reinforced concrete buildings.
- When compared Cases 1 and 2, more normal loads are obtained for Case 2.
- Buildings with significant machine loads, such as laboratories, should be modelled taking into account these machine loads.
- It is obviously suggested that all machines on the damaged floor of the building must be removed. Because machine loads significantly increase the loads on all carrying elements.

References

Biswas RC, Iwanami M, Chijiwa N, Uno K (2020). Effect of non-uniform rebar corrosion on structural performance of RC structures: A numerical and experimental investigation. *Construction and Building Materials*, 230, 116908.

Chen L, Hu Y, Ren H, Xiang H, Zhai C, Fang Q (2019). Performances of the RC column under close-in explosion induced by the double-end-initiation explosive cylinder. *International Journal of Impact Engineering*, 132, 103326.

Chen X, Xinzheng L, Xuchuan L (2019). Damage assessment of shear wall components for RC frame–shear wall buildings using story curvature as engineering demand parameter. *Engineering Structures*, 189, 77-88.

Demartino C, Wu J, Xiao Y (2017). Experimental and numerical study on the behavior of circular RC columns under impact loading. *Procedia Engineering*, 199, 2457-2462.

Junsheng S, Zhongxian L, Junjie W, Rajesh PD (2020). Numerical simulation and damage analysis of RC bridge piers reinforced with varying yield strength steel reinforcement. *Soil Dynamics and Earthquake Engineering*, 130, 106007.

Kumar V, Kartik KV, Iqbal MA (2020). Experimental and numerical investigation of reinforced concrete slabs under blast loading. *Engineering Structures*, 206, 110125.

Li Y, Yin S-p, Chen W-j (2020). Seismic behavior of corrosion-damaged RC columns strengthened with TRC under a chloride environment. *Construction and Building Materials*, 201, 736-745.

Mohammed AA, Manalo AC, Maranan GB, Muttashar M, Zhuge Y, Vijay PV, Pettigrew J (2020). Effectiveness of a novel composite jacket in repairing damaged reinforced concrete structures subject to flexural loads. *Composite Structures*, 233, 111634.

Rajib KB, Mitsuyasu I, Nobuhiro C, Kunihiko U (2020). Effect of non-uniform rebar corrosion on structural performance of RC structures: A numerical and experimental investigation. *Construction and Building Materials*, 230, 116908.

Shuijing X, Longhe X, Zhongxian L (2019). Seismic performance and damage analysis of RC frame–core tube building with self-centering braces. *Soil Dynamics and Earthquake Engineering*, 120, 146-157.

Sulaem ML, Sudip T (2019). A study on the performance of damaged RC members repaired using ultra-fine slag based geopolymer mortar. *Construction and Building Materials*, 217, 216-225.

Tie-shuan Z, Ming-yang W, Cheng-yu Y, Tao Z, Chao G (2019). Experimental investigation on dynamic response and damage models of circular RC columns subjected to underwater explosions. *Defence Technology*, In Press.

Wei J, Li J, Wu C (2019). An experimental and numerical study of reinforced conventional concrete and ultra-high performance concrete columns under lateral impact loads. *Engineering Structures*, 201, 109822.

Xian-Liang R, Shan-Suo Z, Yi-Xin Z, Xiao-Yu Z, Li-Guo D (2019). Experimental study on the seismic behavior of RC shear walls after freeze-thaw damage. *Engineering Structures*, 206, 110101.

Xinchen Z, Bing L (2020). Damage characteristics and assessment of corroded RC beam-column joint under cyclic loading based on acoustic emission monitoring. *Engineering Structures*, 205, 110090.

Yang Z, Yanping Z, Marlyn Y, Dongliang M, Xudong S, Qi D, Genda C (2019). Flexural behaviors and capacity prediction on damaged reinforcement concrete (RC) bridge deck strengthened by ultra-high performance concrete (UHPC) layer. *Construction and Building Materials*, 215, 347-359.

Zhao C, Lu X, Wang Q, Gautam A, Wang J, Mo YL (2019). Experimental and numerical investigation of steel-concrete (SC) slabs under contact blast loading. *Engineering Structures*, 196, 109337.

Challenge Journal of Structural Mechanics

Research Article

L-shaped reinforced concrete retaining wall design: cost and sizing optimization

Aylin Ece Kayabekir [a], Zülal Akbay Arama [a], Gebrail Bekdaş [a,*], İlknur Dalyan [b]

[a] *Department of Civil Engineering, İstanbul University-Cerrahpaşa, 34320 İstanbul, Turkey*
[b] *Disaster and Emergency Management Presidency, 06800 Ankara, Turkey*

ABSTRACT

In the context of this study, the design of L-shaped reinforced concrete retaining walls have been scrutinized parametrically depending on the simultaneous analysis of cost and sizing with the use of a recent optimization algorithm. The differences and restrictions of L-shaped reinforced concrete retaining wall design than classical T-shaped walls have been also discussed. The foundation width and the thickness of the wall required for a safe design has been also investigated according to the change of excavation depth, the type of soil dominating field and the external loading conditions. The observed results from optimization analyses shows that the variation of the shear strength angle is the most significant soil geotechnical parameter for supplying an envisaged safe design against sliding, overturning and adequate bearing capacity. Concurrently, the excavation depth is the most important factor that is forming the necessity of the construction of the retaining structure and optimal dimension evaluation. It is also proved that the wall foundation width is the most effected dimension of the retaining structures by the change of design parameters and the cost difference is directly influenced by the change of sizing. A cost-effective wall design can be performed with the use of proposed optimization analysis is capable in a shorter time than the traditional methods. Eventually, it has shown that such optimization methods may be useful to find the optimal design requirements for geotechnical engineering structures.

ARTICLE INFO

Article history:
Received 6 March 2020
Revised 14 April 2020
Accepted 2 May 2020

Keywords:
Retaining wall
Soil properties
Optimization
Frictional soil
Jaya algorithm
Lateral soil pressure

1. Introduction

Retaining walls are basic type of civil engineering structures that are widely used to support excavation works or equipoise the lateral pressures when there is a difference in elevation. The main aim to construct a wall system is to resist lateral earth pressures with the self-weight of the whole system (Coulomb, 1776; Rankine, 1857; Boussinesq, 1882; Terzaghi, 1941). Depending on the project requirements, land ownership, environmental limitations and infrastructure locations it can be essential to build the sections of the wall with restrictions. L-shaped reinforced concrete retaining walls are the most common types of these restricted supporting systems. In such a case, the toe of the wall system is not constructed and the stability of the wall is controlled according to this limited section. The term "stability" means to ensure not also geotechnical but also structural design requirements simultaneously. Geotechnical stability conditions necessitates to supply sliding, overturning and total failure safety. In addition to this, the sections of the wall have to procure adequate shear and moment capacities and the steel reinforcement has to satisfy the relevant code requirements for reaching structural safety (Sasidhar et al., 2017). For a restricted type of retaining wall, it can be a significant problem to obtain stability conditions because the lack of one of the structural elements of the wall system causes to reduce resisting forces of the wall. This condition contributes to enlarge the foundation heel of the wall unpredictably.

* *Corresponding author*. Tel.: +90-212-4737070 ; Fax: +90-212-4737180 ; E-mail address: bekdas@istanbul.edu.tr (G. Bekdaş)
ISSN: 2149-8024 / DOI: https://doi.org/10.20528/cjsmec.2020.03.005

When this is the case, the construction works will not be economic. That's why, to acquire optimum cost of the wall connected to safe design have to be the most important factor for both engineers and employers. Several different methods are preferred to procure cost and sizing equilibrium depending on the advancements in computer technologies. Particle swarm optimization (Kennedy and Eberhart, 1995; Nedushan and Varaee, 2009), Genetic algorithm (Kalateh-Ahani and Sarani, 2019; Sasidhar et al., 2017; Holland, 1975; Kaveh et al., 2013), Big bang big crunch (Dorigo et al., 1996; Camp and Akin, 2012), Harmony search algorithm (Geem et al., 2001; Kaveh and Abadi, 2011; Uray et al., 2019), Bat algorithm (Yang, 2010), simulated annealing (Ceranic et al., 2001; Yepes et al., 2008; Pei and Xia, 2012), Grey wolf optimization (Bekdaş and Temur, 2018), teaching learning based optimization (Bekdaş and Niğdeli, 2016; Bekdaş and Temür, 2017) techniques can be given as examples of applied new methods to the optimization problem of retaining walls.

In the present study, L shaped retaining wall systems are parametrically designed taking into consideration the optimization of cost and sizing simultaneously. The focus point of the study is to obtain optimum design of restricted walls with the change of effective parameters on the envisaged design process. The effects of the change of soil properties, loading conditions and excavation depth is taken into consideration through the analyzed 105000 different cases that are performed with a recently proposed algorithm called Jaya. The results of the optimization analyses have been shown with two steps. The first step is based on the evaluation of the change of design parameters on the costs and the second step is the achievement of design due to the variation of envisaged parameters.

2. Methodology

In the Fig. 1, the cross section of a standard L-shaped retaining wall and the mobilized loads that are effecting on the wall system is illustrated. In Fig. 1, the height of the wall stem (H), the excavation depth (h), the embedment depth (d), the thickness of foundation base (x_5), the foundation heel width (x_1), the width of the stem at the base level (x_4) and the width of the stem at the ground level (x_3) is shown. Rankine Earth Pressure Theory is used to calculate active and passive earth pressure coefficients K_a ($\tan^2[45\text{-}\Phi/2]$) and K_p ($\tan^2[45+\Phi/2]$). W_{ws} and W_{wf} is the weight of the wall stem and the foundation base respectively. W_{sa} is the weight of the backfill soil retained on the foundation heel. $q_{\max}$ and $q_{\min}$ is the base pressures acting through the foundation. P_t is the average value of base pressures acting from the center of the gravity of foundation. P_{sa}, P_{sp} is the lateral soil forces for active and passive state and they can be calculated by the use of Eqs. (1) and (2) for pure frictional soils. It is a well-known issue that the passive lateral stresses are induced in relation to the embedment depth of the retaining structures. The activation of passive lateral earth forces causes to increase the resistance of the soil mass not to fail. But within the concern of this study, it is preferred not to use the passive earth pressures in stability analysis to stay on the safer side.

$$P_a = 0.5\gamma_s H^2 \tan^2([45 - \Phi/2]) \quad (1)$$

$$P_p = 0.5\gamma_s H^2 \tan^2([45 + \Phi/2]) \quad (2)$$

The term γ_s represents the unit weight of soil. An infinite distributed external load q_a is acted at the ground level and it is converted to horizontal load, Pq_a by the multiplication of active lateral earth coefficient of backfill material. The integrated components of the lateral disturbing forces can lead wall to slide through the base of the wall foundation. The wall system has to acquire enough security to carry this kind of unbalanced lateral loads. Dividing the sum of lateral resistant forces to the sliding forces gives the degree of sliding safety (SFs). The heaviness of the wall, the foundation soil base friction and the passive forces (it is not taken into consideration for current study) generates the resistant forces. Beside these states, the lateral component of the soil active forces and the surcharge loads induce unbalanced forces. The activation of lateral forces both active and passive leads the wall to overturn about its toe point (point A in Fig. 1). Dividing the sum of the moments generated by the resistant forces to the moments that is trying to slide the system, gives the safety degree for overturning behavior (SFo). In addition to these safety investigations, the bearing capacity failure has to be controlled by the division of ultimate bearing pressure to the maximum mobilized soil base pressure through the base of the wall. The upper and lower bounds of the soil base pressure values can be determined by the use of traditional bearing capacity equations proposed for shallow foundations (Dembicki and Chi, 1989; Powrie, 1996; Bowles, 1988; Yıldırım, 2002). In this study, the mentioned safety control of the wall section is tried to be controlled by the use of Jaya Algorithm that is proposed by Rao (2016) through the analysis conducted by Matlab Software. The logic of the Jaya Algorithm depends on the searching of the problem that has to be towards the best solution and has to stand aloof the worst solution which is used to choose the optimum sizing of the envisaged structure and to find minimum cost. The advantage of using Jaya Algorithm can be defined that it requires to identify the general control parameters as the number of generations and population size. Besides, no algorithm-specific parameters, that are special parameters to control for different algorithms. Hence, it is only required to elementally select the common control parameters in the Jaya algorithm without having to define more complex control parameters in applications. By the way Jaya Algorithm can be applied to several real-world optimization problems. That is the reason why to select the Jaya Algorithm to check the cost-effective design of L shaped reinforced concrete retaining walls in this paper. In the context of this study, in order to perform analysis with Jaya Algorithm for the evaluation of optimum sizing and cost relationship a certain flow has to be followed. Firstly the constant parameters of the retaining wall system, algorithm parameters, and the

ranges of the design parameters have to be defined and then the initial solutions are generated randomly. Until the attainment of stopping criteria, existing solutions are modified by the use of features of Jaya Algorithm. In consequence of the obtainment of the stopping criteria the analyses are stopped. Six different design variables (X_1, X_3, X_4, X_5, X_6, X_7) are considered in order to perform the optimization analysis of L-shaped reinforced concrete retaining walls that are given in Table 1. The variables are divided into two sections according to the related parameters with cross-section and reinforced concrete design. The first variable set includes the length of the heel and the thickness of the stem at the top, at the bottom and foundation base respectively. The second set includes the area of reinforcing bars of the stem and foundation heel. The design process begins with the scanning of safety values against the envisaged failure modes then if the satisfaction is gained it becomes necessary to define the implementation of the requirements of reinforced concrete. ACI 318-05 code is preferred to use because of its prevalent usage. This code proposes to define equivalent rectangular compressive stress distribution. As regards to the equivalent compressive stress distribution, the moment capacity of the wall system can be determined and only the critical sections of the stem and foundation is checked for the design of the reinforcement. The design constraints on strength and dimensions are shown in Table 2.

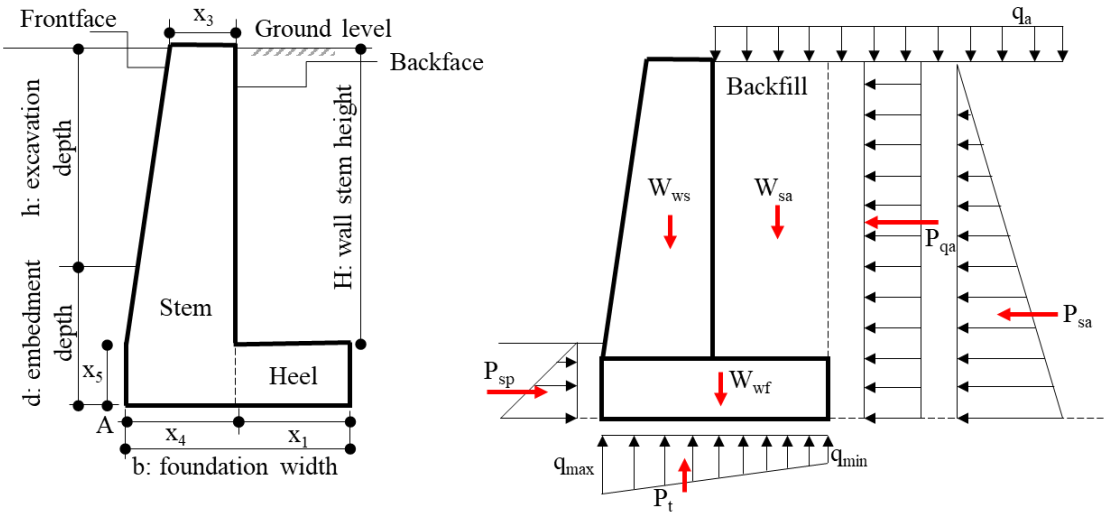

Fig. 1. L-shaped retaining wall cross section and the load distribution mode of administration.

Table 1. Definitions of L-shaped wall design variables.

	Symbol	Description of parameter
Variables in relation to cross-section dimension	X_1	Length of the heel (x_1)
	X_3	Thickness of wall stem at the top (x_3)
	X_4	Thickness of wall stem at the bottom (x_4)
	X_5	Thickness of wall foundation (x_5)
Variables in relation to reinforced concrete design	X_6	Area of reinforcing bars of the stem
	X_7	Area of reinforcing bars of foundation heel

Table 2. Design constraints on strength and dimensions.

Description	Constraints
Safety for overturning stability	$g_1(X)$: $F_oS_{ot,\text{design}} \geq F_oS_{ot}$
Safety for sliding	$g_2(X)$: $F_oS_{s,\text{design}} \geq F_oS_s$
Safety for bearing capacity	$g_3(X)$: $F_oS_{bc,\text{design}} \geq F_oS_{bc}$
Minimum bearing stress (q_{min})	$g_4(X)$: $q_{\min} \geq 0$
Flexural strength capacities of critical sections (M_d)	$g_{5\text{-}7}(X)$: $M_d \geq M_u$
Shear strength capacities of critical sections (V_d)	$g_{8\text{-}10}(X)$: $V_d \geq V_u$
Minimum reinforcement areas of critical sections (A_{smin})	$g_{11\text{-}13}(X)$: $A_s \geq A_{\text{smin}}$
Maximum reinforcement areas of critical sections (A_{smax})	$g_{14\text{-}16}(X)$: $A_s \leq A_{\text{smax}}$

The objective function of the performed analysis is preferred to include only the material costs to compare the effects of variants of the design process. Material costs that consist of the sum of concrete and reinforcing steel bars are defined by using the costs per unit volume/weight. The mathematical expression of the recommended objective function can be calculated by Eq. (3).

$$\min f_x = C_{concrete}.V_{concrete} + C_{steel}.W_{steel} \tag{3}$$

In this equation, C_{concrete} is the unit cost of concrete and C_{steel} is the unit cost of steel material, V_{concrete} is the volume of used concrete and W_{steel} is the weight of used steel per unit length.

3. Numerical Examples

The proposed methodology is applied to randomly select numerical examples that have been conducted in order to evaluate the effects of soil properties, surcharge loading conditions and excavation depth on the cost and sizing of L-shaped restricted retaining walls. The surrounding soil, backfill soil and foundation soil are assumed to be the same and they consist of pure frictional soils. The shear strength angle, unit weight of soil and ultimate soil pressure is taken into consideration as the variants of soil properties. The shear strength angle has been chosen from a range that is representing the strength characteristics of frictional soils loose to very dense in reference to Bowles (1988) (28° to 38°). The unit weight has been selected between 16 to 20 kN/m^3 to represent sandy soils and the ultimate soil pressure has been chosen 250, 300, 350, 400 kPa respectively for the analyzed cases. Excavation depth has been selected 4, 6, 8, 10, 12 meters and the surcharge load have been assumed to act from the ground surface locating at the backfill side. The excavation depths have been selected within the scope of the existing limits of the national and international related literature. The absence of the surcharge load and the effects of 5, 10, 15 and 20 kPa loading condition is investigated respectively. In the solution of the selected optimization cases, some constraints related to the dimensions of the wall system are applied. The lower and upper boundaries of top and bottom thickness of the wall stem is assumed to be between 0.2-3 meters and the thickness of the foundation is taken between 0.2-10 meters for all optimization analyses (Bowles, 1988). Other restrictions about the material properties, the safety degrees and the costs are listed in Table 3.

Table 1. The design constants and design variables of retaining walls.

Symbol	Definition	Value	Unit
μ	Concrete-soil friction	tan (2/3) ϕ	-
f_y	Yield strength of steel	420	MPa
f'_c	Compressive strength of concrete	25	MPa
c_c	Concrete cover	30	mm
E_{steel}	Elasticity modulus of steel	200	GPa
γ_{steel}	Unit weight of steel	7.85	t/m^3
γ_{concrete}	Unit weight of concrete	25	kN/m^3
C_c	Cost of concrete per m^3	75	$
C_s	Cost of steel per ton	700	$
SF_o	Factor of safety for overturning	1.5	-
SF_s	Factor of safety for sliding	1.5	-
SF_{bc}	Factor of safety for bearing capacity	3.0	-

4. Discussion and Results

It is a well-known issue that in the design process of a retaining wall system, the excavation depth, the geotechnical properties of soil and the loading conditions are crucial parameters that are affecting the design of retaining structures. In this respect, in this section it is aimed to control the effects of the mentioned parameters to the optimal cost effective design of L-shaped reinforced retaining walls. A great number of parametric analysis of envisaged different cases due to the changes in identifying parameters has been performed taking into consideration the constraints of the design. Totally 105000 optimization analysis is obtained and graphs are illustrated for selected special cases in order to describe the change of cost and sizing due to the related parameters. At the first step of the discussions, the change in total material cost is investigated and a number of specific reference cases are described to compare the influence rates of variants. At the second step, the change of wall sizing subjected to the variants is discussed with the calculation of foundation base thickness and total width.

Step 1: Total material cost change of construction:

In Fig. 2, the change in the total material cost of envisaged retaining wall design is taken into consideration against the increase of excavation depth with the change of the shear strength angle of the soil medium. The ultimate soil base pressure is assumed to be constant (q_s= 250 kPa) and the external load is not existing. The unit

weight of the soil has assumed to be the third variable for the analysis and Fig. 2 is drawn for both 16 and 19 kN/m^3 values of unit weight. The lateral axes is fixed to reach the same numeric value to ease the comparison. It is very explicit to say that the increase of the excavation depth rises the costs as the same manner for all the fictionalized cases. The change of soil unit weight hasn't got a significant effect for the discussions made with the evaluation of same excavation depth. In order to compare the influence rate of soil strength properties a reference constant excavation depth value can be selected and it can be seen that the strength of granular soil with the increase of shear strength angle leads costs to decrease. In conjunction with this, the influence ratio of shear strength angle increases with the increment of excavation depths. In all the cases except the case that the soil unit weight is 16 kN/m^3 and the shear strength angle is 38°, there cannot be able to obtain a proper design that is supporting 12 meters excavation depth due to the lack of technical adequateness (either geotechnical or static design safety requirements) within the limits of defined design variables. This situation can be categorized for procuring design restraints of L-shaped reinforced concrete retaining walls and maybe a limitation with a function of excavation depth can be asserted for defining the constructability of L-shaped walls. In Fig. 3, the change of total cost against the change of external loading conditions are given for two different excavation depth assumptions. The first case is defined for 4 meters and the second case is defined for 8 meters excavation depths. The ultimate base bearing capacity and the cost of concrete is assumed to be constant and selected to be 250 kPa and 75$ respectively.

On the other hand, the columns that are numbered beginning from 1 to 5 is representing the change of total costs against shear strength angles. It has to be noted that the numerical boundary values of the vertical axes of the graphs are different from each other. It is clear to say that the increase of external loading conditions leads to rise the total costs. But the incremental steps of total costs are dedicated to the change of soil strength. The increase of soil shear strength causes to decrease the relative cost change between the identified loading conditions. According to the analysis performed in the context of this paper, the maximum relative total cost change is occurring 49% rate and it comprised for the increasing excavation depths via the smallest shear strength angles (for example, the case of H=8 m and Φ=28°). In addition to this, the relative cost change for 4 meters is incontrovertibly important. The increase of soil shear strength from 28° to 38° leads relative cost change rates to decrease 37% to 25%. In such a case that evaluating the same external loading conditions for different shear strength values causes to change relative costs. The relative cost change is 34% for the case that the excavation depth is both 4 and 8 meters and the surcharge loading is constant 20 kPa. The absence of external loading causes to decrease the relative difference between the costs. In the case that the increase of friction 28° to 38° leads the relative difference change to become 27% for both excavation depths. Fig. 4 illustrates the total cost change against the unit weight of soil. Two different soil shear strength angles are selected to interpret the dual effects of soil characteristics. Soil unit weight is assumed to be 15, 16, 17, 18, 19, 20 kN/m^3 respectively. The results of the consideration of the increase of the soil unit weights individually and the comparability of them with the smallest value of the selected unit weights show a uniform increment of total costs with the increasing density. For the constant excavation depth H=4 m, the relative total cost change for Φ=30°, begins with 3% for γ=15 kN/m^3 and reaches 25% for γ=20 kN/m^3. The increase of excavation depth to 8 meters causes to rise relative cost change 5% to 29 for γ=15 kN/m^3 to 20 kN/m^3 respectively. Generally, it can be said that the increase of soil unit weight with the decrease of soil strength causes to raise the material costs. In Fig. 5 the change of total costs against the ultimate soil base pressure is shown due to the change of excavation depths. Excavation depths have been considered 4 meters and 8 meters respectively and other design variants are taken as constant values. The unit weight of soil is assumed to be 19 kN/m^3, the shear strength angle is 35° and no external load application is occurred. Ultimate base pressure is representing an upper boundary for foundation bearing pressure which is used to control bearing capacity failure of structures supported on or in soils. This failure control is conducted by the comparison of the calculated ultimate value of base pressure with the envisaged value of bearing capacity of soil. The calculated value of base pressure has to be smaller than the ultimate bearing pressure of soil.

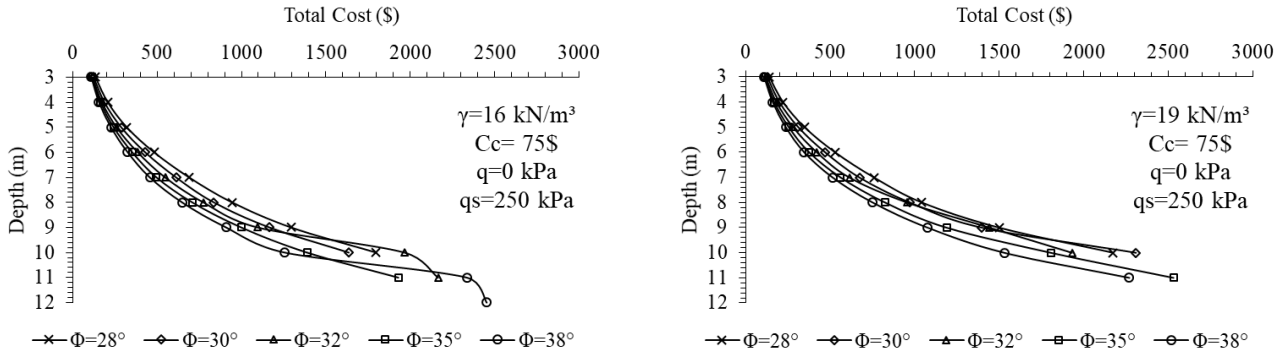

Fig. 2. Change of total cost against excavation depth and internal friction angle.

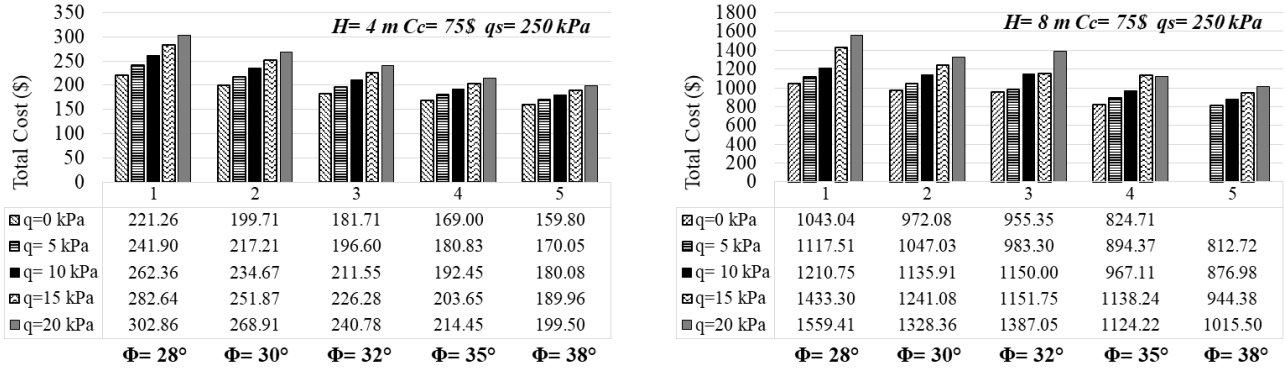

	Φ= 28°	Φ= 30°	Φ= 32°	Φ= 35°	Φ= 38°
q=0 kPa	221.26	199.71	181.71	169.00	159.80
q= 5 kPa	241.90	217.21	196.60	180.83	170.05
q= 10 kPa	262.36	234.67	211.55	192.45	180.08
q=15 kPa	282.64	251.87	226.28	203.65	189.96
q=20 kPa	302.86	268.91	240.78	214.45	199.50

	Φ= 28°	Φ= 30°	Φ= 32°	Φ= 35°	Φ= 38°
q=0 kPa	1043.04	972.08	955.35	824.71	
q= 5 kPa	1117.51	1047.03	983.30	894.37	812.72
q= 10 kPa	1210.75	1135.91	1150.00	967.11	876.98
q=15 kPa	1433.30	1241.08	1151.75	1138.24	944.38
q=20 kPa	1559.41	1328.36	1387.05	1124.22	1015.50

Fig. 3. Change of total cost against surcharge loading and internal friction angle.

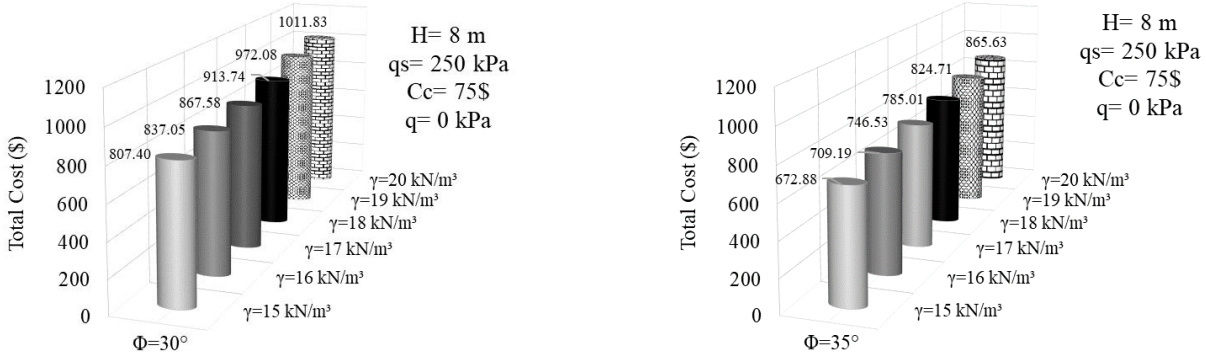

Fig. 4. Change of total cost against the unit weight and internal friction angle of soil.

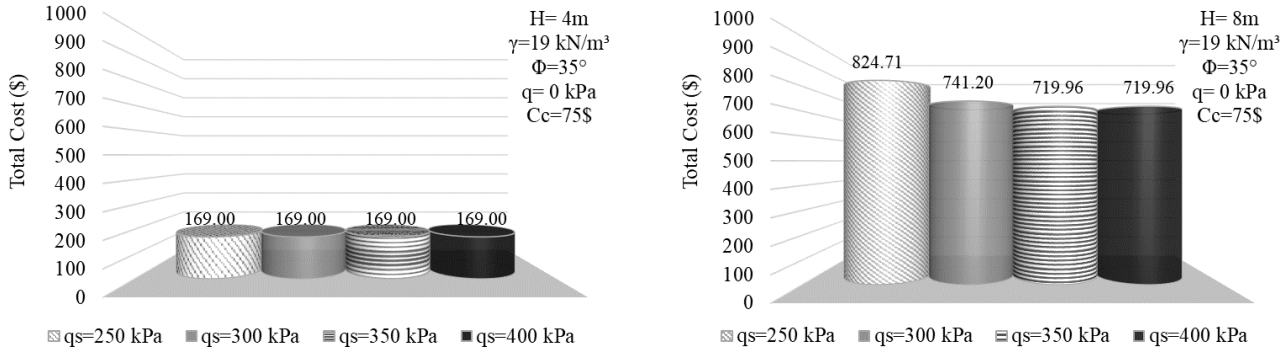

Fig. 5. Change of total cost against the ultimate soil base pressure and the excavation depth.

In case that the excavation depth is selected 4 meters, the change of ultimate bearing pressure hasn't got any effect on the cost of the system. This condition is happened due to the minority of the obtained design section weights with optimization technique. It can be said that the optimized structural design not causes to reach the ultimate base pressure of the soil medium for smaller excavation depths. But the increase of the excavation depth leads the behavior tendency to become dependent on the ultimate bearing pressure of the soil based on the increasing area of the structural design. The increase of the envisaged ultimate soil bearing pressure causes the design to become narrow and cost effective until reaching a boundary value. It can be said that after 350 kPa value of ultimate bearing pressure (from Fig. 5) the design of the system is not needed to be changed. After 350 kPa of ultimate bearing pressure the system is not needed to be changed and the cost is constant and equal to 720$. The increase of ultimate soil bearing pressure from 250 kPa to 350 kPa reduces the total costs of the structural design approximately 15%.

Step 2: The change of wall sizing:

The change of wall sizing based on optimal design of L-shaped walls have been evaluated by the use of the change of foundation dimensions. Foundation width and thickness is used as affected design parameters from variants of this paper. In Fig. 6 the change of wall base width against soil shear strength angle is illustrated with change of excavation depths. Two different excavation depths are assumed to be used to being a reference (*H*= 4 and 8 meters). The unit weight of the soil is assumed to

be 16 kN/m³ and the ultimate soil bearing pressure is selected 250 kPa as a constant. The absence of external surcharge loading is taken into consideration and evaluations are done according to the change of shear strength angle. In Fig. 6, it can be said that doubling the depth of excavation affected the base width at a similar rate. The change of internal friction angle for the cases that are in prospect hasn't got a significant effect as the change of excavation depth on the dimensions of foundation base. In such a case that is assumed to stay the same excavation depth, the influence of the change of the shear strength angle between the upper and lower limits is nearly calculated 33%. In addition to this, the change of the width of the foundation is nearly calculated 52% for the cases that the change of excavation depth is evaluated based on a constant value of the shear strength angle.

As a result, it can be seen from Fig. 6, the duplication of the excavation depth causes to twice the wall base width. In Fig. 7, the change of wall base thickness is illustrated against the change of shear strength angle and excavation depth. The values that are assumed to be constant for the previous case is taken at the same for Fig. 7. The change of internal friction angle for H=4 meter condition, hasn't got any effect on the design of the thickness of the foundation. But the deepening of the excavation depth causes to increase the thickness of the foundation base to ensure stability conditions because only the rise of the width of the foundation cannot supply the essential resistance that are required for the structural safe design. For the smallest internal friction angle (Φ=28°), the duplication of the excavation depth causes to increase the thickness of foundation twice and besides this the increase of shear strength angle to the envisaged highest value (Φ=38°) causes to increase the thickness 25%. In Fig. 8 and Fig. 9, the effect of the change of the soil unit weight on the dimensions of the wall is investigated for 4 and 8 meters excavation depths respectively. Shear strength angle (Φ=28°) and ultimate soil bearing capacity (q_s=250 kPa) is assumed to be constant and the absence of external load application is evaluated. In Figs. 8 and 9, it is clear to say that the change of foundation width is dominant than the changes in foundation thickness based on the difference of unit weight of soil. Fig. 8, shows that the increase of soil unit weight leads to the increase of foundation width 6% and the foundation thickness is not affected by the difference of soil unit weight. But in Fig. 9, it can be seen that the change of soil unit weight changes both the foundation thickness and the foundation width with 6% level. Figs. 10 and 11 represents the change of soil base ultimate bearing pressure to the wall dimensions for the conditions that the excavation depth is assumed to be 4 and 8 meters respectively. The ultimate bearing pressure values are variants of the cases and they have selected 250, 300, 350 and 400 kPa. The constant parameters of the case are selected the unit weight of soil (19 kN/m³), the shear strength of soil (Φ=35°) and the absence of external load application is taken into consideration. In Fig. 10, it will be proper to say the change of ultimate bearing pressure is an ineffective design parameter for relatively shallow excavation depths. But Fig. 11, represents a significant influence of ultimate bearing pressure on the design for relatively deep excavation depths for the selected cases. Due to Fig. 11, the required thickness and width of the wall base are decreased, by increasing the ultimate bearing pressure. Analysis that is conducted to obtain the change of external load magnitude on the design shows that the thickness of the foundation is not affected by loading magnitude. Therefore in Fig. 12, only the change of foundation width is shown for different external load applications. The change of foundation width is demonstrated with the dual evaluation of both shear strength angle and excavation depth. The excavation depth has been selected 4 and 8 meters like the before mentioned other cases. The ultimate soil bearing pressure is 250 kPa and the unit weight of the soil is selected 19 kN/m³. The absence of external loading and 5, 10, 15 and 20 kPa external loading conditions are treated respectively in the analysis. In Fig. 12, the vertical axes of the given graphs are different. In such a case that the excavation depth is 4 meters and the shear strength angle is 28°, the increase of external loads from 0 to 20 kPa causes to enlarge the foundation depth by 24%. If the shear strength angle increased to 38°, the increase of external loads from 0 to 20 kPa leads the foundation width to enlarge by 19%. The deepened the excavation depth results an important influence of external loads to the width of the foundation. In cases which the excavation depth is 8 meters and internal friction angle is selected 28°, the rise of external load from 0 to 20 kPa produces an increment on the foundation width by 47%. If the shear strength angle is assumed 38°, the rise of the external load causes to increase the dimension of foundation by 33%.

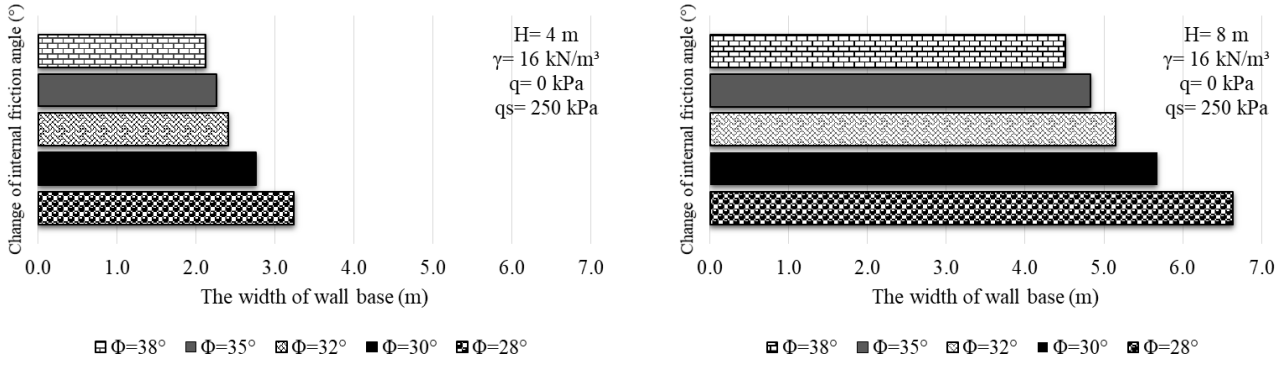

Fig. 6. Change of the wall base width against soil shear strength angle and the excavation depth.

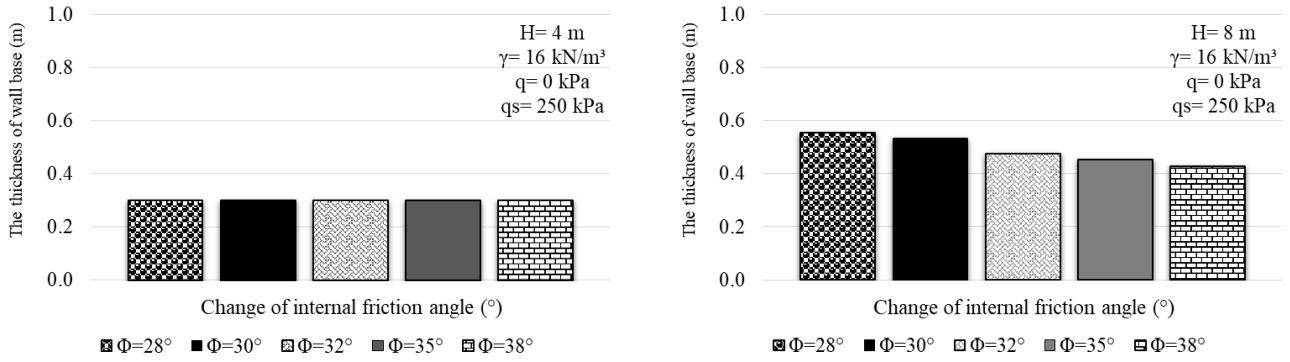

Fig. 7. Change of the wall base thickness against soil shear strength angle and the excavation depth.

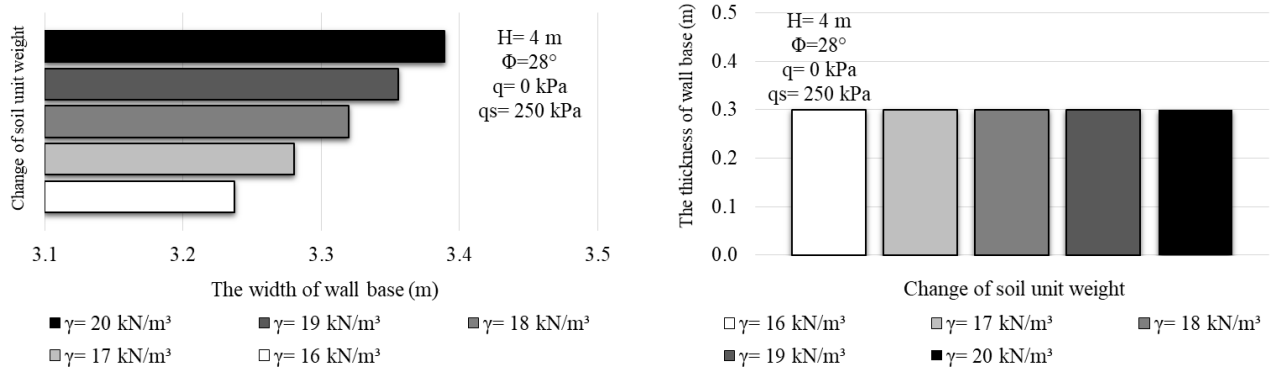

Fig. 8. Change of wall sizing against soil unit weight (*H*=4 m).

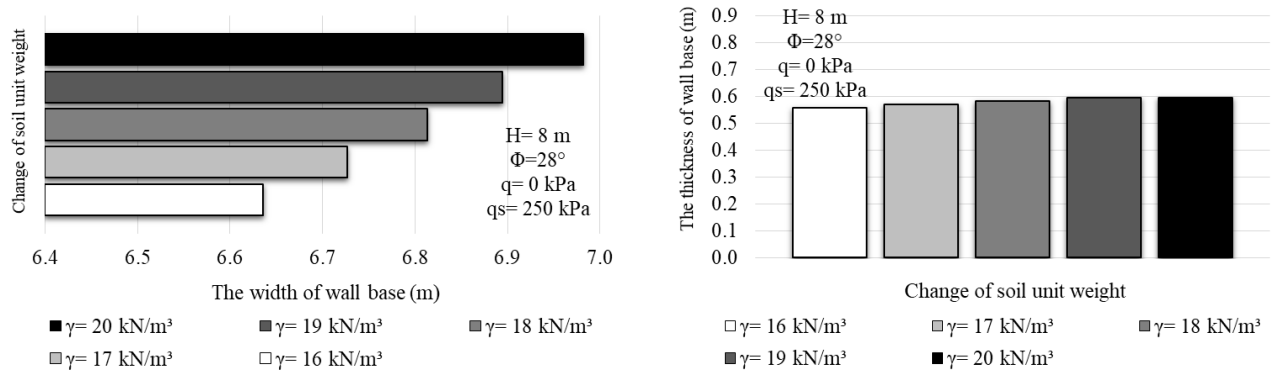

Fig. 9. Change of wall sizing against soil unit weight (*H*=8 m).

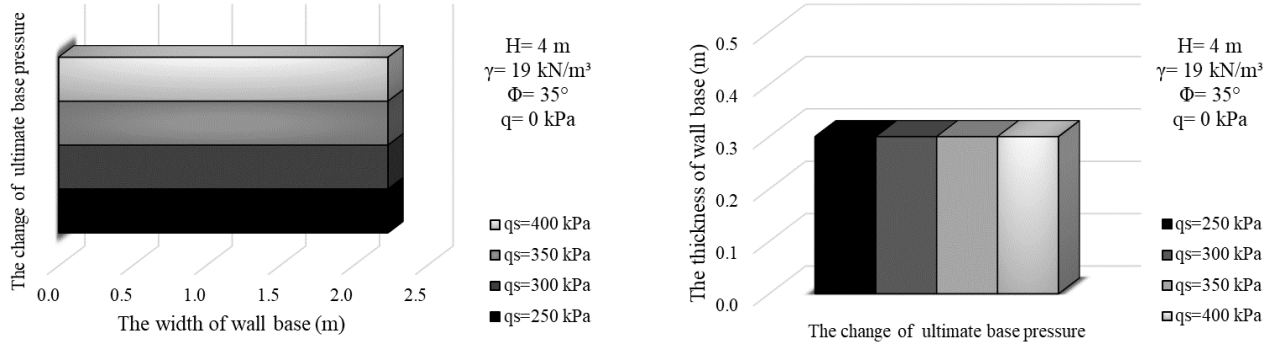

Fig. 10. Change of wall sizing against the ultimate base pressure (*H*=4 m).

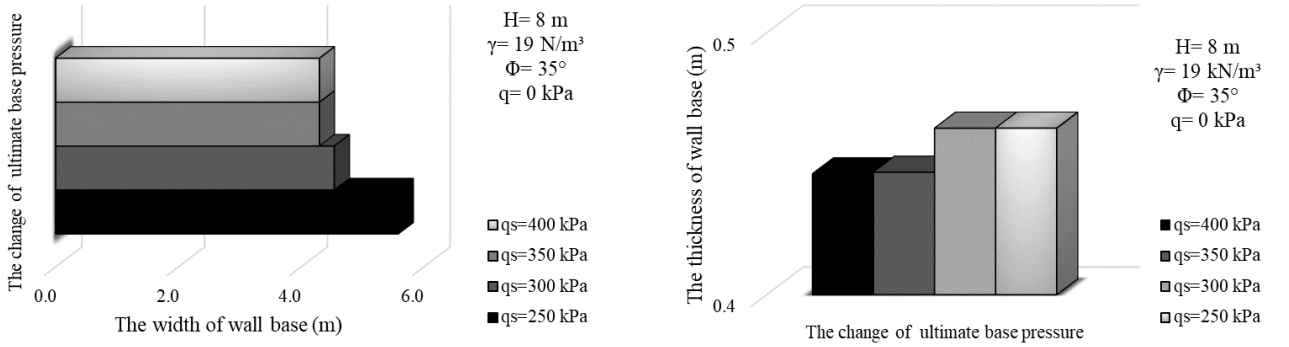

Fig. 11. Change of wall sizing against the ultimate base pressure (H=8 m).

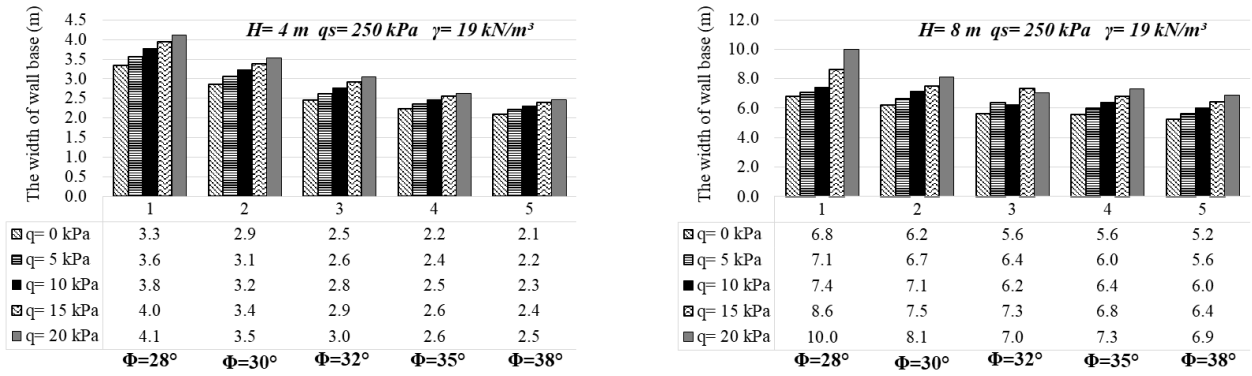

Fig. 12. Change of the width of the wall base against surcharge loading, internal friction angle and the excavation depth.

5. Conclusions

In the present study, innumerous optimization analysis is performed with Jaya Algorithm to find the cost effective sizing of L-shaped restricted reinforced concrete retaining walls. The vital point of the study is to investigate the influence rates of design parameters on the optimization process of the walls based on the applicable restrictions of L-shaped walls. Five different shear strength angles, four different ultimate base bearing pressures and five different soil unit weights have been used to derive various design cases to generate the embedding soil medium of retaining structures. Besides these, five different external surcharge loading condition is formed and five different excavation depths are compared with each other to control the parameter selection importance on design and cost balance. The analysis results have shown that the most influencer parameter on the design of L-shaped reinforced concrete retaining walls is the excavation depth. The deeper the excavation depth leads to widen the foundation width and causes the increase of costs in relation with the sizing. Besides this the shear strength angle has been found as the significant soil parameter which is changing the design entirely. The foundation width and the thickness of the foundation base is both affected by only the change of soil friction for the constructions done in granular soils. The unit weight change of the soil medium has only an effect on the width of the foundation. The increase of the soil unit weight causes to widen the foundation due to the increased lateral earth pressures. The effect of ultimate base bearing pressure can be the least effective soil parameter to obtain the optimal design. But the effect of the ultimate bearing pressure might have been relatively significant if the wall construction reached a limit height which can be changed according to the design requirements. The increase of the wall height has led the increase the vertical resisting forces with the increase of wall weight and this situation also has increased the lateral soil pressures. Besides this condition, the existence and increase of external surcharge loads cause to decrease the safety value against sliding, overturning and adequateness of ultimate soil base pressure. Because the increase of external loads at the backfill side of the wall system causes to increase the lateral forces and attain the structure unstable condition. Differently from this mentioned conclusion, it is obvious to say that the design of L-shaped walls are separated from T-shaped walls by the restriction of foundation base. Due to this restriction, it is hard to acquire essential structural strength and related geotechnical design to resist lateral earth with classical pre-design methods. So, this study represents the advantage of optimization techniques that are providing compatible and time-effective solutions for observing the limitations of design. In this study, the analysis is conducted for the excavation depths between 4-12 meters but it cannot be able to obtain an appropriate design that is supporting 9, 10 and 12 meters excavation depth due to the lack of technical adequateness (either geotechnical or static design safety requirements) within the limits of defined design variables. In addition to all these, the present study is original because of the usage of a

recently developed algorithm Jaya to a special type of a retaining wall. So it can be assumed that the present study is representative to show the applicability of this algorithm to special retaining wall designs. The advantage of optimization application according to the other limit state based retaining wall design software is to investigate the safe design requirements and to discuss the influencer parameters with time and cost effectiveness.

REFERENCES

ACI 318 (2014). Building Code Requirements for Structural Concrete and Commentary. ACI Committee.

Ahmadi-Nedushan B, Varaee H (2009). Optimal design of reinforced concrete retaining walls using a swarm intelligence technique. *The First International Conference on Soft Computing Technology in Civil, Structural and Environmental Engineering*, Stirlingshire, Scotland.

Bekdas G, Niğdeli SM (2016). Optimum design of reinforced concrete columns employing teaching-learning based optimization. *Challenge Journal of Structural Mechanics*, 2(4), 216-219.

Bekdas G, Temür R (2017). Metaheuristic approaches for optimum design of cantilever reinforced concrete retaining walls. *Challenge Journal of Structural Mechanics*, 3(1), 23-30.

Bekdas G, Temur R (2018). Grey wolf optimizer for optimum design of reinforced concrete cantilever retaining walls. *International Conference of Numerical Analysis and Applied Mathematics, AIP Conference Proceedings*, Amer Inst Physics, Melville.

Boussinesq J (1882). Sur la détermination de l'épaisseur minima que doit avoir un mur vertical d'une hauteur et d'une densité données, pour contenir un massif terreux sans cohésion, dont la surface supérieure est horizontale. *Ann. des Ponts et Chaussées*, t. III, 625.

Bowles JE (1988). Foundation Analysis and Design. McGraw-Hill, New York.

Camp CV, Akin A (2012). Design of retaining walls using big bang-big crunch optimization. *Journal of Structural Engineering, ASCE*, 138(3), 438-448.

Ceranic B, Fryer C, Baines RW (2001). An application of simulated annealing to the optimum design of reinforced concrete retaining structures. *Computers & Structures,* 79(17), 1569-1581.

Coulomb CA (1776). Essai sur une application des regles des maximis et minimis a quelques problemes de statique relatifs a l'artitecture. *Mem. Acad. Royal Pres. Div. Sav.*, Paris, 7.

Dembicki E, Chi T (1989). System analysis in calculation of cantilever retaining walls. *International Journal for Numerical and Analytical Methods in Geomechanics*, 13(6), 599-610.

Dorigo M, Maniezzo V, Colorni A (1996). The ant system: Optimization by a colony of cooperating agents. *IEEE Transactions on Systems, Man, and Cybernetics—Part B,* 26, 29-41.

Geem ZW, Kim JH, Loganathan GV (2001). A new heuristic optimization algorithm: harmony search. *Simulation*, 76, 60-68.

Holland JH (1975). Adaptation in Natural and Artificial Systems. University of Michigan Press, Ann Arbor MI.

Kalateh-Ahani M, Sarani A (2019). Performance-based optimal design of cantilever retaining walls. *Periodica Polytechnica Civil Engineering*, 63(2), 660-673.

Kaveh A, Abadi ASM (2011). Harmony search based algorithms for the optimum cost design of reinforced concrete cantilever retaining walls. I*nternational Journal of Civil Engineering,* 9(1), 1-8.

Kaveh A, Kalateh-Ahani M, Fahimi-Farzam M (2013). Constructability optimal design of reinforced concrete retaining walls using a multi-objective genetic algorithm. *Structural Engineering and Mechanics*, 47(2), 227-245.

Kennedy J and Eberhart RC (1995). Particle swarm optimization. In: *Proceedings of IEEE International Conference on Neural Networks No. IV*, Perth Australia; November 27 - December 1, 1942-1948.

Pei Y, Xia Y (2012). Design of cantilever retaining walls using heuristic optimization algorithms. *Procedia Earth and Planetary Science*, 5, 32-36.

Powrie W (1996). Limit equilibrium analysis of embedded retaining walls. *Geotechnique*. 46(4), 709-723.

Rankine WJM (1857). On the stability of loose earth. *Philosophical Transactions of the Royal Society of London*, 147, 9-27.

Rao R (2016). Jaya: A simple and new optimization algorithm for solving constrained and unconstrained optimization problems. *International Journal of Industrial Engineering Computations,* 7(1), 19-34.

Sasidhar T, Neeraja D, Samba Murthy Sudhindra V (2017). Application of genetic algoritm technique for optimizing design of reinforced concrete retaining wall. *International Journal of Civil Engineering and Technology*, 8(5), 999-1007.

Terzaghi K (1941). General wedge theory of earth pressure. *Transactions, ASCE*, 106, 68-97.

Uray E, Çarbaş S, Erkan İH, Tan Ö (2019). Parametric investigation for discrete optimum design of a cantilever retaining wall. *Challenge Journal of Structural Mechanics*, 5(3), 108-120.

Yang XS (2010). A New Metaheuristic Bat-Inspired Algorithm. In: *Nature Inspired Cooperative Strategies for Optimization (NISCO 2010), Studies in Computational Intelligence*, Springer Berlin, 65-74.

Yepes V, Alcala J, Perea C, Gonzalez-Vidosa F (2008). A parametric study of optimum earth-retaining walls by simulated annealing. *Engineering Structures*, 30(3), 821-830.

Yıldırım S (2002). Zemin Incelemesi ve Temel Tasarımı. Birsen Yayınevi, İstanbul. (in Turkish)

Challenge Journal of Structural Mechanics

Research Article

Stress and displacement analysis of perforated circular plates

Mustafa Halûk Saraçoğlu [a,*], Fethullah Uslu [a], Uğur Albayrak [b]

[a] *Department of Civil Engineering, Kütahya Dumlupınar University, 43100 Kütahya, Turkey*
[b] *Department of Civil Engineering, Eskişehir Osmangazi University, 26480 Eskişehir, Turkey*

ABSTRACT

Critical deflection and stress values of perforated circular plates under loads has an important role on the design criteria. For the perforated circular plates, the basic problem is determining how they have a perforation schema for the most suitable design. For this purpose, 10 different perforated circular plate models were presented and their static analysis was studied. All of the models have the same open area percentage but different number of holes. In this way, it was more convenient to compare the results. The circular plates were analyzed under their self-weight and uniformly distributed load with different nine thickness to diameter ratios obtained based on Classical Plate Theory. In addition, two set of analyses have been performed on the circular plates for fixed supported and simply supported boundary conditions. As an example, for the 6th model critical displacement and stress values under self-weight and under uniformly distributed load are investigated in detail. Designers of perforated circular plates can use the graphics presented in this study. The present study also purposes the shape optimization of thin circular perforated plates with round and staggered holes.

ARTICLE INFO

Article history:
Received 10 March 2020
Revised 16 May 2020
Accepted 3 June 2020

Keywords:
Displacement
Finite element method
Perforated circular plates
Static analysis
Stress

1. Introduction

Circular plates are common in many structures. They are used such as nozzle covers, end closures in pressure vessels, and bulkheads in submarines and airplanes, reactors, heat exchangers, and distillation towers (Jawad, 2010).

There are many practical applications of perforated plates because of their advantages. They let flow of light and air. They have a resistant to high/low temperature and corrosion. They have light weight and they have a low cost. Also, in the architectural applications - office buildings, hospitals, educational establishments, airports, stations etc. - perforated plates are can be used as a ceilings, floors, dividers, walls etc. Many equipment as speakers, furniture, dryers, light fixtures etc. are made of perforated plates. Also daily use areas are very wide including electrical components, agricultural equipment, mining, food processing equipment, vehicles as well as other machines.

Studies about perforated circular plates with a serial solutions are not found in abundance in literature.

Timoshenko and Woinowsky-Krieger (1959), wrote the basic reference for plates and shells. Many authors have interested in bending of perforated plates. Harrop and Abdul-Karim (1967), investigated the deflections and stresses for circular plates with square pitch perforations. The plates are subjected to uniform lateral pressure. They also compare the results with experimental results obtained by other investigators on three plate models. Murakami and Konishi (1982), studied about an elastic-plastic constitutive equation for transversely isotropic materials and as an application of the resulting constitutive equation, elastic-plastic bending of perforated circular plates is analyzed by modelling them by equivalent homogeneous transversely isotropic plates. Albayrak and Saraçoğlu (2011, 2018) and, Saraçoğlu and Albayrak (2016, 2017, 2018), were interested in plates with multiple holes and published some research articles about their subject. Wu et al. (2003), present a mathematical

* *Corresponding author*. Tel.: +90-274-443-4142 ; Fax: +90-274-265-2066 ; E-mail address: mhaluk.saracoglu@dpu.edu.tr (M. H. Saraçoğlu)
ISSN: 2149-8024 / DOI: https://doi.org/10.20528/cjsmec.2020.03.006

model of axisymmetric elastic/plastic perforated circular plate bending and stretching is developed which accounts for through thickness yielding, through thickness variations in perforation geometry, elastic outer edge restraint, and moderately large deflections. Atanasiu and Sorohan (2016), studied the displacements and stresses distribution in bending of perforated circular plate in their work using the finite element analysis (FEA) and experimentally by holographic interferometry. Azelmad et al. (2018), proposed a 2D typical model for the numerical simulation of the circular clamped perforated thin plates behavior in the elastic and elastoplastic domains. Their problem model is based on the real geometry of plates. The model takes into account different perforation distribution patterns and ligament factors. Also it is then validated by experiments. Konieczny et al. (2020), presented an analysis of an isotropic circular axisymmetric perforated plate loaded with concentrated force applied in the geometric center of the plate using finite element software ANSYS. The results of numerical calculations were compared and verified with experimental results.

In addition to theoretical studies, there are also studies that carry out experimental studies about this subject takes place in the literature. Osweiller (1989), presented some curves about the effective elastic constants based on consistent theoretical and experimental results in his study. These curves allow one to determine accurate and confident effective elastic constants and they were some help to engineers concerned with the design of multi-perforated plates. Solar and Hill (1976), analyzed the perforated plates for tubesheet design in their study. And also a simple analytical expression is proposed to determinate the effective bending stiffness of a perforated plate in the paper. Achtelik et al. (2008), presented a paper about elaborating the methodology of empirical studies in perforated plates centrally loaded by a concentrated force. They also presented experimental results to verify the mathematical model proposed in a companion paper.

There are a considerable number of studies that perform dynamic analysis as well as static analysis. Civalek and Çatal (2003), studied numerical solution to static and free vibration analysis of thin circular and annular plates having various supports and load conditions are obtained by the method of Harmonic Differential Quadrature (HDQ). Mishra and Das (1971), studied about free vibrations of isotropic nonhomogeneous circular plates and discussed the transverse vibration of nonhomogeneous free circular plate in their paper. Jhung et al. (2006), investigated free vibration analysis of perforated plate and in their study the equivalent material properties of perforated plates are suggested by performing several finite element analysis with respect to the ligament efficiencies. Jhung and Jo (2006), suggested the equivalent material properties of a perforated plate by performing several analyses with respect to ligament efficiencies. Jhung et al. (2009), studied about equivalent material properties of perforated structures. Lee and Chen (2011), in their paper theoretically derived the natural frequencies and natural modes of a circular plate with multiple circular holes and numerically determined. Dinkar (2015), study about vibration analysis of perforated plates in his doctoral thesis. Senjanovic et al. (2017), investigate the vibration analysis of thin circular plates with multiple openings. They use the assumed mode method and evaluate the results through their comparison with an analytical and finite element method solution. Jeong and Jhung (2017), have presented free vibration analysis of partially perforated circular plates with a triangular hole pattern and clamped boundary condition. They proposed a theoretical method and compare the results with finite element method solutions.

In this study, the effect of perforation pattern in perforated circular plates is investigated. For this purpose, ten perforated plate models were produced and statically analyzed under their self-weight. The finite element software ANSYS workbench was used to analyze the deflection behavior of thin circular plates with open holes in bending, and put forth a suitable perforation pattern for a perforated circular plate was proposed.

2. Material and Methods

Deformations and stresses in a plates are calculated by using a plate theory. Various plate theories have been developed since 19th century. In engineering two of them are widely used. One of them is named Kirchhoff–Love plate theory and also named as Classical Plate Theory (CPT). The other is named as Mindlin–Reissner plate theory and also named as First-order Shear Deformation Plate Theory (FSDPT). Every theory has different assumptions. In this study perforated circular plates are analyzed using CPT. In this theory the following kinematic assumptions are made:

- Straight lines normal to the mid-surface remain straight after deformation.
- Straight lines normal to the mid-surface remain normal to the mid-surface after deformation.
- The thickness of the plate does not change during a deformation.

In CPT, thickness to width ratio of a plate structure is have to be between 1/150 and 1/20.

The equations developed with reference to Cartesian coordinates are not convenient for the analysis of circular plates (Bhaskar et al., 2014). Therefore, the differential equations for the bending of a rectangular plate have to be transform to the polar coordinates for circular plates.

For the analysis of stress and displacement distribution of circular plates under loads, the derived differential equations of circular plates must have to be solved. These equilibrium equations of plates was made around 1900 by Love. These investigations were made for various boundary conditions and loadings.

When the load is symmetrically on the axis perpendicular to the circular plate through its center, the deflection surface is bent also symmetrically. So that, all points which have equal distance from the center of the plate the deflections will be the same as can be seen at Fig. 1.

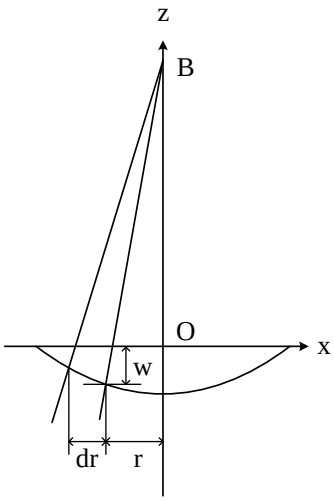

Fig. 1. Deflection of a circular plate.

The governing differential equation of a circular plate in cylindrical coordinates is given in Eq. (1):

$$\frac{1}{r}\frac{d}{dr}\left\{r\frac{d}{dr}\left[\frac{1}{r}\frac{d}{dr}\left(r\frac{dw}{dr}\right)\right]\right\} = \frac{q}{D} \tag{1}$$

In this equation w is the deflection of the plate, r is the radius coordinate of the circular plate, q is the intensity of loading and D is the flexural rigidity of the plate formulated at Eq. (2) dependent to E modulus of elasticity, υ Poisson's ratio and h plate thickness.

$$D = \frac{Eh^3}{12(1-\nu^2)} \tag{2}$$

Considered coordinates for circular plates with fixed supported and simply supported boundary conditions are shown in Fig. 2.

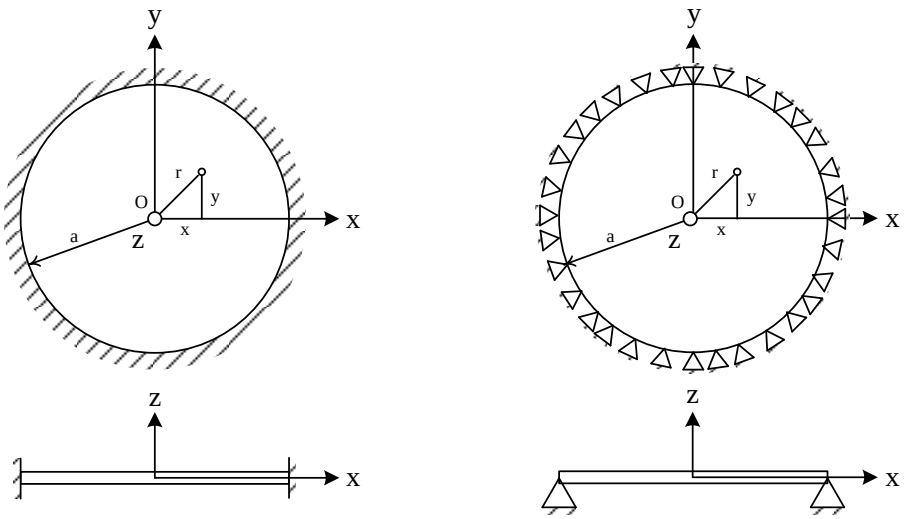

(a) Fixed supported (b) Simply supported

Fig. 2. Coordinates of a circular plate.

3. Numerical Applications

For demonstrating the differences between perforation patterns ten models were produced systematically as shown in Fig. 3. Firstly, a non-perforated circular plate with no holes is taken as a reference plate. These models were subjected to bending analysis under their self weights.

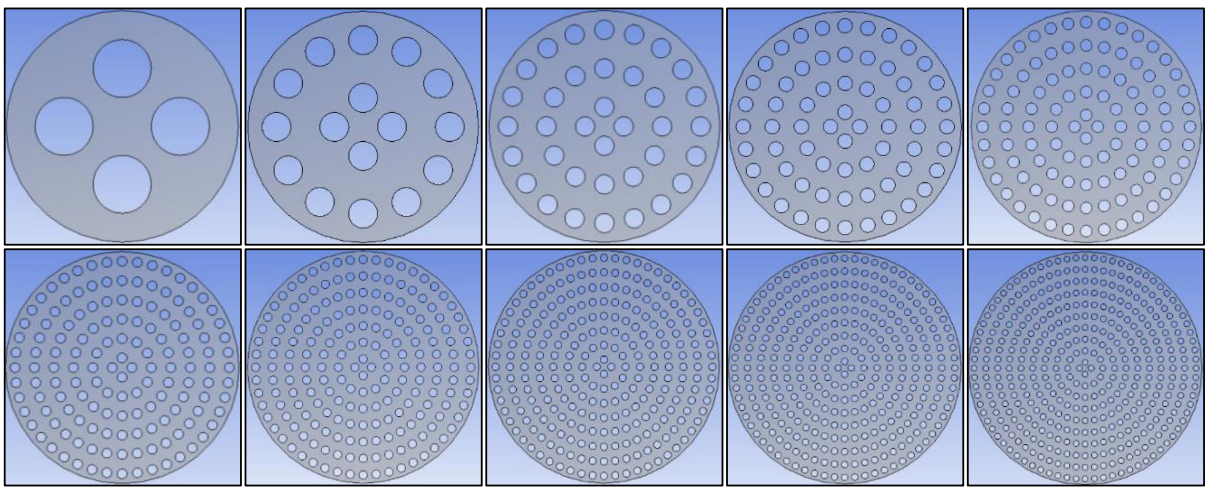

Fig. 3. Models of perforated circular plates.

Stress and displacement analysis of these models investigated and mid-point deflections and stresses are calculated. Circular plates are considered as they are thin plates. Nine different thickness to diameter ratio of these thin plate structures is taken into account as 2/300, 3/300, 4/300, 5/300, 6/300, 8/300, 10/300, 11/300 and 14/300 respectively. The solutions were developed for boundary conditions of simply supported and fixed supported.

The circular plate models are assumed to have the radius of 150 mm and made of steel material. The material parameters of the steel plates are assumed as shown in Table 1.

Table 1. Material properties of the perforated steel plate.

Property	Value
Young's modulus, E (GPa)	200
Poisson's ratio, υ	0.3
Mass density, ρ (kg/m^3)	7850

Shell181 has a capability for analyzing thin to moderately-thick shell structures. It is defined by four nodes. There are six degrees of freedom at each node as: rotations about the x, y and z axes, and translations in the x, y and z directions.

Triangular free mesh is used in free meshing operations. In the example models 1mm finite element mesh size is used.

After preprocessing the problem in the program, static analysis was performed and the results of deformations and stresses were obtained from the program.

Stress output for SHELL181 element is as follows:

σ_x is normal stress due to X axis (SX)

σ_y is normal stress due to Y axis (SY)

τ_{xy} is shear stress (SXY)

Number of holes, radius of the circular holes and total hole area is dependent to the model number n. In all of the perforated circular plate models % open area is the same as shown in Table 2.

Analyses of these models ANSYS software was used. This finite element software has various elements in the element library for static and dynamic analyses. For this study Shell181 is the most suitable element for the problem.

Table 2. Total hole areas for the models.

Model No	Number of holes	Radius	Total hole area
0	0	0.0000	$0*\pi*0^2$
1	4	37.5000	$4*\pi*37.5000^2$
2	16	18.7500	$16*\pi*18.7500^2$
3	36	12.5000	$36*\pi*12.5000^2$
4	64	9.3750	$64*\pi*9.3750^2$
5	100	7.5000	$100*\pi*7.5000^2$
6	144	6.2500	$144*\pi*6.2500^2$
7	196	5.3571	$196*\pi*5.3571^2$
8	256	4.6875	$256*\pi*4.6875^2$
9	324	4.1667	$324*\pi*4.1667^2$
10	400	3.7500	$400*\pi*3.7500^2$
.	.	.	.
.	.	.	.
.	.	.	.
n	$(2*n)^2$	$R/(4*n)$	$(\pi*R^2)/4$

4. Results and Discussion

Although the plate models in this study have the same arrangement they have different number of holes. The circular plates examined to different number of holes as 4, 16, 36, 64, 100, 144, 196, 256, 324, 400, respectively and radius and locations are also different. As seen from the Table 2, % open areas of the models are exactly same. Analyze results evaluate how the perforated circular would perform under self-weight. The results can be examined under two headings, namely displacements and stresses.

4.1. Displacements under self-weight

Fig. 4 shows comparison of mid-point deflections for fixed supported and simply supported non-perforated and perforated circular plates according to ten models with different nine thickness to diameter ratios obtained by ANSYS with solutions based on CPT.

It can be seen from the Fig. 4 that mid-point deflections of the circular plates have almost the same value for the models greater than 6th model.

Critical displacements for non-perforated and perforated (6th model) circular plates are given in Table 3.

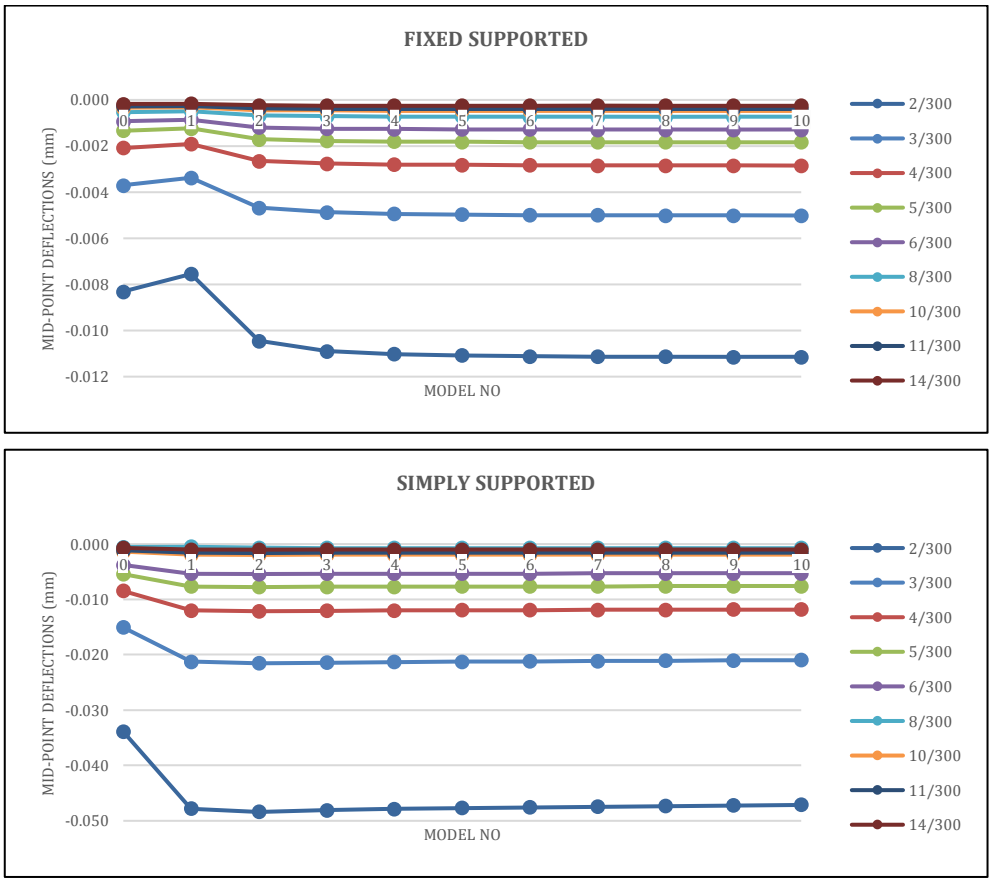

Fig. 4. Midpoint deflections of fixed supported and simply supported non-perforated and 10 perforated circular plate models according to thickness to diameter ratios.

Table 3. Critical displacements of the plates under self-weights (mm).

h/D	Fixed Supported		Simply Supported	
	non-perforated	perforated	non-perforated	perforated
2/300	-0.008318	-0.011111	-0.033893	-0.047570
3/300	-0.003701	-0.004989	-0.015067	-0.021177
4/300	-0.002085	-0.002833	-0.008478	-0.011930
5/300	-0.001337	-0.001828	-0.005429	-0.007647
6/300	-0.000930	-0.001280	-0.003772	-0.005318
8/300	-0.000526	-0.000730	-0.002125	-0.003000
10/300	-0.000339	-0.000473	-0.001362	-0.001925
11/300	-0.000282	-0.000393	-0.001127	-0.001593
14/300	-0.000176	-0.000247	-0.000698	-0.000988

Displacement values for all points of fixed and simply supported perforated (6th model) circular plate for D/h=150 under self-weights is shown in Fig. 5.

4.2. Displacements under uniformly distributed load

Displacements under uniformly distributed q=1kN/m^2 load has been performed on the two set of plates for fixed supported and simply supported non-perforated and 6th model perforated circular plates.

The critical displacements of the circular plates loaded with uniformly distributed load are shown in Table 4 with two support conditions. The maximum deflection is occurs at the midpoint of the circular plate and smaller than the thickness of the plate.

4.3. Stresses under self-weight

Stress distribution for the perforated circular holes under self-weights is more complex than the deflection distributions.

In Fig. 6, minimumSX and maximumSX stress values of non-perforated circular plate and ten models of fixed and simply supported perforated circular plates are shown.

MinimumSY and maximumSY stress values of non-perforated circular plate and ten models of perforated circular plates are shown in Fig. 7.

MinimumSXY and maximumSXY stress values of non-perforated circular plate and ten models of perforated circular plates are shown in Fig. 8.

As an example stress distribution of reference (non-perforated) and 6th model (perforated) plate for D/h=150 is shown in Fig. 9. In the example variation of stresses along line from point (0,0,0) to point (150,0,0) for perforated and non-perforated reference plates under their self-weights are given.

Similar to fixed supported plates, variation of stresses for simply supported circular plates are also given in Fig. 9.

From the graphs it can be inferred that there are large stress jumps on the perimeters of the holes.

The critical stresses of the circular plates under self-weights are shown in Table 5 with two support conditions. Circular plates are taken as non-perforated and as an example for 6th perforated model.

Stress values for all points of fixed and simply supported perforated (6th model) circular plate for D/h=150 under self-weights is shown in Fig. 10.

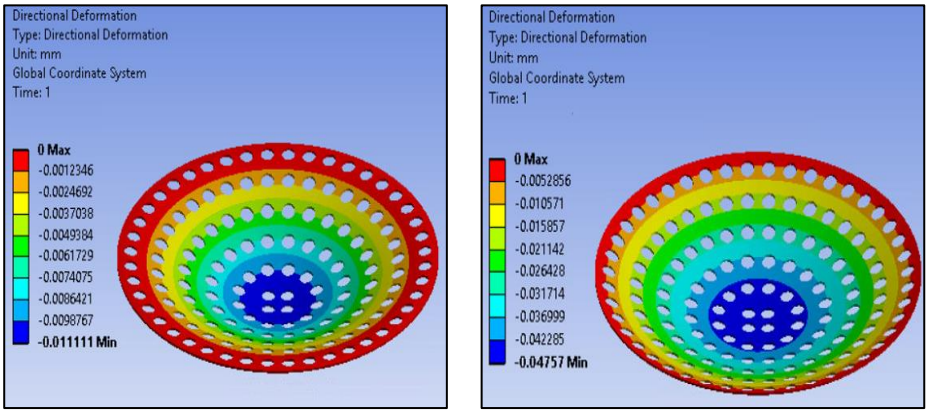

fixed supported simply supported

Fig. 5. Displacement values of fixed and simply supported perforated (6th model) circular plate for D/h=150 under self-weights.

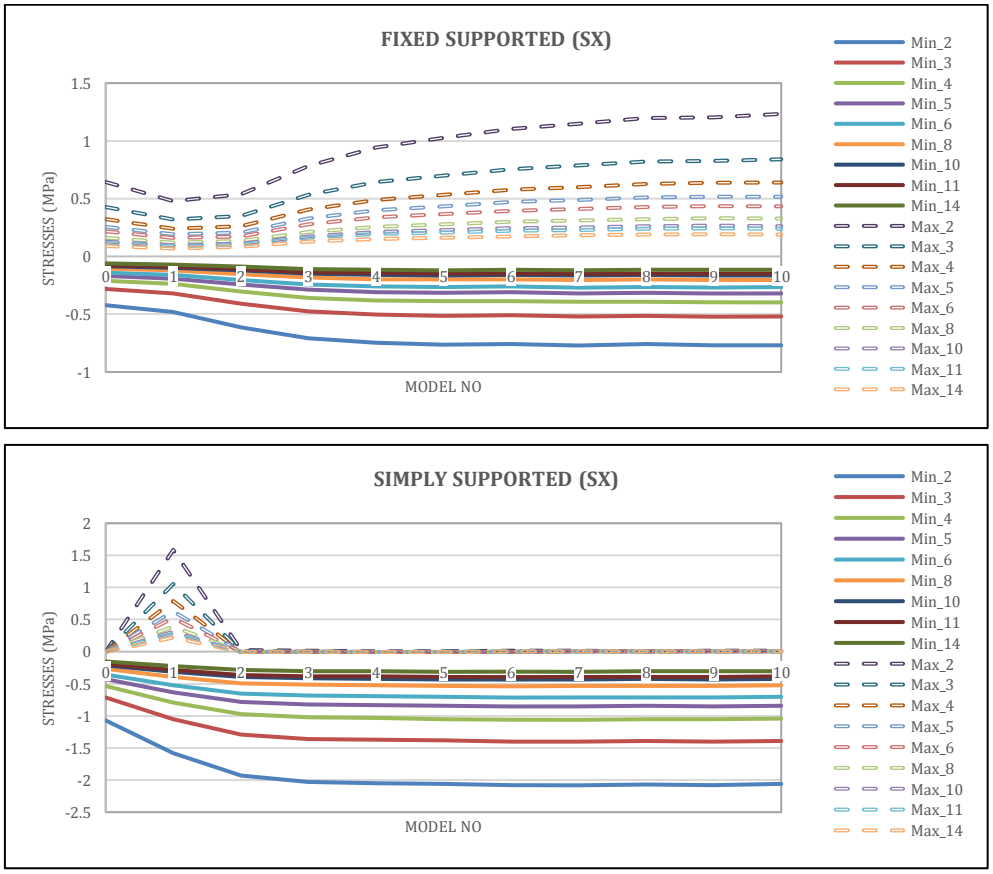

Fig. 6. MinimumSX and MaximumSX stress values of fixed supported and simply supported non-perforated and 10 perforated circular plate models.

Table 4. Critical displacements of the plates loaded with uniformly distributed load (mm).

h/D	Fixed Supported		Simply Supported	
	non-perforated	perforated	non-perforated	perforated
2/300	-0.054028	-0.072168	-0.220140	-0.308970
3/300	-0.016025	-0.021603	-0.065242	-0.091695
4/300	-0.006770	-0.009199	-0.027534	-0.038743
5/300	-0.003473	-0.004750	-0.014104	-0.019866
6/300	-0.002014	-0.002771	-0.008166	-0.011513
8/300	-0.000854	-0.001185	-0.003450	-0.004871
10/300	-0.000441	-0.000615	-0.001770	-0.002501
11/300	-0.000332	-0.000465	-0.001331	-0.001882
14/300	-0.000164	-0.000230	-0.000648	-0.000917

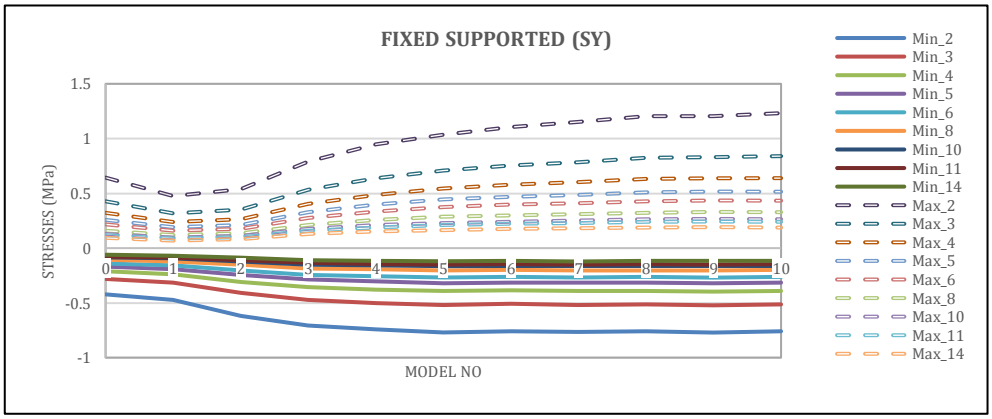

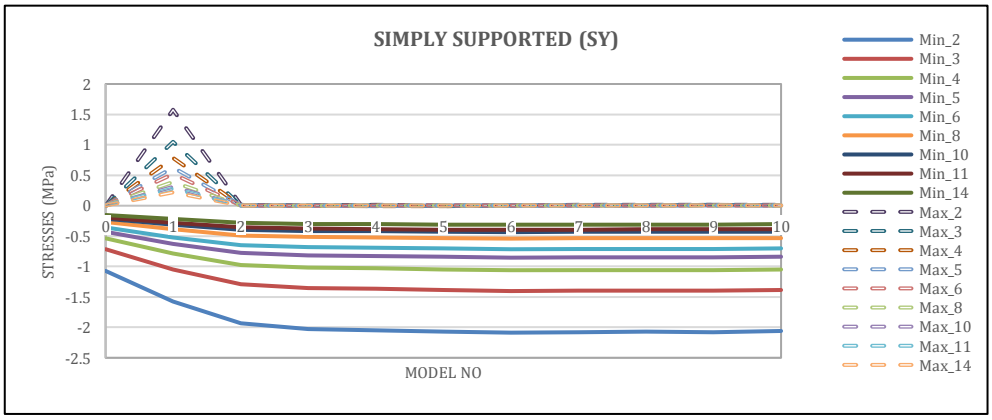

Fig. 7. MinimumSY and MaximumSY stress values of fixed supported and simply supported non-perforated and 10 perforated circular plate models.

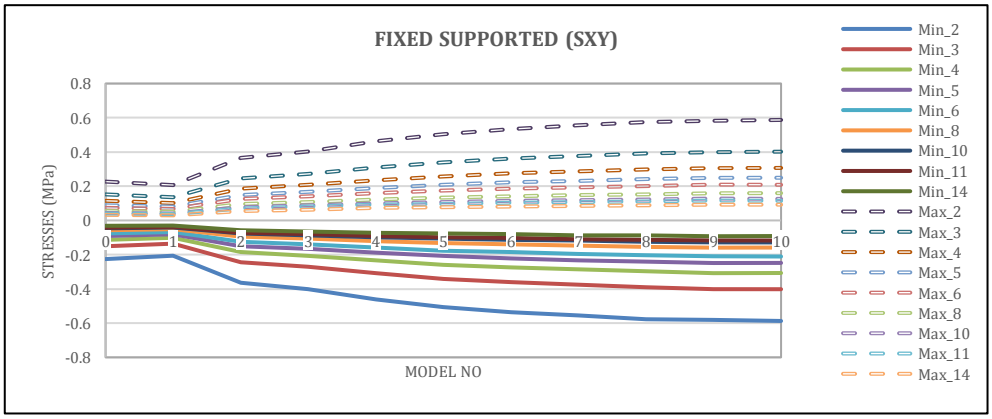

Fig. 8. (continued)

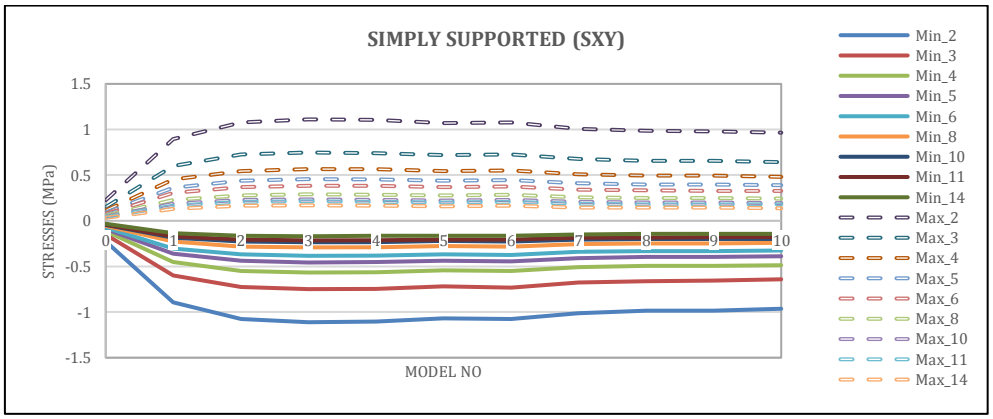

Fig. 8. MinimumSXY and MaximumSXY stress values of fixed supported and simply supported non-perforated and 10 perforated circular plate models.

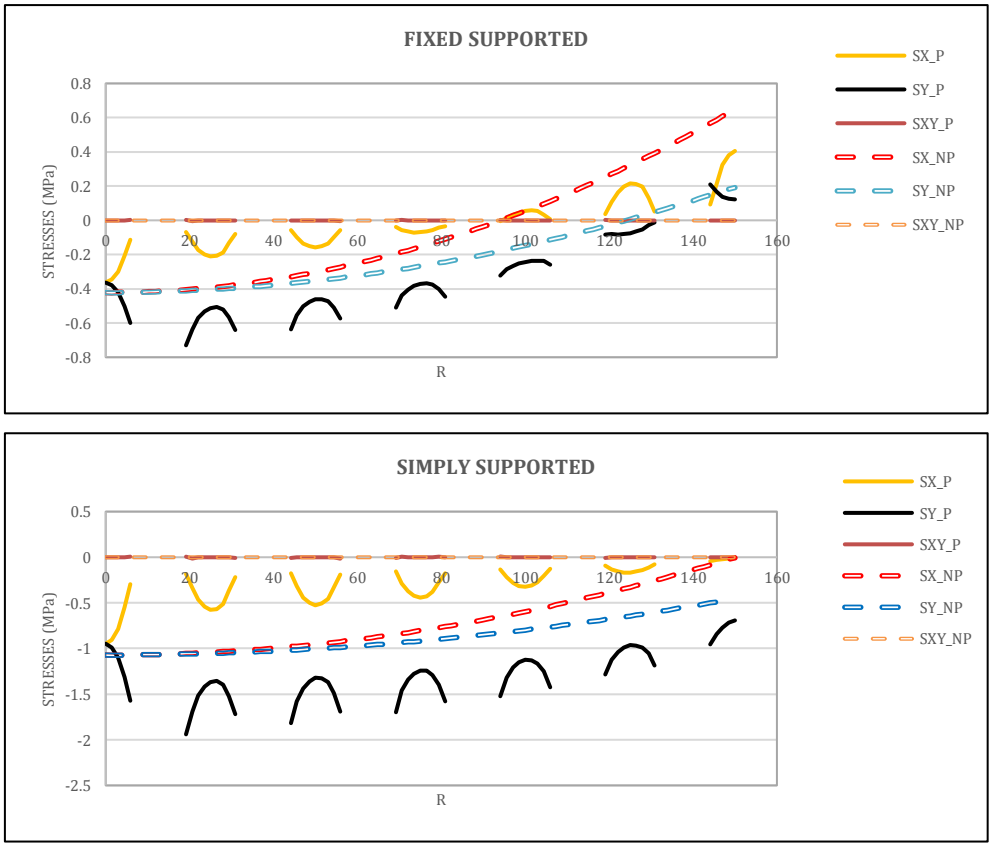

Fig. 9. Stress values of fixed supported and simply supported non-perforated and perforated (6th model) circular plate for D/h=150.

Table 5. Critical stresses of the plates under self-weights (MPa).

	Fixed Supported				Simply Supported			
	Minimum		Maximum		Minimum		Maximum	
	non-perforated	perforated	non-perforated	perforated	non-perforated	perforated	non-perforated	perforated
S_X	-0.422180	-0.756420	0.644680	1.104500	-0.004581	0.012353	-1.071700	-2.080700
S_Y	-0.422170	-0.757280	0.644880	1.106200	-0.004164	0.008235	-1.071700	-2.086300
S_{XY}	-0.226080	-0.535380	0.226080	0.535380	0.226120	1.077800	-0.226120	-1.077800

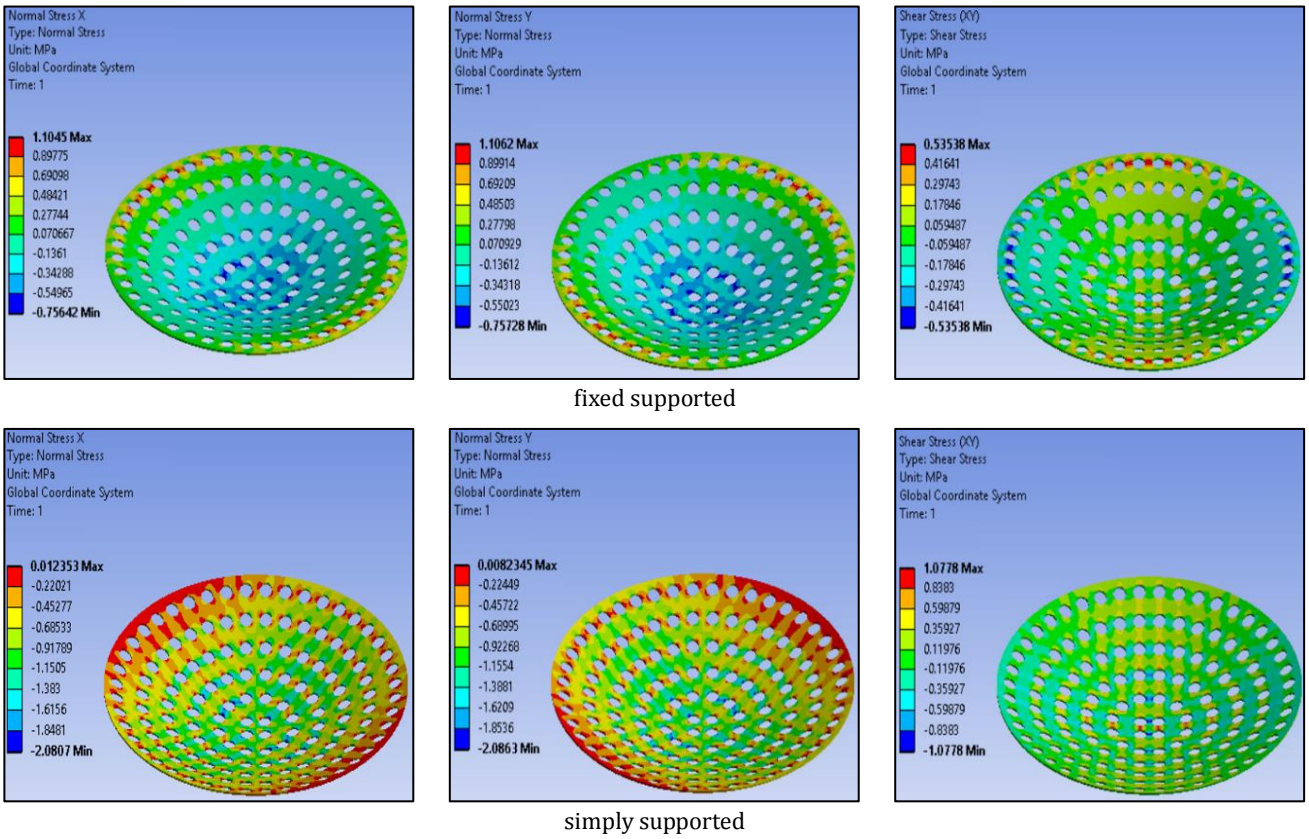

Fig. 10. Stress values of fixed and simply supported perforated (6th model) circular plate for D/h=150 under self-weights.

4.4. Stresses under uniformly distributed load

Stresses under uniformly distributed q=1kN/m² load has been performed on the two set of plates for fixed supported and simply supported non-perforated and 6th model perforated circular plates.

The critical stresses of the plates loaded with uniformly distributed load can be seen in Table 6.

Table 6. Critical stresses of the plates loaded with uniformly distributed load (MPa).

	Fixed Supported				Simply Supported			
	Minimum		Maximum		Minimum		Maximum	
	non-perforated	perforated	non-perforated	perforated	non-perforated	perforated	non-perforated	perforated
S_X	-2.742	-4.9129	4.1872	7.1739	-0.029753	0.080234	-6.9607	-13.514
S_Y	-2.742	-4.9186	4.1885	7.1847	-0.027043	0.053483	-6.9607	-13.551
S_{XY}	-1.4684	-3.4773	1.4684	3.4773	1.4686	7.0004	-1.4686	-7.0004

5. Conclusions

In this paper, the mid-point deflection and stress values of the perforated circular plate under self-weights and under uniformly distributed load with the influence of holes was calculated and analyzed. Series of models have been produced for investigating the stresses and displacements of perforated circular plates.

The results obtained can be listed as follows:

- In all of the perforated circular plate models % open area is the same as shown in Table 2.
- Problems were analyzed by using finite element analysis software ANSYS Workbench.
- Displacement and stress distribution of perforated circular plate under self-weights and under distributed q=1kN/m² load was separately analyzed and results are presented as tables and graphics.
- Critical deflection and stress values has an important role on the design of perforated circular plates.
- The deflections for the simply supported perforated circular plates is approximately 4.3 times higher than those fixed supported perforated circular plates.

- The results obtained for nine different diameter/thickness values within the limits of thin plate acceptance showed approximately the same behavior.
- The variation of the deflection and stress values are getting asymptotic after the 6th model.
- Critical displacement values of perforated circular plate under self-weights for fixed supported is 0.011111 mm and for simply supported is 0.047570 mm.
- Critical SX values of perforated circular plate under self-weights for fixed supported is 1.104500 MPa and for simply supported is 2.080700 MPa.
- Critical SY values of perforated circular plate under self-weights for fixed supported is 1.106200MPa and for simply supported is 2.086300 MPa.
- Critical SXY values of perforated circular plate under self-weights for fixed supported is 0.535380 MPa and for simply supported is 1.077800 MPa.
- Critical displacement values of perforated circular plate under distributed load for fixed supported is 0.072168 mm and for simply supported is 0.308970 mm.
- Critical SX values of perforated circular plate under distributed load for fixed supported is 7.173900 MPa and for simply supported is 13.514000 MPa.
- Critical SY values of perforated circular plate under distributed load for fixed supported is 7.184700 MPa and for simply supported is 13.551000 MPa.
- Critical SXY values of perforated circular plate under distributed load for fixed supported is 3.477300 MPa and for simply supported is 7.000400 MPa.
- When the number of holes increases, deflection and stress values are getting asymptotic.
- Designers of perforated circular plates can take into account these midpoint deflections by using these graphics.

As a result, the present study purposes the shape optimization of thin circular perforated plates with round and staggered holes. And perforation schemas can also be developed by different optimization techniques.

References

Achtelic H, Gasiak G, Grzelak J (2008). Strength tests of axially symmetric perforated plates for chemical reactors: Part 2-Experiments. *International Journal of Pressure Vessels and Piping*, 85, 257–264.

Albayrak U, Saraçoğlu MH (2011). Analyzing of thin square plates with multiple circular holes. *International Symposium on Advances in Applied Mechanics and Modern Information Technology 2011 (ISAAM&MIT'11)*, Baku, Azerbaijan, 79–83.

Albayrak U, Saraçoğlu MH (2018). Analysis of regular perforated metal ceiling tiles. *International Journal of Engineering and Technology,* 10(6), 440–46.

Atanasiu C, Sorohan S (2016). Displacements and stresses in bending of circular perforated plate. *IOP Conference Series: Materials Science and Engineering,* 147(1).

Azelmad E, Salmi A, El Kennassi E, Bousshine L (2018). Elastoplastic behavior analysis of clamped circular perforated thin plates. *IOSR Journal of Mechanical and Civil Engineering*, 15(2), 23–37.

Bhaskar K, Varadan R (2014). Plates: Theories and Applications. Wiley Online Library, ISBN:9781118893876.

Civalek Ö, Çatal H (2003). Linear static and vibration analysis of circular and annular plates by the harmonic differential quadrature (HDQ) method. *Journal of Engineering and Architecture Faculty of Eskişehir Osmangazi University,* XVII(1), 43–71.

Dinkar MK (2015). Vibration Analysis of Perforated Plates. *Ph.D thesis*, Birla Institute of Technology and Science, Pilani.

Harrop J, Abdul-Karim RM (1967). Stresses and deflections in circular plates with square pitch perforations. *Nuclear Engineering and Design,* 6(5), 431–39.

Jawad MH (2010). Design of Plate and Shell Structures: Bending of Circular Plates. ASME Press, ISBN: 0791801993.

Konieczny MM, Achtelik H, Gasiak G (2020). Finite element analysis (FEA) and experimental stress analysis in circular perforated plates loaded with concentrated force. *Frattura ed Integrita Strutturale,* 14(51), 164–173.

Kyeong-Hoon J, Myung-Jo J (2017). Free vibration analysis of partially perforated circular plates. *Procedia Engineering,* 199, 182–87.

Lee WM, Chen JT (2011). Free vibration analysis of a circular plate with multiple circular holes by using indirect BIEM and addition theorem. *Journal of Applied Mechanics, Transactions ASME,* 78(1), 0110151–510.

Mishra DM, Das AK (1971). Free vibrations of an isotropic nonhomogeneous circular plate. *AIAA Journal*, 9(5), 963–64.

Murakami S, Konishi K (1982). An elastic-plastic constitutive equation for transversely isotropic materials and its application to the bending of perforated circular plates. *International Journal of Mechanical Sciences,* 24(12), 763–75.

Myung J, Hwan Y, Ho Y (2009). Equivalent material properties of perforated structure for free vibration analysis. *Modal Analysis,* (SMiRT 20), 1–8.

Myung Jo J, Jong Chull J (2006) Equivalent material properties of perforated plate with triangular or square penetration pattern for dynamic analysis. *Nuclear Engineering and Technology,* 38(7), 689–96.

Myung-Jo J, Jong Chull J, Kyeong Hoon J (2006). Free vibration analysis of perforated plate submerged in fluid. *Journal of Mechanical Science and Technology,* 20(9), 1323–38.

Osweiller F (1989). Evolution and synthesis of the effective elastic constants concept for the design of tubesheets. *Journal of Pressure Vessel Technology, Transactions of the ASME,* 111(3), 209–17.

Saraçoğlu MH, Albayrak U (2016). Linear static analysis of perforated plates with round and staggered holes under their self-weights. *Research on Engineering Structures & Materials,* 2(1), 39–47.

Saraçoğlu MH, Albayrak U (2017). Computational analysis of perforated rectangular thin plates. *2nd International Conference on Civil and Environmental Engineering*, Nevşehir, Turkey, 1864.

Saraçoğlu MH, Albayrak U (2018). Analysis of regular perforated rectangular plates. *5th International Conference on Civil and Urban Engineering (ICCUE 2018)*, Barcelona, Spain, 47.

Senjanović I, Hadžić N, Vladimir N (2017). Vibration analysis of thin circular plates with multiple openings by the assumed mode method. *Proceedings of the Institution of Mechanical Engineers Part M: Journal of Engineering for the Maritime Environment,* 231(1), 70–85.

Solar AI, Hill WS (1976). Effective bending properties for stress analysis of rectangular tubesheets. *American Society of Mechanical Engineers (Paper)* (76-WA/Pwr-1), 365–70.

Timoshenko S, Woinowsky-Krieger S (1959). Theory of Plates and Shells. McGraw-Hill Inc.

Wu DJ, Peddieson GR, Rochelle SG (2003). Large axisymmetric deformations of elastic/plastic perforated circular plates. *Journal of Pressure Vessel Technology, Transactions of the ASME,* 125(4), 357–64.